Cavity Optical Spring Sensing for Single Molecules

by

Wenyan Yu
B.Sc., Zhejiang University, China, 2006
M.A.Sc., University of Victoria, 2012

A Dissertation Submitted in Partial Fulfillment of the
Requirements for the Degree of

DOCTOR OF PHILOSOPHY

in the Department of Electrical and Computer Engineering

Cavity Optical Spring Sensing for Single Molecules

by

Wenyan Yu
B.Sc., Zhejiang University, China, 2006
M.A.Sc., University of Victoria, 2012

Supervisory Committee

Dr. Tao Lu, Supervisor
(Department of Electrical and Computer Engineering)

Dr. Chris Papadopoulos, Departmental Member
(Department of Electrical and Computer Engineering)

Dr. Peter Wild, Outside Member
(Department of Mechanical Engineering)

Supervisory Committee

Dr. Tao Lu, Supervisor
(Department of Electrical and Computer Engineering)

Dr. Chris Papadopoulos, Departmental Member
(Department of Electrical and Computer Engineering)

Dr. Peter Wild, Outside Member
(Department of Mechanical Engineering)

ABSTRACT

This thesis investigated single nanoparticle/molecule detections using a whispering gallery mode (WGM) microcavity, with focuses on sensing with the cavity optomechanical oscillation (OMO).

The high quality (Q) factor and small mode volume properties of a WGM microcavity make it possible to establish a strong intracavity power density with a small amount of input optical power. Such a high optical power density exerts a radiation pressure that is sufficient to push the cavity wall moving outward. The dynamic interaction between the optical field and the mechanical motion eventually results in a regenerative mechanical oscillation of the WGM cavity, which is termed as the optomechanical oscillation. With a high Q spherical microcavity, the observation of OMO in heavy water is reported. To the best knowledge of the author, this is the first demonstration of the cavity OMO in an aqueous environment.

Furthermore, by utilizing the properties of reactive sensing, cavity OMO, and optical spring effect, we demonstrated a new sensing mechanism that improves the WGM microcavity sensing resolution by several orders of magnitude. Finally, we conducted the demonstration of in-vitro molecule sensing by detecting single bindings of the 66 kDa Bovine Serum Albumin (BSA) protein molecules at a signal-to-noise ratio of 16.8.

Contents

Supervisory Committee **ii**

Abstract **iii**

Table of Contents **iv**

List of Figures **vi**

Acknowledgements **xi**

Dedication **xii**

1 Introduction **1**

1.1 Research overview 1

1.2 Organization 3

2 Whispering Gallery Mode Cavities **5**

2.1 Resonance mode 7

2.2 Mode volume 14

2.3 Quality factor 15

2.4 Optical coupling 18

2.5 Transmission spectrum 21

2.6 Intracavity buildup power and nonlinear effects 25

3 Cavity Reactive Sensing **31**

3.1 Sensing principle 31

3.2 System configuration 35

3.3 Peak resolution 38

3.4 Reference interferometer 40

3.5 In-line interferometer 40

3.6 Summary 45

4 Optomechanical Oscillation **48**
4.1 Radiation pressure 48
4.2 Cavity optomechanics 50
4.3 Optomechanical oscillation in an aqueous environment 55
4.4 Experiment results and discussions 57
4.5 Summary 67

5 Optical Spring Sensing **70**
5.1 Sensing principle 71
5.1.1 Optical spring effect 73
5.1.2 Mechanical frequency shift induced by particle binding 74
5.1.3 Cavity optomechanical transduction sensing resolution 75
5.1.4 Distinction from conventional mass sensing 76
5.2 Experiment realization 77
5.2.1 System setup 77
5.2.2 Device characterisation 79
5.2.3 Calibration of laser-cavity wavelength detuning 82
5.2.4 OMO frequency versus laser-cavity detuning 82
5.2.5 Allan deviation measurement of OMO frequency 88
5.3 Sensing performance 90
5.3.1 Silica nanoparticles detection 90
5.3.2 Single protein molecules sensing 94
5.4 Summary 96

6 Conclusion and Future Works **98**

A List of Publications **99**
A.1 Journal paper 99
A.2 Conference paper 100

Bibliography **101**

List of Figures

Figure 2.1 WGM microcavities: (a) Microdisk; (b) Microtoroid; (c) Microsphere (sideview) with a diameter around 100 μm; (d) The fundamental mode profile of the 100 μm diameter microsphere calculated numerically through the FEM. The mode pattern is presented with the intensity of the field that is confined by the cavity boundary near the equator. 6
Figure 2.2 The illustration of the resonance light propagating inside a WGM cavity. With a wavelength scanning input laser, the resonance wavelength λ_0 is identified by a transmission dip on the output spectrum. 8
Figure 2.3 The diagram of cylindrical coordinates with a toroid WGM microcavity. 11
Figure 2.4 The fundamental and high order transverse mode profiles of a 30-μ-radius microsphere from FEM simulation. 13
Figure 2.5 The normalized intensity plots along the radial direction across the cavity boundary with different surrounding media. The red curve represents the normalized intensity and the blue straight line indicates the interface between the cavity and its surrounding. (a) cavity in air; (b) cavity in water; (c) zoom in plot near the interface in air; (d) zoom in plot near the interface in water. 16
Figure 2.6 Schematic plot of the coupling between a WGM cavity and a waveguide coupler by the evanescent field. 19
Figure 2.7 Normalized transmission spectra for different couplings conditions. 23
Figure 2.8 Intra-cavity power as a function of the laser-cavity detuning by assuming the input power is 1 mW. 26
Figure 2.9 Dynamical thermo-optic effects of a cavity. Bottom: The input laser (blue) scans across the cavity resonance (red). Top: The broadened transmission spectrum from the thermal effects. . . 28

Figure 3.1 Schematic plot of the reactive sensing. The particle adsorbed on the cavity surface induces a change of the optical path length and leads to a shift of the cavity resonance wavelength. 32
Figure 3.2 The tapered fiber coupler is made by heating and pulling a single mode optical fiber on the customized fiber pulling stage. 36
Figure 3.3 The front view of the sensing configuration for a silica microshere coupled with a tapered fiber coupler above it. 37
Figure 3.4 The setup for the microspere sensing system with a reference interferometer connected in parallel. 39
Figure 3.5 The cavity transmission spectrum. Top: The cavity resonance shows quality factors of 2.1×10^8 for the resonance to the left and 3.8×10^8 for the resonance to the right; Bottom: Interferometer signal used to determine the resonance location and linewidth. . 41
Figure 3.6 Schematic plot of WGM sensing systems with in-line interferometers. (a) WGM sensor with a Mach-Zehnder interferometer in serial (b) WGM sensor with a Fabry-Pérot interferometer in serial 42
Figure 3.7 The transmission spectrum of WGM with a Fabry-Pérot interferometer in serial 44
Figure 3.8 The comparison of transmission fluctuations between the FPI and the conventional configuration. 46

Figure 4.1 Schematic plot showing the radiation pressure in an optical resonator. The radiation pressure causes the movement of the cavity boundary, therefore the output is modulated by the cavity osculation frequency Ω_m with a constant input power. 49
Figure 4.2 Experiment setup for the OMO measurements. 56
Figure 4.3 Transmitted optical power as a function of probe laser wavelength detune. At a dropped optical power close to the threshold power, the left inset displayed a sinusoidal spectrum while at a high dropped power the spectrum displayed in the right inset was distorted by the high order harmonics. 58
Figure 4.4 RF power spectrum of the reference interferometer output calibrated from the dark current spectrum. 59

Figure 4.5 Cavity transmitted optical power (blue trace) displays a Lorentzian shape. The laser frequency is calibrated through the transmitted signal of the reference interferometer (green trace). The red dashed lines are least square fitting results. 60
Figure 4.6 RF spectra at dropped power of 1.1 mW, 1 mW and 0.4 mW, least square fittings to the Lorentzian function indicate the linewidths of the optomechanical tones to be 232 Hz, 61 kHz and 269 kHz respectively. In the main plot, each spectrum was averaged over 100 spectral traces collected seamlessly at the same drop power level. The inset is the spectrum of single trace measurement. . 62
Figure 4.7 In a separate measurement, as high as 24-th order harmonics was observed in a frequency span of 10 MHz. The inset further displayed the spectrum with a frequency span set at 1 MHz. . . 63
Figure 4.8 Mechanical energy (normalized to the maximum value) as a function of the dropped power. The peak frequency as a function of the dropped power is displayed in the inset and a linear extrapolation predicts an intrinsic mechanical frequency of 198.7 kHz. 65
Figure 4.9 The plot of mechanical linewidth vs dropped power, which indicates an intrinsic mechanical linewidth of 431 kHz and an effective mechanical quality factor of $Q_{\mathrm{m}} = 0.5$ through the linear extrapolation. 66
Figure 4.10Spectrogram of the optomechanical oscillation indicates a 130 Hz standard deviation of the oscillation peak over a time span of 392 ms. 68

Figure 5.1 Schematic illustrating the sensing mechanism. A protein molecule bound to an optomechanically oscillating microsphere yields an optical resonance shift $\delta\lambda$, which is transduced to a mechanical frequency shift δf_{m}. The color map on the microsphere shows the radial breathing mechanical mode simulated by the finite element method. 72
Figure 5.2 Experiment setup for optomechanical transduction sensing. . . 78

Figure 5.3 The optical transmission spectrum of the microsphere immersed in DPBS, at a probe laser wavelength of 974 nm, with experimental data in blue and theoretical fitting in red. The input power is maintained low enough to characterize the intrinsic optical property of device, which exhibits an intrinsic optical Q of 4.8×10^6. 80
Figure 5.4 The optical transmission spectrum at an input laser power of 8.5 mW. The coherent OMO was excited with a threshold power of 3.0 mW dropped into the cavity. 81
Figure 5.5 The detailed spectrum of the fundamental oscillation tone, with experimental data in blue and theoretical fitting in red. The OMO exhibits a full-width at half maximum of 0.1 Hz, corresponding to an effective mechanical Q of 2.6×10^6. 83
Figure 5.6 An example of the power spectral density of the cavity transmission. The fundamental oscillation frequency is located at 262 kHz, with 6 high-order harmonics clearly visible on the spectrum. 84
Figure 5.7 Spectrogram of cavity transmitted signal as a function of laser wavelength detuning Δ'_λ (see Fig. 5.8 for the meaning of Δ'_λ), showing the detuning dependent mechanical frequency. The proportional frequency variations at the second and third harmonics are clearly visible. Every spectrum was averaged over 5 traces acquired continuously. 85
Figure 5.8 The OMO frequency as a function of laser-cavity wavelength detuning. The blue crosses show the experimental data and the grey curve shows the theory. The red curve is a polynomial fitting to the experimental data. The dashed circle indicates the operating regime for the particle and molecule sensing, with a frequency tuning slope of $df_\mathrm{m}/d\Delta_\lambda = -1.5$ kHz/fm at a laser-cavity detuning of $\Delta_\lambda = -70$ fm. Inset: Recorded dropped optical power as a function of laser wavelength detuning. This curve was used to obtain the real laser-cavity wavelength detuning $\Delta_\lambda = \lambda_l - \lambda_0$ where λ_l is the laser wavelength. 87

Figure 5.9 The two-sample Allan deviations of the fundamental, second and third harmonic tones measured in bare DPBS in the absence of sensing particle, showing a minimum deviation of 9.5 Hz at the fundamental oscillation tone. 89

Figure 5.10(a)-(d) Typical mechanical spectrograms for the binding events of silica beads with average radii of 11.6, 25, 50, and 85 nm, where (a) shows that of third harmonic and (b)-(d) show those of the fundamental oscillation frequency. (e)-(h) The histograms of the normalized frequency steps $\delta f_{\mathrm{m}}/f_{\mathrm{m}}$. 91

Figure 5.11The corresponding cavity resonance shifts induced by the particle binding as a function of bead radius. The color bars show the probability density functions of the recorded cavity resonance wavelength shifts induced by particle binding, where the bar width indicates the standard deviation of the bead size (provided by the manufacturer) and the color map indicates the magnitude of probability density. The red circles indicate the recorded maximum wavelength shifts of the cavity resonance. The dashed curve shows the theortical prediction. 93

Figure 5.12(a) A typical mechanical spectrogram recorded at the third harmonic of the oscillation tone, capturing the event of a BSA protein molecule detaching from the silica microsphere surface at 38 second, with a clear frequency step (inset) of -0.67 ± 0.04 kHz. (b) The histogram of the normalized frequency steps. (c) A mechanical spectrogram in the absence of protein molecules. (d) The histogram of the normalized frequency steps. 95

ACKNOWLEDGEMENTS

I would first like to thank my academic supervisor Prof. Tao Lu for all the guidance and support that he has provided throughout my research work at UVic. It is a great opportunity offered by him to let me work the topic of photonics and biosensing. His passion and intuition in scientific research always show me the right direction to the goal. He is open for discussion all the time, and his suggestions are very helpful for me to find the solutions when I am facing the difficulties during my research.

I would also like to express my deep gratitude to our collaborators Prof. Qiang Lin and Dr. Wei Jiang from University of Rochester for a lot of fruitful discussions and suggestions. I have truly learned a lot during our collaboration. It would be much more difficult for me to reach the success without their contributions.

Last but not least, I wish to thank my former and present group members: Steven Herchak, Xuan Du, Amin Cheraghi, Niloofar Sadeghi, Serge Vincent, Wen Zhou, Liao Zhang and so many people. It was a pleasure to work with them.

DEDICATION

To my parents

and

my wife

Chapter 1

Introduction

1.1 Research overview

An optical resonator confining light by the continuous total internal reflection (TIR), as oppose to a Fabry-Pérot cavity by the reflections between a pair of mirrors, is called whispering gallery mode (WGM) microcavity [1, 2]. Generally, a WGM microcavity is made of dielectric materials with an axial-symmetric structure in which the optical wave can circulate along its azimuthal direction. The quality factor (Q) and mode volume, whose definitions will be deferred to Chapter 2, are important quantities to characterize a WGM microcavity. A well fabricated silica WGM cavity can achieve an ultra high Q factor above two billion [3] and a mode volume as small as hundreds of λ^3, where λ is the confined light wavelength [4].

During the past several decades, researches on high Q WGM microcavities have been accelerated by scientists and engineers worldwide, with topics ranging from the fundamental physics to the engineering applications of different perspectives[5, 6, 7]. In particular, the prediction of a highly sensitive WGM cavity based biodetection was first proposed in 1995 [8], when Arnold and Griffel et. al. successfully observed the excitation of optical resonance with a dielectric microsphere in an aqueous environment for the first time. This so-called cavity reactive sensing mechanism relies on the dispersive nature of the optical resonance as the cavity resonance wavelength is perturbed by the changes of its surrounding environment [9, 10]. Since then, many progresses have been made and single particle biosensors have been developed on different WGM platforms. Up to date, the sensitivity of a plain passive optical microcavity can detect single polystyrene nanobeads as small as 12.5-nm in radius in

an aqueous environment [11]. This is four times smaller in volume than the influenza A virus [12, 13]. However, the physical limitation from the cavity loss restricts the further narrowing of optical resonance linewidth, on which the microresonator sensitivity critically depends. To reach the single molecule sensitivity, researchers have explored several different approaches, such as the active sensing with rare earth doped cavities and the local signal enhancement with additional plasma structures on cavity surface [14, 15, 16, 17]. These technologies enable the detection of a single molecule at the extra cost of complicated fabrication processes or sensing efficiency reduction by orders.

In parallel, a high Q WGM microcavity can establish strong intracavity optical power with a milli-Watts-power pump source when on-resonance [18, 19, 20, 21]. Therefore, the optical wave continuously launched into a cavity can produce a radiation pressure onto the cavity wall to excite the mechanical motion. This induced mechanical motion changes the optical path of the resonator and thus shifts the optical resonance wavelength, which in turn modulates the optical field inside the cavity. When the accumulated power is above a threshold value, the radiation force will amplify the mechanical motion, leading to the coherent regenerative oscillation of the device. This is the cavity optomechanical oscillation (OMO).

The cavity optomechanics has been a research focus since its first demonstration in 2005 [22, 19, 18]. The oscillator has the similar properties as the micro/nano-electromechanical system (MEMS/NEMS) based sensors [23], except that both the driving and reading of the OMO are performed optically. According to Hooke's law that the mechanical eigen frequency (Ω_{m}) of a solid object follows $\Omega_{\mathrm{m}} = \sqrt{k/m}$, where k is the spring constant and m is the effective mass of the corresponding oscillation mode. The mass sensing is achieved by monitoring the mechanical frequency (Ω_{m}) shift induced by the mass (m) change from particle binding [24, 25, 26]. However, researches showed that the OMO mass sensing capability is limited by the relatively large effective mass [27]. Note that for the fundamental mechanical oscillation mode, a typical WGM cavity such as a 72-μm-diameter silica microtoroid has an effective mass of 3.3×10^{-8} kg [22]. As the fundamental oscillation frequency shift from the added particle mass is at 72-266 Hz/pg, such sensor can only detect sub-pg or 1-μm diameter silica particle [28, 29], as oppose to the record detection of 10-nm gold particles in suspensions using NEMS based mass sensing [30].

In this dissertation, we present a novel cavity transduction sensing mechanism coupled with the OMO. Instead of tracing the frequency dependence with the effective

mass, we monitor the mechanical frequency shift of a microcavity transduced from its optical resonance shift. Physically, the affected optical mode can modify the effective stiffness of a microcavity through the radiation force, by tuning the optical spring constant of the OMO. This unique effect existing in the cavity optomechanics is called optical spring effect [31]. Our experiments illustrate that this cavity optical spring sensing technique provides an outstanding sensitivity that can detect a single Bovine Serum Albumin (BSA) protein molecule at a signal-to-noise ratio of 16.8, with a plain dielectric cavity immersed in water. For the experimental demonstration, a cavity that can oscillate in an aqueous environment is a prerequisite, which is necessary to many applications in life science. We implemented the cavity optomechanical oscillation with a silica microsphere cavity immersed in liquid for the first time. The power spectra of the output signal from the cavity displays a stable and narrow bandwidth OMO along with its high order harmonics. Using silica nanobeads of different sizes as sensing particles, we demonstrated that the sensor on this principle set a new record of sensitivity among all plain microcavity sensors.

1.2 Organization

Chapter 2 is an introduction to the dielectric WGM microcavity. It provides the basic properties of the optical resonator that are related to this work, which include the quality factor, optical mode volume, and light coupling condition. Besides, the analysis of the optical transmission and the power buildup inside a cavity are presented in detail.

Chapter 3 describes the general principle of the cavity reactive sensing, which has a strong dependency with the WGM resonance. The system configuration and experimental details for single particle detections on a silica microsphere platform is also provided. Additionally, we demonstrate the sensitivity improvement by implementing a simple reference interferometer in serial.

Chapter 4 describes the cavity optomechanical effects and for the first time demonstrates the coherent, regenerative optomechanical oscillation with a high Q microsphere in an aqueous environment.

Chapter 5 proposes a new sensing mechanism that detects particle bindings based on the optical spring effect. We demonstrate an improvement of sensitivity by orders of magnitude compared to the conventional reactive sensing or mechanical mass sensing.

Chapter 6 serves as a briefed summary of the author's work and discusses the future research.

Chapter 2

Whispering Gallery Mode Cavities

The optical whispering gallery mode microcavity is named after the circular gallery of St Paul's Cathedral in London, where the creeping acoustic wave makes a whisper audible from any location near the gallery wall [32]. Its optical counterpart, the WGM microcavity can form the optical resonance through the continuous total internal reflection (TIR) at its circular edge. It is easy to reduce the WGM cavity size into micrometer scale while maintaining the high quality factor (Q), which is a dimensionless factor that quantifies the light confinement of an optical cavity [33].

The first observation of the optical WGM phenomenon dates back to 1977 [34]. In that experiment, a liquid droplet WGM with a quality factor (Q) of 10^6 was reported. In 1989, Braginsky et al. first demonstrated the ultrahigh Q ($Q \simeq 10^8$) WGM with a solid dielectric mcirosphere [1]. A record quality factor was later achieved at $Q = (0.8 \pm 0.1) \times 10^{10}$ by the same group [35].

By the beginning of this century, researchers have developed various ultrahigh Q (defined as Q$> 10^8$) WGM cavities. These include the microdisk, microtoroid, and microsphere, etc, as shown in Fig. 2.1. Most of these microcavities are fabricated with silica because of the low optical absorption, while alternative materials including silicon [36], CaF_2 [37, 38], $LiNbO_3$ [39], and active medium doped silica [40, 41] etc., are also used. Among them, the silica microdisk is one of the first on-chip WGM demonstrated [42]. The disk is fabricated by the standard photolithography/HF wet chemical etching procedure on a silica-on-silicon (SoS) wafer, followed by the XeF_2 dry etching to selectively under-cut the silicon and form a pillar to support the silica microdisk. Although it is a promising on-chip device, extra efforts are required to achieve the ultrahigh Q due to the scattering loss from the etch-induced imperfection at the edge [43]. By heating the disk with a high power CO_2 laser, the

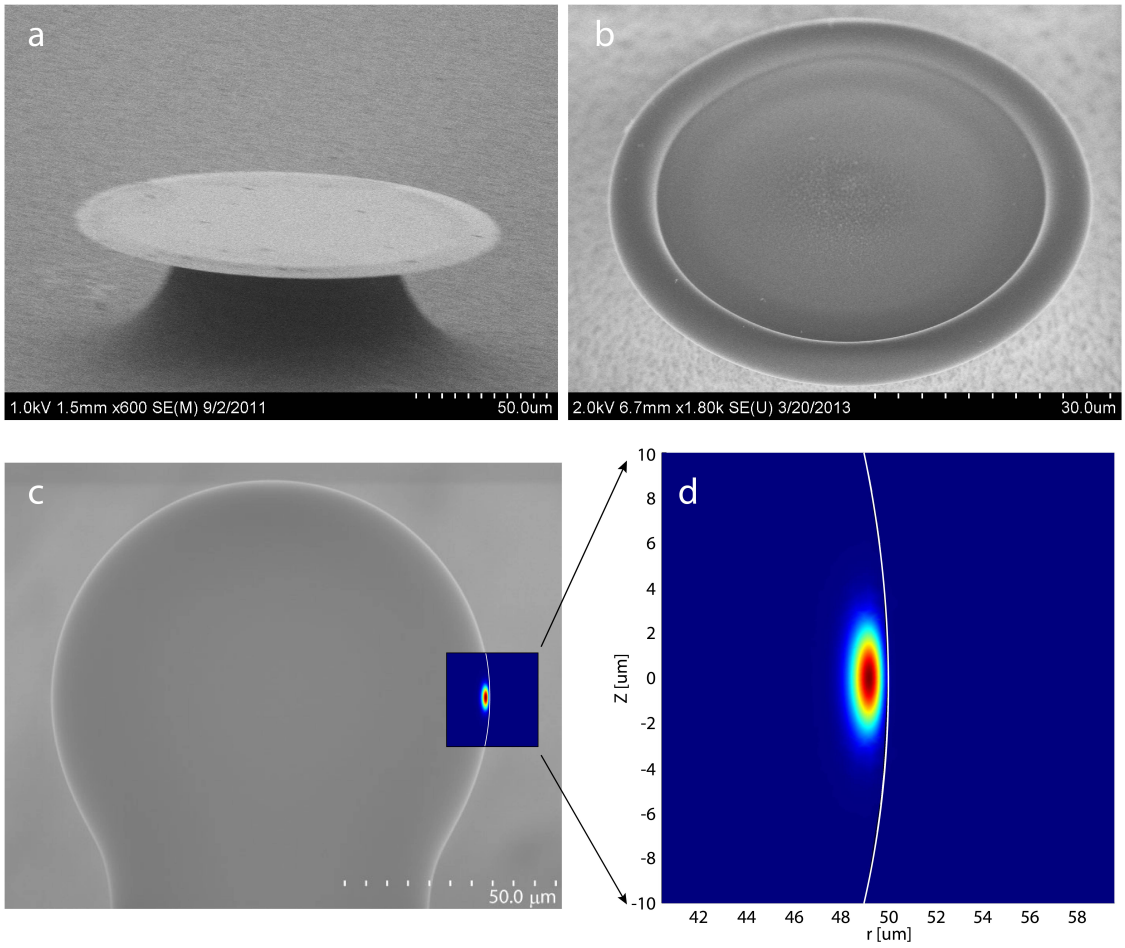

Figure 2.1: WGM microcavities: (a) Microdisk; (b) Microtoroid; (c) Microsphere (sideview) with a diameter around 100 μm; (d) The fundamental mode profile of the 100 μm diameter microsphere calculated numerically through the FEM. The mode pattern is presented with the intensity of the field that is confined by the cavity boundary near the equator.

silica microdisk will be reflowed to a donut shape silica toroid around the pillar with a smooth surface [4]. This is the microtoroid cavity as shown in Fig. 2.1(b). Similar procedure is applied to the fabrication of microsphere cavity (c.f. Fig. 2.1(c)), where the tip of a tapered optical fiber rather than a disk is reflowed by a CO_2 laser. After the laser reflow, a 100-μm-diameter ultrahigh Q silica microsphere is formed. It is worth mentioning that with the advancement of fabrication technology, silica disks of Q as high as 875 million has been reported [43]. The related fabrication process, although removes the necessity of the reflow process for Q improvement, is still at experimental stage and requires sophisticated steps compared to the conventional method. In this thesis, the author's work focuses on the spherical microcavities. However, the work can be generalized to other WGM platforms.

2.1 Resonance mode

Confined by the TIR, the light circulating inside a WGM cavity forms a closed trajectory near the periphery of the cavity equator. Therefore, its optical path length (L_{op}) per one round trip is approximately $L_{\text{op}} \approx 2\pi rn$. Here r is effective radius of the WGM, n is the refractive index of the cavity. Once on resonance, the propagating light experiences the constructive interference, or equivalently, all photons at the same azimuthal cross section are synchronized in phase. That is, the photons keep the same phase and momentum after each complete round trip except for a small loss during the propagation. This leads to the resonance condition of a WGM as illustrated in Fig. 2.2

$$L_{\text{op}} = m\lambda_0, \tag{2.1}$$

where m is an integer azimuthal mode number and λ_0 is the resonance wavelength of the corresponding mode. The resonance wavelength of the mode can be identified from the cavity output transmission spectrum by linearly scanning the wavelength of an input laser near the cavity resonance. The transmission intensity drops to a minimal value at the cavity resonance wavelength, while $\Delta\lambda$ represents the linewidth of the cavity resonance whose value is equal to the full-width-half-maximum (FWHM) of the resonance dark peak.

From the Maxwell's equations, the electromagnetic field inside a charge and cur-

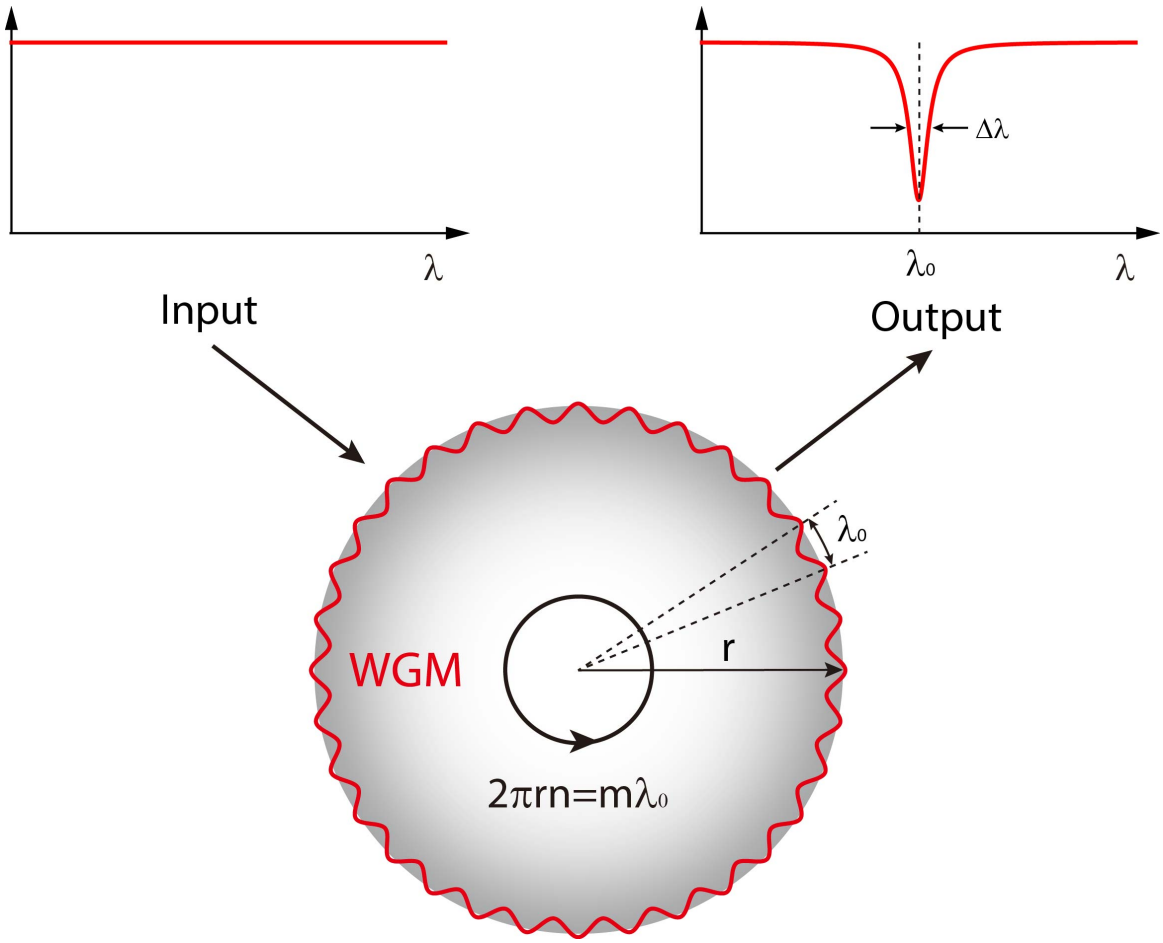

Figure 2.2: The illustration of the resonance light propagating inside a WGM cavity. With a wavelength scanning input laser, the resonance wavelength λ_0 is identified by a transmission dip on the output spectrum.

rent free medium such as the dielectrics follows [44]

$$\nabla \cdot \mathbf{D}(\mathbf{r},t) = 0 \tag{2.2}$$

$$\nabla \times \mathbf{E}(\mathbf{r},t) = -\frac{\partial \mathbf{B}(\mathbf{r},t)}{\partial t} \tag{2.3}$$

$$\nabla \cdot \mathbf{B}(\mathbf{r},t) = 0 \tag{2.4}$$

$$\nabla \times \mathbf{H}(\mathbf{r},t) = \frac{\partial \mathbf{D}(\mathbf{r},t)}{\partial t} \tag{2.5}$$

where $\mathbf{D}(\mathbf{r},t)$ is the electric displacement field, $\mathbf{E}(\mathbf{r},t)$ is the electric field, $\mathbf{B}(\mathbf{r},t)$ is the magnetic field and $\mathbf{H}(\mathbf{r},t)$ is the magnetizing field. For a microcavity system, the medium is piece-wise homogeneous such that $\mathbf{D}(\mathbf{r},t) = \epsilon\mathbf{E}(\mathbf{r},t)$ and $\mathbf{H}(\mathbf{r},t) = \frac{1}{\mu}\mathbf{B}(\mathbf{r},t)$, where ϵ and μ are the permittivity and permeability respectively.

Taking the curl of Eq. 2.3 and Eq. 2.5 on both sides that

$$\begin{cases} \nabla(\nabla \cdot \mathbf{E}(\mathbf{r},t)) - \nabla^2\mathbf{E}(\mathbf{r},t) = -\mu\frac{\partial}{\partial t}(\nabla \times \mathbf{H}(\mathbf{r},t)) \\ \nabla(\nabla \cdot \mathbf{H}(\mathbf{r},t)) - \nabla^2\mathbf{H}(\mathbf{r},t) = \epsilon\frac{\partial}{\partial t}(\nabla \times \mathbf{E}(\mathbf{r},t)) \end{cases}, \tag{2.6}$$

we can reduce the four Maxwell's equations to a set of wave equations by substituting the Maxwell's equations into Eq. 2.6

$$\begin{cases} \nabla^2\mathbf{E}(\mathbf{r},t) = \mu\epsilon\frac{\partial^2\mathbf{E}(\mathbf{r},t)}{\partial t^2} \\ \nabla^2\mathbf{H}(\mathbf{r},t) = \mu\epsilon\frac{\partial^2\mathbf{H}(\mathbf{r},t)}{\partial t^2} \end{cases}. \tag{2.7}$$

Consequently, the time and space terms of both E and H fields can be separated as $F(\mathbf{r},t) = F(\mathbf{r})\Psi(t)$ where F is any component of E and H. Further any sub equations of Eq. 2.7 can be rearranged to

$$\frac{1}{F(\mathbf{r})}\nabla^2 F(\mathbf{r}) = \mu\epsilon\frac{1}{\Psi(t)}\frac{\partial^2\Psi(t)}{\partial t^2} \tag{2.8}$$

Note L.H.S. of Eq. 2.8 only operates on position while R.H.S. on time. As a result, the set of partial differential equations holds only when both sides equals to a time/space independent constant. Therefore, we obtain

$$\begin{cases} \mathbf{E}(\mathbf{r},t) = \mathbf{E}(\mathbf{r})e^{j\omega t} \\ \mathbf{H}(\mathbf{r},t) = \mathbf{H}(\mathbf{r})e^{j\omega t} \end{cases}, \tag{2.9}$$

where ω is the angular frequency of the electromagnetic wave. After cancelling the time dependent term ($e^{j\omega t}$) on both sides in Eq. 2.7, we obtain the time independent Helmhöltz equations [45],

$$\begin{cases} \nabla^2\mathbf{E}(\mathbf{r}) + [k_0 n(\mathbf{r})]^2\mathbf{E}(\mathbf{r}) = 0 \\ \nabla^2\mathbf{H}(\mathbf{r}) + [k_0 n(\mathbf{r})]^2\mathbf{H}(\mathbf{r}) = 0 \end{cases}. \tag{2.10}$$

Here, the electric field $\mathbf{E}(\mathbf{r})$, magnetic field $\mathbf{H}(\mathbf{r})$, and the refractive index $n(\mathbf{r})$ are all variables of the position vector $\mathbf{r}$. $k_0 = 2\pi/\lambda$ is the wave number of the light in free space, in which λ represents the light wavelength.

In order to take the advantage of the WGM rotational symmetry, it is more convenient to solve the equations in the cylindrical coordinates (ρ, ϕ, z) as shown in Fig. 2.3. Consequently, the above Laplace operator is presented in the form of cylindrical coordinates as

$$\nabla^2 = \frac{1}{\rho}\frac{\partial}{\partial\rho}(\rho\frac{\partial}{\partial\rho}) + \frac{1}{\rho^2}\frac{\partial^2}{\partial\phi^2} + \frac{\partial^2}{\partial z^2}. \tag{2.11}$$

Correspondingly, the components of vector field $\mathbf{E}(\mathbf{r})$ and $\mathbf{H}(\mathbf{r})$ are projected onto the cylindrical coordinates. For instance, the expression of the magnetic field is

$$\mathbf{H}(\mathbf{r}) = H^\rho\widehat{\rho} + H^\phi\widehat{\phi} + H^z\widehat{z}. \tag{2.12}$$

Substituting the above expression back into the Helmhöltz equation (2.10), we get three separated equations for the corresponding components in the coordinates

$$\begin{cases} \left[\rho\frac{\partial}{\partial\rho}(\rho\frac{\partial}{\partial\rho}) + \rho^2\frac{\partial^2}{\partial z^2} - 1\right] H^\rho - 2\frac{\partial H^\phi}{\partial\phi} + \rho^2[k_0 n(\mathbf{r})]^2 H^\rho = -\frac{\partial^2}{\partial\phi^2}H^\rho & \text{(2.13a)} \\ \left[\rho\frac{\partial}{\partial\rho}(\rho\frac{\partial}{\partial\rho}) + \rho^2\frac{\partial^2}{\partial z^2} - 1\right] H^\phi + 2\frac{\partial H^\rho}{\partial\phi} + \rho^2[k_0 n(\mathbf{r})]^2 H^\phi = -\frac{\partial^2}{\partial\phi^2}H^\phi & \text{(2.13b)} \\ \left[\rho\frac{\partial}{\partial\rho}(\rho\frac{\partial}{\partial\rho}) + \rho^2\frac{\partial^2}{\partial z^2}\right] H^z + \rho^2[k_0 n(\mathbf{r})]^2 H^z = -\frac{\partial^2}{\partial\phi^2}H^z & \text{(2.13c)} \end{cases}$$

Here $2\frac{\partial H^\phi}{\partial\phi}$ and $2\frac{\partial H^\rho}{\partial\phi}$ are the small radiation loss part that has little contribution to form the high Q WGM, therefore they are negligible in calculating the resonance mode. In particular, for the piece-wise homogeneous WGM microcavity, although the refractive index $n(\mathbf{r})$ depends on the position as well, it is invariant along the azimuthal direction (ϕ) due to the rotational-symmetric structure of the cavity. There-

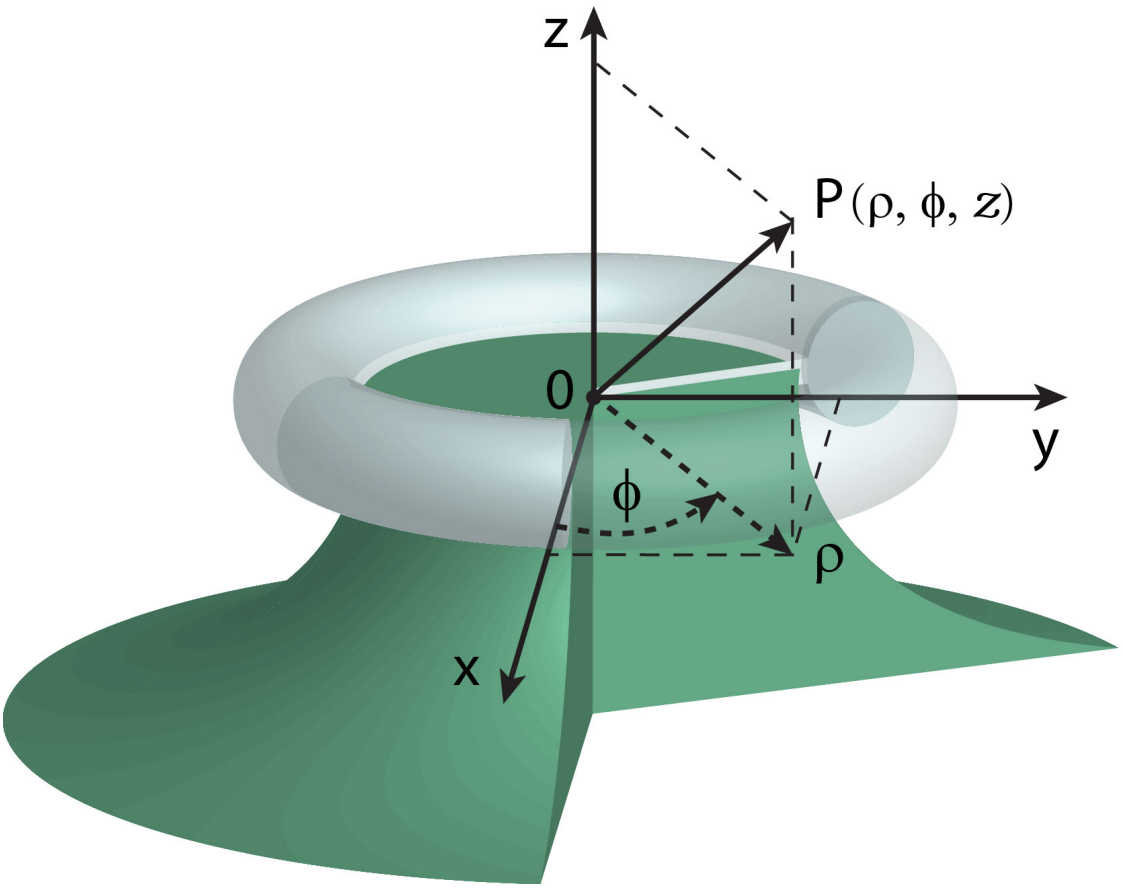

Figure 2.3: The diagram of cylindrical coordinates with a toroid WGM microcavity.

fore in Eq. 2.13, L.H.S. have no dependence on ϕ while R.H.S. only operate on ϕ, leading to the separation of variables

$$H^z(\rho, \phi, z) = H^z(\rho, z)\Phi(\phi). \tag{2.14}$$

After dividing both sides of Eq. 2.13c by the H^z component, we obtain

$$\frac{1}{H^z(\rho,z)}\left[\rho\frac{\partial}{\partial\rho}(\rho\frac{\partial}{\partial\rho}) + \rho^2\frac{\partial^2}{\partial z^2}\right]H^z(\rho,z) + \rho^2 n(\rho,z)^2 k_0^2 = -\frac{1}{\Phi(\phi)}\frac{\partial^2}{\partial\phi^2}\Phi(\phi) \tag{2.15}$$

Eq. 2.15 holds only if its both sides equal a position independent constant m^2 and leads to the separation of variables for the field component with $e^{jm\phi}$ term. Apply the similar treatment onto the rest components of the electromagnetic field to obtain

$$\begin{cases} \mathbf{E}(\mathbf{r}) = \mathbf{E}(\rho,z)e^{jm\phi} \\ \mathbf{H}(\mathbf{r}) = \mathbf{H}(\rho,z)e^{jm\phi} \end{cases}. \tag{2.16}$$

Here, it is worth pointing out that m is actually a complex number whose imaginary part represents all kinds of optical loss during the light propagating within the cavity, while its real part (m_r) is the integer number for the corresponding azimuthal mode, according to the single value condition that

$$e^{j2\pi m_\mathrm{r}} = 1. \tag{2.17}$$

Utilizing Eq. 2.14, the Helmhöltz equations (2.10) are reduced as

$$\begin{cases} \nabla_\perp^2\mathbf{E}(\rho,z) + \left[k_0^2 n(\rho,z)^2 - \left(\frac{m}{\rho}\right)^2\right]\mathbf{E}(\rho,z) = 0 \\ \nabla_\perp^2\mathbf{H}(\rho,z) + \left[k_0^2 n(\rho,z)^2 - \left(\frac{m}{\rho}\right)^2\right]\mathbf{H}(\rho,z) = 0 \end{cases}, \tag{2.18}$$

with the transverse Laplace operator $\nabla_\perp^2 = \nabla^2 - \frac{1}{\rho^2}\frac{\partial^2}{\partial\phi^2} = \frac{1}{\rho}\frac{\partial}{\partial\rho}(\rho\frac{\partial}{\partial\rho}) + \frac{\partial^2}{\partial z^2}$. Therefore, one can simplify the numerical calculation from 3D to 2D [46].

The reduced Helmhöltz equations can be solved numerically through the finite element method (FEM) [47, 48]. Fig. 2.4 shows the optical mode profiles for a set of WGMs computed by COMSOL, a FEM simulation software. Here, a 30-μm-radius silica microsphere in free space is simulated. Its resonance wavelength is around 970 nm and the corresponding azimuthal mode order $m = 272$. There are multiple

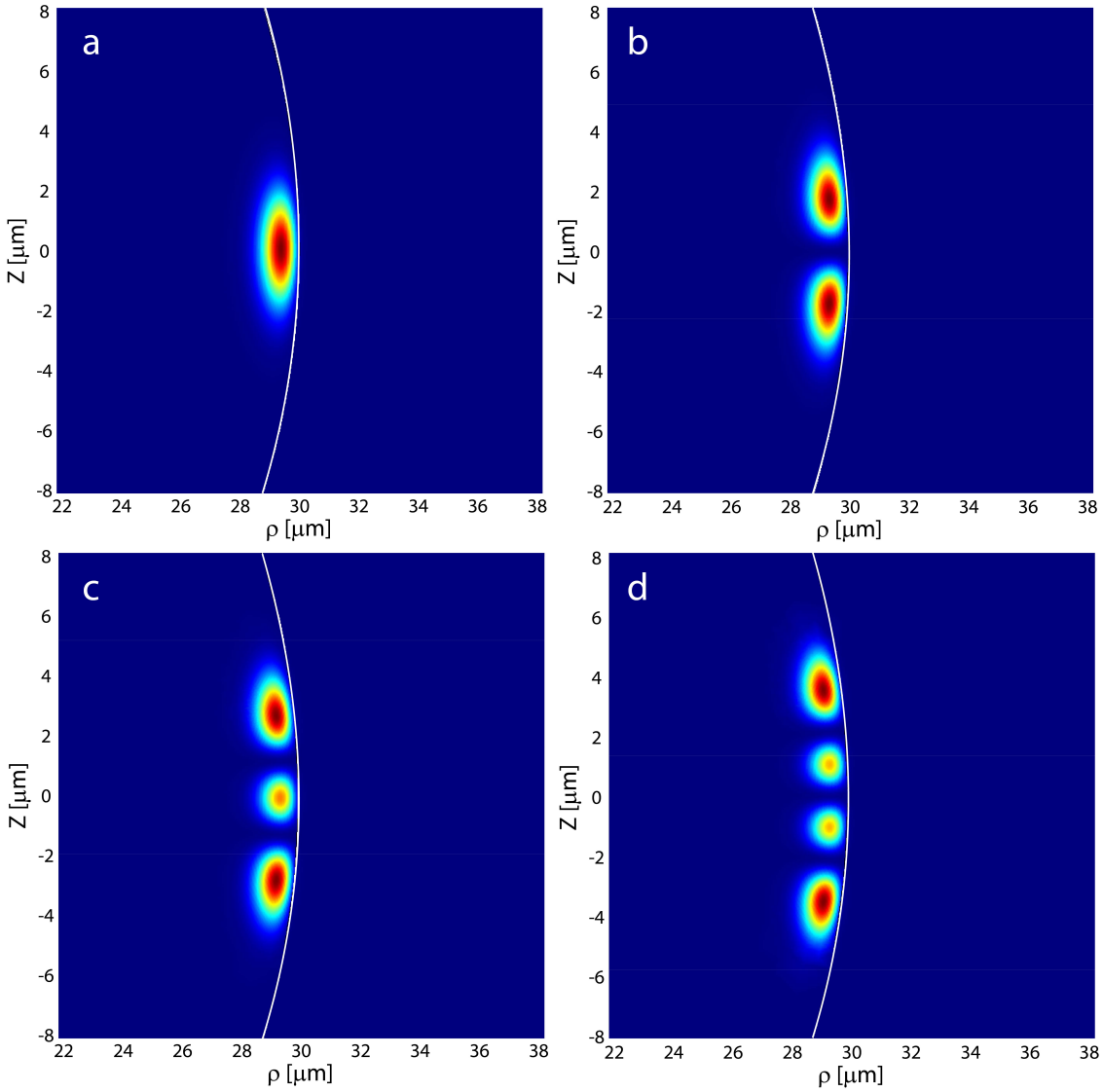

Figure 2.4: The fundamental and high order transverse mode profiles of a 30-μ-radius microsphere from FEM simulation.

high order transverse modes existing with the fundamental mode (Fig. 2.4a) that has the largest resonance wavelength for a given azimuthal mode number. As expected, the optical wave is propagating close to the boundary at the cavity equator. The spherical geometry leads to a stronger confinement of the optical field along the radial direction than that of the axial direction.

2.2 Mode volume

Although most of the light is circulating inside the dielectric cavity, there is still a small part of light propagating in the surrounding medium, which is known as the evanescent field. The evanescent wave is a result of the continuity condition of the electromagnetic field at the interface where the total internal reflection (TIR) occurs [44]. It exponentially decays along the radial direction from cavity surface. It is the evanescent part of the optical mode that sensitively experiences the change of surrounding media, since the evanescent field is travelling through the area where the local refractive index of the surrounding changes.

The physical size of the optical mode confined in a cavity is characterized by the parameter called mode volume [49],

$$V_{\mathrm{m}} = \frac{\int \epsilon_{\mathrm{r}}(\mathbf{r})|\mathbf{E}|^2 dV}{|\mathbf{E}_{\mathrm{max}}|^2}, \tag{2.19}$$

where $\epsilon_{\mathrm{r}}(\mathbf{r})$ is the permittivity, $|\mathbf{E}_{\mathrm{max}}|$ is the magnitude of maximum electric field strength of the optical mode, and the integral is taken over the full space. According to Eq. 2.19, one can estimate that the mode volume of a 50-μm-radius microsphere is around 1,000 $\mu\mathrm{m}^3$. The small mode volume, compared to the Fabry-Pérot cavity, is one of unique advantages of the WGM microcavity, leading to the higher energy density given a fixed intracavity power. In order to obtain a higher power density, a WGM microcavity with a compact mode volume is preferable in some applications, such as the nonlinear optics [5, 50].

The mode volume, which determines the space confinement of an optical cavity, has a strong dependence on the cavity geometry. A smaller cavity provides a more compact optical mode with smaller volume, leading to more optical power distributed into the evanescent field. Therefore, it is expected to find a larger amount of evanescent field surrounding the smaller cavity. Besides, the cavity shape plays a role in the mode volume. For example, the microsphere has a relatively larger mode volume than

the microtoroid with similar diameter, as the microtoroid has a stronger confinement along the vertical direction.

In addition, the surrounding media can also affect the distribution of the optical mode through modifying the refractive index contrast between the cavity and its surrounding. Generally, a smaller difference of indices leads to a weaker light confinement in space. For the purpose of illustration, we provide the normalized intensity profiles along the radial direction for a same silica microcavity surrounded by air and water in Fig. 2.5.

Fig. 2.5(a) shows the intensity distribution of the fundamental transverse mode (red trace) along the radial direction of a cavity in air while Fig. 2.5(b) is of the same cavity but immersed in water. In each plot, the blue straight line indicates the interface between the cavity and its surrounding medium. As the resonance wavelength is around 970 nm, the refractive index of water ($n_{\text{water}} = 1.33$) [51] is approximately 30% higher than that of air ($n_{\text{air}} = 1.0$), which leads to a smaller refractive indices contrast and a subsequent weaker confinement to the optical field. Therefore, the center of the cavity mode is closer to the boundary and a larger portion of the light leaks to water.

A closer comparison between the mode profiles shown in Fig.2.5(c) and (d), shows the evanescent pattern is broadened along the radial direction in the aqueous environment. It is the evanescent part that has more interaction with the surrounding environment, so it can be used to deliver the optical information or detect the change of the environment. For instance, the communication between a WGM cavity and a waveguide is realized through the evanescent field coupling. In addition, once there is a particle attached within the evanescent field at the cavity surface, it triggers a sudden change of the cavity resonance, whose amplitude depends on the size and property of the adsorbed particle.

2.3 Quality factor

Besides the space confinement, the temporal confinement of light provides a long life time to the circulating photons, which can be characterized by the cavity quality factor (Q) [6]. The Q is defined as the total energy stored in the cavity divided by the energy loss per resonance cycle, which can be expressed as

$$Q = 2\pi f_0 \times \frac{E_{\text{stored}}}{P_{\text{loss}}} = \omega_0 \tau. \tag{2.20}$$

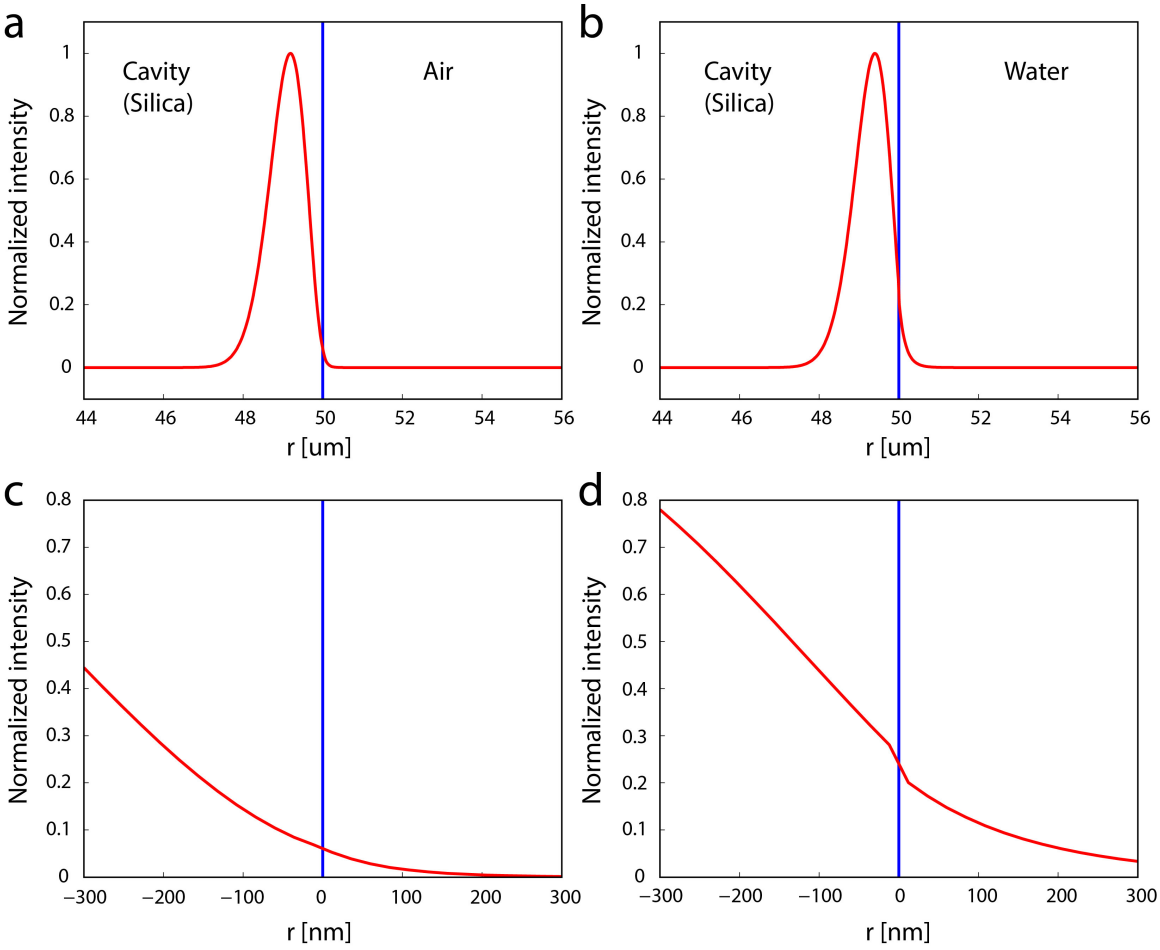

Figure 2.5: The normalized intensity plots along the radial direction across the cavity boundary with different surrounding media. The red curve represents the normalized intensity and the blue straight line indicates the interface between the cavity and its surrounding. (a) cavity in air; (b) cavity in water; (c) zoom in plot near the interface in air; (d) zoom in plot near the interface in water.

Here, f_0 is the optical resonance frequency, $\omega_0 = 2\pi f_0$ is the corresponding angular frequency and τ is the life time of the circulating photon before escaping. Thus, one can obtain the cavity Q factor through measuring the photon life time[52], which is usually used to measure the cavity Q higher than 100 million.

According to energy dissipating mechanism, when a cavity coupled with an external probe such as a waveguide or prism, the total Q factor can be divided into several approximately independent components, including the material absorption loss Q_{mat}, the radiation loss Q_{rad}, the surface scattering loss Q_{ss}, the contamination loss Q_{con} and the coupling loss Q_{c}. When there is no light coupled out from the cavity to a coupler ($Q_{\mathrm{c}} = 0$), the total loss equates the cavity intrinsic loss Q_0 which is used to characterize the quality of an optical resonator. The relation of the Q factors can be described by the following equation

$$\begin{aligned} \frac{1}{Q_{\mathrm{total}}} &= \frac{1}{Q_0} + \frac{1}{Q_{\mathrm{c}}} \\ &= \left(\frac{1}{Q_{\mathrm{mat}}} + \frac{1}{Q_{\mathrm{rad}}} + \frac{1}{Q_{\mathrm{ss}}} + \frac{1}{Q_{\mathrm{con}}}\right) + \frac{1}{Q_{\mathrm{c}}}. \end{aligned} \tag{2.21}$$

Here Q_{mat} represents the light loss due to the absorption of the cavity material and its surrounding medium. It depends on both the light frequency and the material properties. For example, the silica has a very low absorption to the 1550 nm light [53]. However, this wavelength is not a suitable candidate for biosensing, as the water is strongly absorptive at this wavelength [51]. An optical source operating in the visible spectrum range is preferable in this scenario because of the much lower loss in water. The Q_{rad} is the loss due to the radiation and is more significant to a smaller cavity. When the cavity size is small, the cavity confinement to the light becomes weaker, causing substantial photon leakage. According to the Rayleigh criterion [54], the detectable resonance shift should be larger than the minimal distance of two distinguishable peaks, whose linewidths are inversely proportional to the Q. The low Q due to the high radiation loss causes a broad linewidth, resulting an increment of the minimal distance. Although a smaller cavity with a shorter optical path is more sensitive for the apportioned resonance shift due to the local perturbation, one cannot infinitely reduce its size since it will lose the spectral resolution because of the low Q. The Q_{ss} is the light scattering loss induced by the cavity surface roughness. The reflowed silica cavity can dramatically reduce the scattering loss, as the interface formed by surface tension has a extremely low roughness by nature. The contamina-

tion loss Q_{con} must always be avoided by handling the cavity carefully in each step during an experiment.

2.4 Optical coupling

In order to excite or probe the whispering galley mode, a tapered fiber waveguide is implemented as an optical waveguide [55]. The guided optical wave in the taper interacts with the microcavity through the evanescent field. The fiber taper has a better coupling efficiency than other couplers, such as the prism and side polished fiber [56, 57, 58, 59]. The critical coupling between a fiber taper and a cavity has been demonstrated experimentally, which is critical to the power dependent nonlinear optical effects [60, 61].

Assuming a WGM microcavity with a resonance frequency of ω_0 is pumped by an external laser source with an optical frequency ω through a tapered fiber coupler, the cavity mode with an amplitude $a_0(t)$ is normalized to the cavity power such that $P_{\text{w}} = |a_0(t)|^2 = a_0^*(t)a_0(t)$. Similarly, the amplitude $b_0(t)$ of transmit waveguide mode in the fiber coupler is normalized to the input power that $P_{\text{f}} = |b_0(t)|^2$. Therefore, the corresponding slow varying mode amplitude for the cavity and coupler can take the form as following: $a(t) = a_0(t)e^{j(\omega-\omega_0)t}$ and $b(t) = b_0(t)e^{j(\omega-\omega_0)t}$.

Using the above normalized amplitudes to represent the optical modes, the coupling between a WGM cavity and a fiber coupler through the evanescent field can be described by the following equation [62],

$$a(t) = jTb(t) + Ra(t-\tau_{\text{c}})e^{j\frac{2\pi n_{\text{e}}L}{\lambda}}e^{-\frac{\alpha_0 L}{2}}, \tag{2.22}$$

where $a(t)$ is the amplitude of the cavity mode and $b(t)$ is the amplitude for the taper mode; n_{e} is the effective refractive index; L is the length of one complete round trip that the light has travelled through; $\tau_{\text{c}} = n_{\text{e}}L/c$ is the roundtrip time of the circulating light; α_0 is the linear attenuation due to the loss. As Fig. 2.1(a) shows that the optical mode is propagating closely to the equator of the cavity, the round trip length L is approximately equal to the cavity circumference $2\pi r$. For simplicity, here we assume that both the cavity and coupler operate in single transverse mode. We further assume that the reflection loss at the coupling junction is negligible, so the coupling coefficient T and reflection coefficient R hold the relation $|T|^2+|R|^2 = 1$. Eq. 2.22 indicates that the field of a cavity mode $a(t)$ is composed of two parts. The

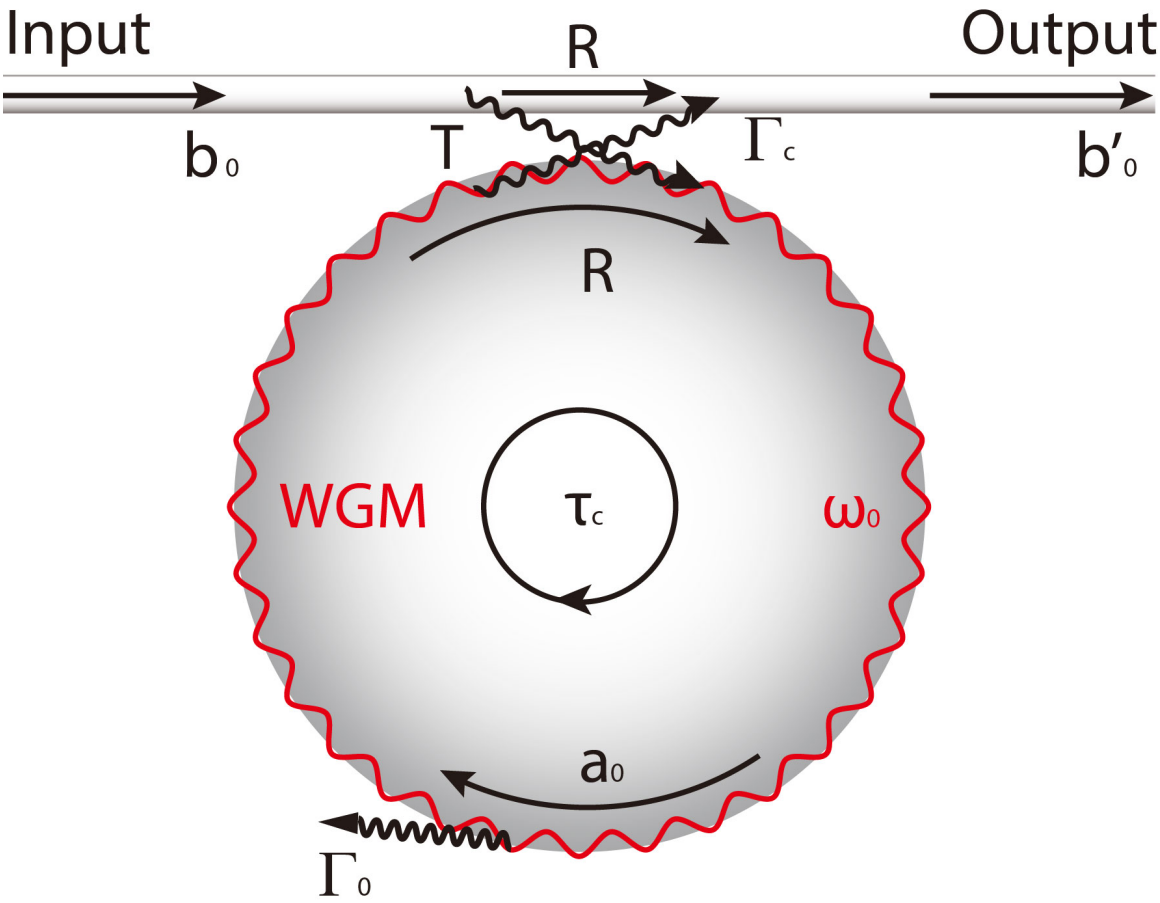

Figure 2.6: Schematic plot of the coupling between a WGM cavity and a waveguide coupler by the evanescent field.

first term at the right hand side of the equation represents the field coupled from the fiber taper while the second term represents the reflected cavity mode from the boundary at the coupling junction.

Further, taking the expansion of the retarded cavity mode term into consideration and assuming $\tau_c << t$

$$a(t-\tau_c) = a(t) - \tau_c \frac{da(t)}{dt}. \tag{2.23}$$

By cancelling the frequency detuning term $e^{j(\omega-\omega_0)t}$ on both sides, the governing equation for the mode amplitudes can be rewritten as below

$$a_0 = jTb_0 + R[a_0 - \tau_c \frac{da_0}{dt} - \tau_c j(\omega-\omega_0)a_0]e^{j\frac{2\pi n_e L}{\lambda}} e^{-\frac{\alpha_0 L}{2}}. \tag{2.24}$$

According to the resonance condition of WGM, the closed optical path length must be m_r multiple of the resonance wavelength λ_0 where the mode number $m_r \approx n_e L/\lambda_0$. Therefore, $e^{j\frac{2\pi n_e L}{\lambda}} \approx e^{j2\pi n_e L/\lambda_0} = 1$ when the laser wavelength λ is close to the cavity resonance wavelength λ_0, which leads to

$$\frac{da_0}{dt} + \frac{1}{\tau_c}(\frac{1}{R}e^{\frac{\alpha_0 L}{2}} - 1)a_0 + j(\omega-\omega_0)a_0 = jCb_0. \tag{2.25}$$

Here, we use a mode matching parameter $C = T/R\tau_c e^{\alpha_0 L/2}$ to describe the coupling matching between the coupler mode and the resonator mode. Considering that the mode coupling between the cavity and taper is through the evanescent field that is within a small fraction of the total field, typically less than one percent. Therefore, the reflection coefficient can be expressed as $1/R \approx 1/(1-T^2/2) \approx 1+T^2/2$. Meanwhile, $\alpha_0 L/2$ is the cavity intrinsic loss mainly from the radiation and material absorption. For a high Q cavity such as the one used in this thesis ($Q > 10^8$), the intrinsic loss is mall as $\alpha_0 L = 2\pi m/Q_0$ [62]. It is sufficient to approximate that $e^{\frac{\alpha_0 L}{2}} \simeq 1 + \alpha_0 L/2$. Therefore, the governing equation for mode coupling can be further simplified to

$$\frac{da_0}{dt} + \frac{1}{2}(\Gamma_0 + \Gamma_c)a_0 + j\Delta_\omega a_0 = jCb_0. \tag{2.26}$$

Eq. (2.26) describes the relation between the exciting mode b_0 in a coupler and the WGM a_0 in a cavity. The second term in the equation is the loss term, which represents both the intrinsic loss rate of the cavity $\Gamma_0 = \alpha_0 L/\tau_c$ and coupling loss rate to

the fiber taper $\Gamma_c = T^2/\tau_c$. The freqeuency difference of the input laser with regard to the cavity resonance, $\Delta_\omega = \omega - \omega_0$ is called frequency detuning. When $\Delta_\omega > 0$, the laser frequency ω is blue detuned to the cavity resonance. In contrast, when $\Delta_\omega < 0$ the laser is red detuned.

By multiplying the Eq. (2.26) with a_0^* and the complex conjugate of the equation with a_0, add them, we obtain

$$a_0 \frac{da_0^*}{dt} + a_0^* \frac{da_0}{dt} + a_0^* a_0 Re\{\delta_0 + \delta_c\} = 2Re\{jCb_0 a_0^*\}. \tag{2.27}$$

This reveals the simple transfer relation from the optical power in the fiber coupler P_f to that in the WGM cavity P_w.

$$\frac{dP_w}{dt} + \Gamma_t P_w = \gamma P_f, \tag{2.28}$$

where $\Gamma_t = \Gamma_0 + \Gamma_c$ is the total decay rate including the contributions from both the coupling and intrinsic loss, and $\gamma = 2Re\{jCa_0^*/b_0^*\}$ is the power transfer rate determined by both the coupling rate and how close the coupler mode is to the cavity mode.

It is worth mentioning that when the pump laser is turned off, $P_f = 0$, Eq. 2.28 gives the cavity power decay rate at $\Gamma_t = -dP_w/(P_w dt)$. According to the definition of the Q factor, we have

$$\frac{1}{Q_{total}} = \frac{\Gamma_{mat} + \Gamma_{rad} + \Gamma_c}{\omega_0} = \frac{1}{Q_{mat}} + \frac{1}{Q_{rad}} + \frac{1}{Q_c}, \tag{2.29}$$

which confirms the relation of cavity Q factors. Besides, the first term, which is the material absorption loss, provides a way to estimate the $Q_{mat} = \omega_0/\Gamma_{mat} = 2\pi n_e/(\alpha_{mat}\lambda_0)$.

2.5 Transmission spectrum

Under the steady state condition, i.e. $da_0/dt = 0$, Eq. (2.26) becomes

$$\frac{1}{2}\Gamma_t a_0 + j\Delta_\omega a_0 = jCb_0. \tag{2.30}$$

It indicates that the mode intensity in the cavity has a dependence not only on the pump laser power but also on the laser-cavity detuning Δ_ω. In order to derive the

output transmission power, the mode amplitude received at the output of the fiber coupler is

$$b_0' = jTa_0 + Rb_0 \approx b_0\left(1 - \frac{2\Gamma_c}{\Gamma_t + 2j\Delta_\omega}\right). \tag{2.31}$$

Similar to the Eq. 2.22, the mode at the coupler output is a composite of the reflection of the coupler and the coupling from the cavity. Based on Eq. (2.31), we can derive the mathematical expression of the normalized transmission spectrum near the cavity resonance as,

$$\left|\frac{b_0'}{b_0}\right|^2 = 1 - \frac{4\Gamma_c\Gamma_0}{(\Gamma_c+\Gamma_0)^2 + 4\Delta_\omega^2} = 1 - \frac{4Q_cQ_0}{(Q_c+Q_0)^2 + (2Q_cQ_0)^2\left(\frac{\omega-\omega_0}{\omega_0}\right)^2}. \tag{2.32}$$

This expression shows the output transmission spectrum of a WGM cavity as a function of the input laser frequency ω, whose shape depends on both the cavity intrinsic loss Q_0 and the coupling Q_c. Clearly, this spectrum has a Lorentzian-shaped dip centred at the cavity resonance ω_0, which offers a way to identify the resonance wavelength experimentally. Besides, at the half maximum of the resonance dip where

$$(Q_c+Q_0)^2 = (2Q_cQ_0)^2\left(\frac{\omega-\omega_0}{\omega_0}\right)^2, \tag{2.33}$$

the laser frequency at both red and blue detuning points are

$$\omega_\pm = \omega_0 \pm \frac{1}{2}\frac{\omega_0}{Q_t}. \tag{2.34}$$

Therefore, the full width at half maximum (FWHM) of the transmission Lorentz dip is determined by the loaded caivty quality factor Q_t and its resonance $\Delta\omega$ that

$$\Delta\omega = \omega_+ - \omega_- = \frac{\omega_0}{Q_t}. \tag{2.35}$$

As shown in Fig. 2.2, the $\Delta\lambda$ or $\Delta\omega$ is the cavity resonance linewidth. Measuring the linewidth of the resonance dip is one of experimental methods to characterize the cavity quality factor.

Further, Eq. (2.32) can be simplified by introducing a normalized coupling parameter $K = Q_0/Q_c$,

$$\left|\frac{b_0'}{b_0}\right|^2 = 1 - \frac{4K}{(K+1)^2(1+\bar{\Delta}_\omega^2)}, \tag{2.36}$$

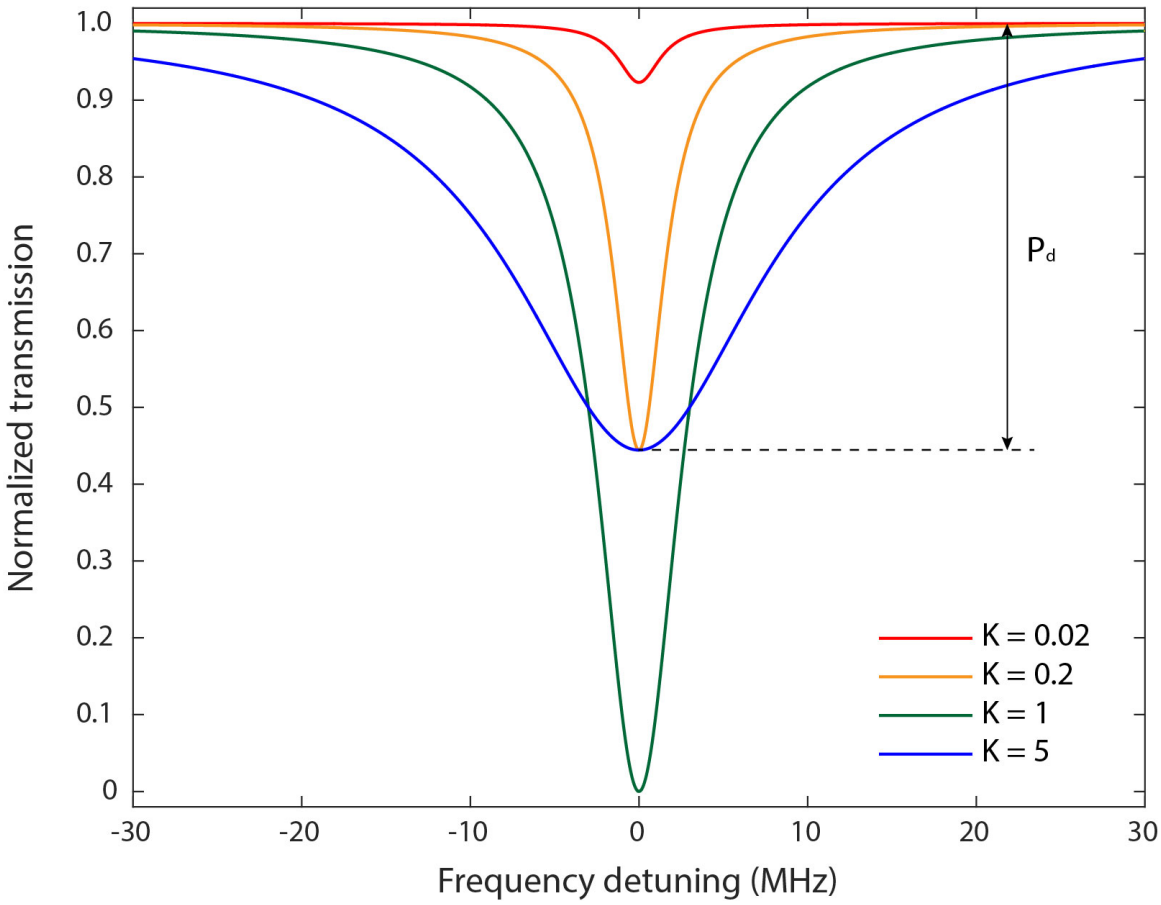

Figure 2.7: Normalized transmission spectra for different couplings conditions.

where $\bar{\Delta}_\omega = 2\Delta_\omega/\Delta\omega$ is the normalized laser-cavity detuning. According to Eq. 2.36, we plot the normalized transmission spectra as a function of the frequency detuning around a resonance mode in Fig. 2.7. For the purpose of illustration, we simulate the transmission spectra with an ultrahigh Q ($Q_0 = 1.0 \times 10^8$) WGM cavity that has a resonance wavelength $\lambda_0 = 1.0$ μm. As the laser frequency scanning from the red detuning side ($\omega < \omega_0$) to the blue detuning ($\omega > \omega_0$) across the cavity resonance, the transmission spectra show the Lorentz dips with different linewidths and depths for different coupling conditions ($K = 0.02$, 0.2, 1, 5). As shown, linewidths at different coupling conditions are different, indicating that the total quality factor Q_t varies with the coupling Q_c, even though the intrinsic quality factor Q_0 remains constant. From Eq. 2.21, the Q_0 can be derived through experimental measurements.

In addition, the difference between the transmitted power at a fixed detuning and the off-resonance transmission is defined as the dropped power (P_d). It characterizes the optical power transfer from a coupler to a cavity. Generally, little power is coupled into a cavity when the laser is far off the resonance. When the input laser is tuning toward the cavity resonance, the power dropped into the cavity increases and the transmission falls into the dark Lorentz peak. For any coupling condition, the dropped power reaches the maximum value at the zero detuning ($\omega = \omega_0$) as shown in Fig. 2.7, corresponding to the minimum on the transmission spectrum. Both of the dropped power and output transmission recovers when the laser detuning increases after crossing the resonance point.

Also shown in Fig. 2.7 is that the transmission at the resonance when $K = 1$. This indicates that the input optical power is fully compensates the cavity loss. Therefore it is called the critical coupling where $Q_\mathrm{c} = Q_0 = 2Q_\mathrm{t}$. Once on-resonance, the cavity mode gains the highest power by a given pump source when it is critically coupled. Note that not all of the coupling methods can achieve the critical coupling, as it requires a matching between the cavity mode and the input field. The high coupling efficiency is the very reason that we choose the tapered optical fiber as the coupler for the experiments. A higher intracavity power is always preferable to the investigation of many interesting nonlinear optical phenomena.

If the tapered fiber is not critically coupled, the cavity transmission spectrum is always above zero even at resonance. In particular, the coupling regime where $Q_0 > Q_\mathrm{c}$ is called under coupling while $Q_0 < Q_\mathrm{c}$ over coupling. Here, under coupling is a weak coupling condition where the coupling rate can not match the cavity decay. The red and orange spectra in Fig. 2.7 are both from the under coupling condition

($K < 1$). The smaller linewidth of the red cure ($K = 0.02$) compared with that of the orange ($K = 0.2$) is due to the larger Q_c for a weaker coupling (smaller K). In practice, $Q_t \approx Q_0$ at a very under coupled condition. On the other hand, the over coupling has a strong coupling rate that $K > 1$. Although it may has the same transmission as the under coupling at the resonance, its resonance linewidth is always larger that from the critical coupling. In this case, the Q_c makes more contribution than the Q_0 to degrade the Q_t.

2.6 Intracavity buildup power and nonlinear effects

Considering the small mode volume and high Q, a WGM cavity is able to accumulate a strong optical power density by confining the photons in space and time. This intracavity power can be estimated from the Eq. (2.30) from which we obtain

$$\frac{P_w}{P_f} = \left| \frac{1}{\frac{\Gamma_t}{2} + j\Delta_\omega} \frac{jT}{R\tau_c} e^{\frac{\alpha_0 L}{2}} \right|^2 . \tag{2.37}$$

The above expression gives the optical power circulating within a cavity that is normalized to the pump power. The WGM cavity functions as an optical amplifier whose magnification depends on the quality factor Q and the frequency detuning Δ_ω. Using the approximations $e^{\frac{\alpha_0 L}{2}} \approx 1 + \frac{\alpha_0 L}{2} \approx 1$ and $1/R \approx 1 + T^2/2 \approx 1$, the ratio between the intra-cavity power and taper input power follows

$$\frac{P_w}{P_f} = \frac{1}{(\omega_0/2Q_t)^2 + \Delta_\omega^2} \frac{\omega_0 c}{n_e L Q_c}, \tag{2.38}$$

where $Q_t = \omega_0 \tau = \omega_0/\Gamma_t$ and $Q_c = \omega_0/\Gamma_c = \omega_0/(T^2/\tau_c)$. The τ is the photon life time for a loaded cavity from Eq. 2.20, while $\tau_c = n_e L/c$ is the photon round trip time in the cavity.

For a fixed input, the cavity can only gain the maximum power of the resonance mode under the critical coupling that $Q_c = Q_0 = 2Q_t$. On resonance $\omega = \omega_0$, the maximum cavity buildup power is

$$P_{w,Max} = \frac{Q_0}{2\pi m_r} P_f, \tag{2.39}$$

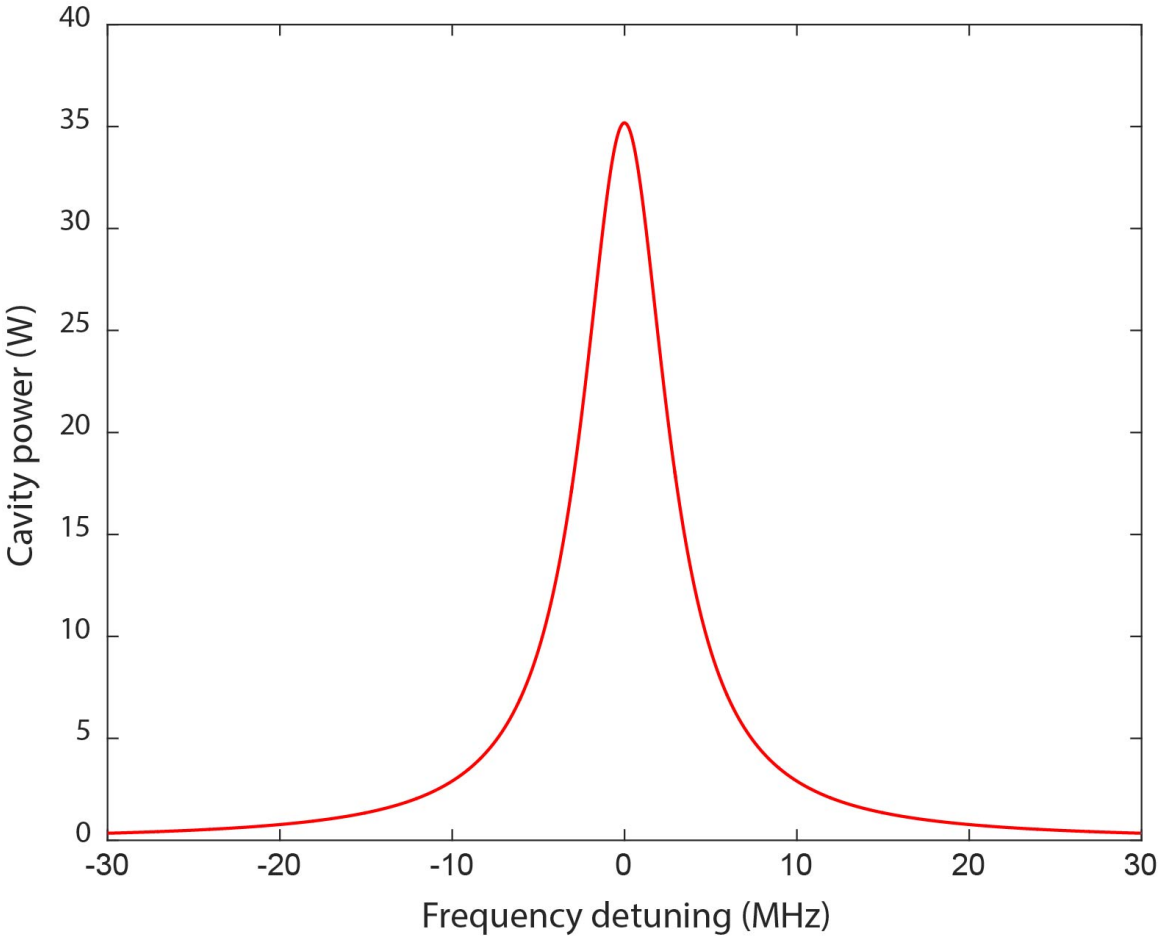

Figure 2.8: Intra-cavity power as a function of the laser-cavity detuning by assuming the input power is 1 mW.

At the critical coupling, we plot the buildup power spectrum according to Eq. 2.38 in Fig. 2.8 for a ultrahigh Q ($Q_0 = 1.0 \times 10^8$) silica microcavity with a 50 μm radius pumped by a 1 mW laser source operating around 1 μm wavelength. The spectrum indicates the maximum cavity power at the resonance exceed 30 W, which is $30,000$ times larger than the input. Additionally, an effective mode area as small as 2.2×10^{-12} m^2 due to the small mode volume of the WGM, results in a maximum mode intensity as high as 1.5×10^{13} W/m^2. Note from Eq. 2.38 that the amplification can be further increased by the reduction of the cavity size, before the radiation loss dominating the cavity intrinsic loss Q_0. Such a considerable power amplification provides a highly efficient platform for the study of nonlinear optics that only occurs above certain threshold power. Provided by a regular laser source of a few mili-watts, the WGM microcavity platform has successfully demonstrated a lot of nonlinear effects, such as the Raman lasing [63, 64, 65], rare earth doped microlasers [61, 41], optomechanics [66, 67], and the thermo-optic effects [68, 69, 70].

The material loss Q_{mat} reveals that the dielectric material of a WGM cavity dissipates a minute amount of optical energy through the absorption. A portion of the dissipated energy is converted to the heat and increases the cavity temperature. For low Q devices, the generated heat is small in amount and dissipates quickly into the surrounding medium. Therefore, the change of the cavity temperature is negligible. However, for an ultra-high Q cavity, a small input power may build up sufficient intracavity intensity that can generate a substantial amount of heat within the small cavity volume. Meanwhile, the microcavity has a low thermal conductivity due the limited surface area, which makes the cavity temperature increment more significant. As a result, some temperature dependent effects can occur.

For example, silica is a common material used widely in optics and cavities. Its refractive index n increases with the temperature resulting a positive temperature dependence of refractive index $\partial n/\partial T = 1.3 \times 10^{-5}\ K^{-1}$ [71]. Note that, its thermal expansion coefficient ($< 1.0 \times 10^{-6}\ K^{-1}$ at room temperature) is more than an order of magnitude smaller than $\partial n/\partial T$, its influence of resonance wavelength change can be neglected [72]. As a result, the Lorentz transmission dip becomes an asymmetric transmission spectrum as shown in Fig. 2.9. In the bottom plot, the blue peak is the pump laser mode which has a much narrower linewidth compared to the cavity mode without thermal broadening represented by the red trace. When the laser is scanning across the cavity resonance from a shorter wavelength, the cavity power is accumulating. Therefore, one can see a red shift of the cold cavity resonance

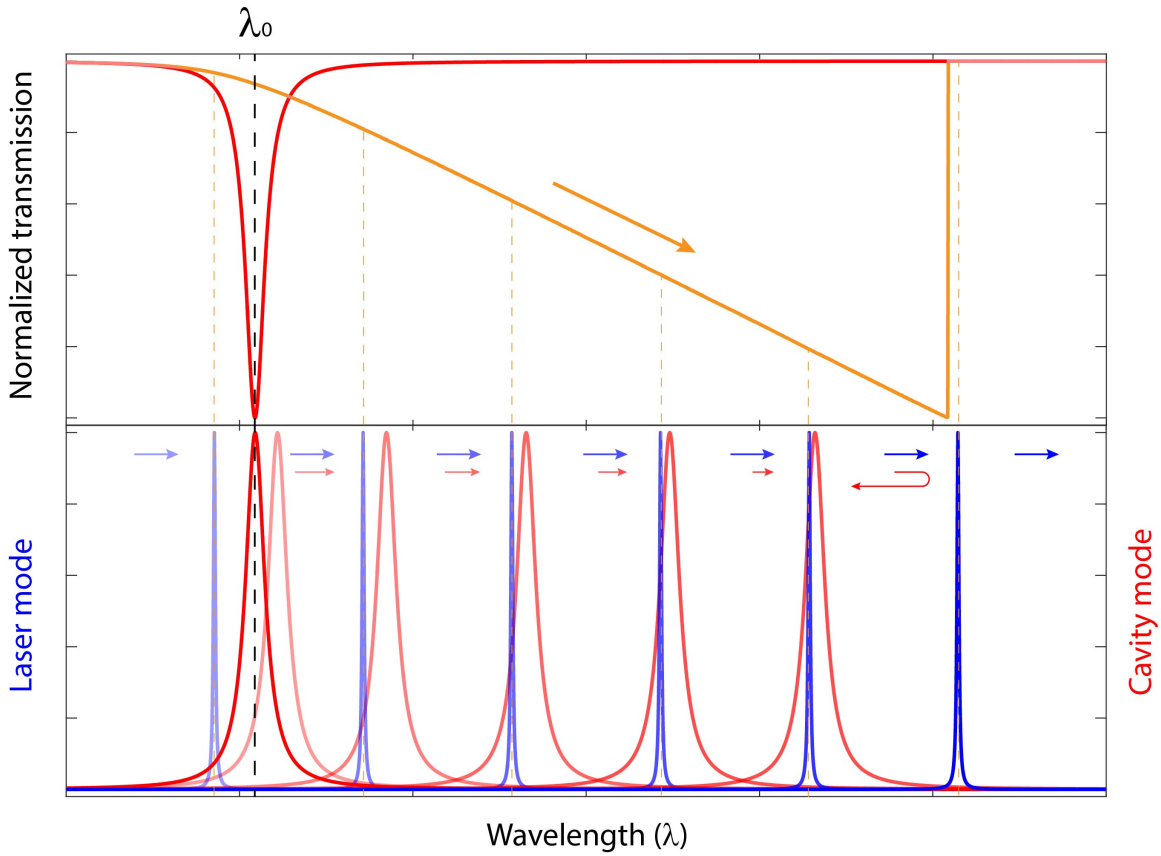

Figure 2.9: Dynamical thermo-optic effects of a cavity. Bottom: The input laser (blue) scans across the cavity resonance (red). Top: The broadened transmission spectrum from the thermal effects.

wavelength λ_0, but the relative detuning between the laser λ and the heated cavity λ_0' decreases. As the laser keeps scanning toward the longer wavelength, the hot cavity resonance increases while accumulating the intracavity power. During this process, the laser is approaching the hot cavity resonance, and catching the resonance at a wavelength where the cavity power reaches the maximum. Therefore, the transmission spectrum displays a thermal broadening effect. When the laser frequency crosses the maximum cavity resonance into the red detuning regime and the cavity power starts to fall quickly. In the phase, as the dropping of cavity power pushes the cavity resonance further away from the laser causing the cavity to dump more power, the cavity resonance drops back to the wavelength of the cold cavity λ_0 in a short time once the laser passed the resonance, yielding a thermal squeezing effect.

This process is observable in the cavity transmission spectrum measured from experiments as illustrated in the top plot of Fig. 2.9. The red curve is the typical transmission of a cold WGM cavity as a function of the wavelength, whose peak position identifies the location of the resonance wavelength λ_0. The orange trace is the shifted transmission spectrum with a laser wavelength up-scan. Upon the up-scan, instead of displaying a Lorentzian shape, the transmission drops linearly while the laser is getting closer to the cavity resonance. Accordingly, each point in the spectrum represents the transmission at a certain laser wavelength for the corresponding heated cavity mode. Once the laser matching the maximum hot cavity resonance, the transmission reaches zero if it is under the critical coupling condition. The next moment, the output transmission recovers immediately as a sharp step on the spectrum. As at this point, the laser frequency is substantially red detuned to the cold cavity resonance λ_0, the transmission rapidly becomes completely off resonance when the hot cavity resonance drops back just after the crossing point. As illustrated by the plot, the thermal broadening makes the cavity resonance may span over a wide range beyond hundreds of its linewidth during the up-scan with the exact range critically dependent upon both the cavity Q and pump laser power for a given cavity [73].

At the wavelength down-scan regime, where the laser scans across the resonance from a longer wavelength to a shorter wavelength, a material with positive $\partial n/\partial T$ always causes the red shift of the cavity resonance. Therefore, the resonance wavelength moves in the opposite direction toward the laser as the laser is approaching the cavity resonance. As a result, the process for the laser matching the resonance becomes even shorter than that without thermal effects. This is the reason that the

Q measured from down-scan is higher than expected. Therefore, low laser power is always favourable to avoid thermal effects in Q measurements.

Although the thermal effect is unfavourable for the Q measurement, it is valuable in other perspectives. In the blue detuning regime where $\omega > \omega_0$ or $\lambda < \lambda_0$, the laser frequency noise could be suppressed by the thermo-optic effects on the transmission when it is coupled with a high Q caivty [70, 73]. It is above noted that the cavity resonance can follow the change of the pump laser frequency. When the laser frequency has some fluctuations, the thermal effect is able to stabilize the relative laser-cavity detuning.

The thermo-optic effect is one of the many interesting nonlinear phenomena that depends the high cavity buildup power. The nonlinear optics is not exclusionary for the WGM cavities, but the high Q factor and small mode volume of the WGM cavity make it a platform more preferable for the study of nonlinear optics. Besides, it is an efficient way to achieve the required high energy density through the WGM cavity with a given pump source.

Chapter 3

Cavity Reactive Sensing

Based on the unique properties, researchers have explored a great number of applications with the WGM cavity that has high optical quality factor [2, 7]. One of the most intriguing examples is the application in nano-detection and biosensing, which offers one label-free sensing technique with an outstanding resolution by utilizing the narrowed cavity resonance linewidth[74, 75, 76, 77].

It is the dispersive nature of the WGM that causes the resonance shift when the optical field is interacting with surrounding media. The reactive sensing concept was first introduced in 1995 by Prof. Arnold and Griffell, where the sensing of nanoparticles by monitoring the microcavity resonance wavelength shift was envisioned [8]. In 2008, the concept was experimentally demonstrated, where a single Influenza A virus was detected at a signal-to-noise ratio of 3 [12]. This sensing technique was further improved with the help of a reference interferometer to suppress the probe laser jitter noise, where a polystyrene nanobead as small as 12.5-nm-radius was detected [11].

3.1 Sensing principle

As mentioned previously, light launched into a WGM cavity can form a resonance. Once on resonance, the optical path length equals to an integer number of the cavity resonance wavelength (λ_0). When a particle attaches on the cavity surface near the equator, it will introduce a change of the local refractive index that is dependent on the difference of the indexes of the attached particle and the cavity surrounding media. The evanescent part of the cavity field can detect such a variation, leading to a change of the optical path length accordingly. As a result, this will generate

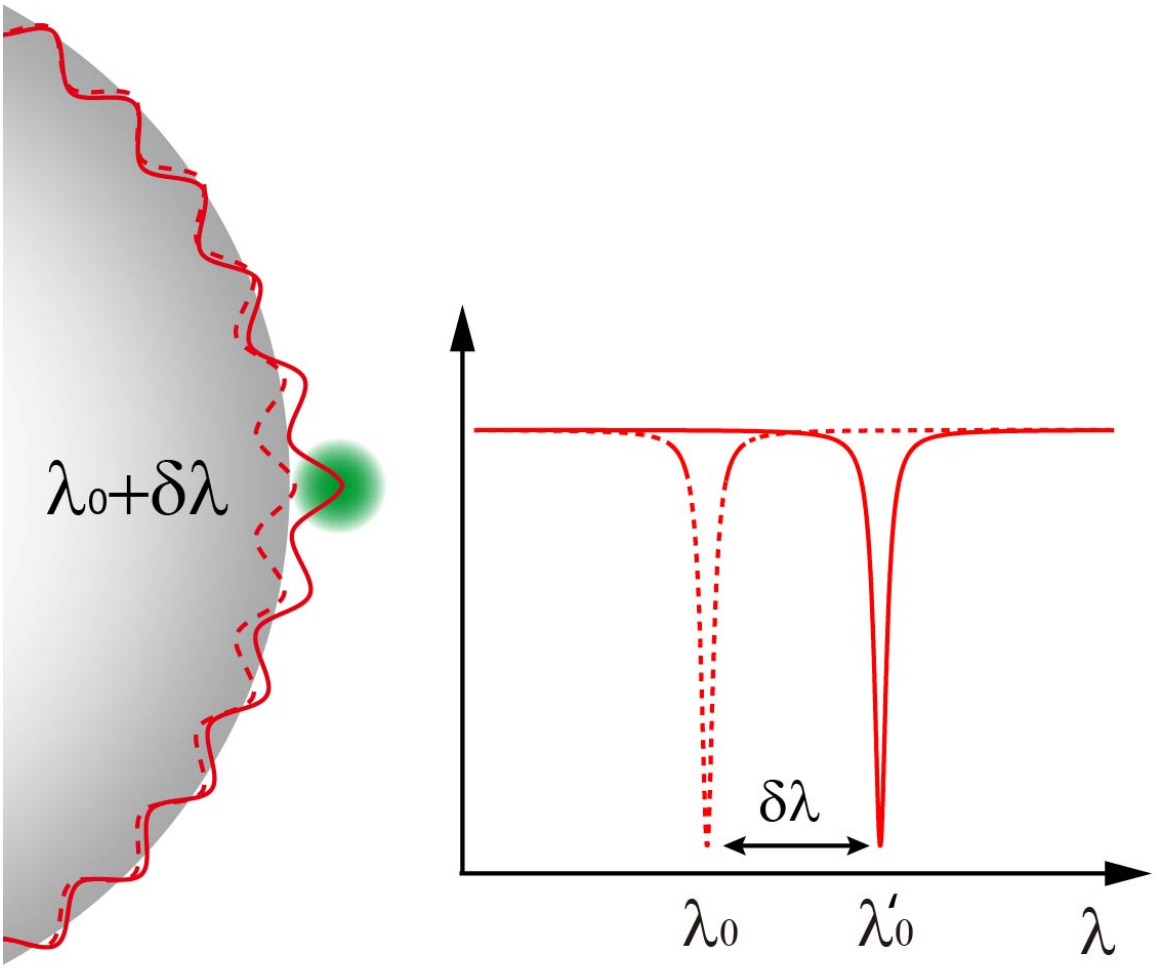

Figure 3.1: Schematic plot of the reactive sensing. The particle adsorbed on the cavity surface induces a change of the optical path length and leads to a shift of the cavity resonance wavelength.

a shift of the cavity resonance wavelength ($\delta\lambda$) for each binding or unbinding event as illustrated in Fig. 3.1. Therefore, the adsorbed particles on the cavity surface are detectable by motoring the steps of the cavity resonance.

One can use one of the Helmhöltz equations (Eq. 2.10) to describe the field in a WGM cavity as following,

$$\nabla^2\mathbf{E} + \frac{1}{c^2}\epsilon_{\mathrm{r}}\omega_0^2\mathbf{E} = 0, \tag{3.1}$$

where c is the speed of light in free space, $\epsilon_{\mathrm{r}} = n^2$ the relative permittivity, and ω_0 the cavity resonance angular frequency before particle binding.

When the nano-particle with a volume V_{p} is attached to the cavity, it changes the index profile locally with its excess relative permittivity $\epsilon_{\mathrm{p}} = \epsilon_{\mathrm{r}} + \delta\epsilon_{\mathrm{r}}$ from the environment. Considering that the nanoparticle is orders of magnitude smaller than the microcavity, one may solve the problem with the help of the perturbation theory [45]

$$\nabla^2(\mathbf{E} + \delta\mathbf{E}) + \frac{1}{c^2}(\epsilon_{\mathrm{r}} + \delta\epsilon_{\mathrm{r}})(\omega_0 + \delta\omega)^2(\mathbf{E} + \delta\mathbf{E}) = 0. \tag{3.2}$$

Here, $\delta\mathbf{E}$ and $\delta\omega$ are the first order perturbation terms that represent the change of the field and the shift of the cavity resonance due to the particle binding respectively. By expanding the perturbation equation and ignoring the high order perturbation terms, it yields

$$\nabla^2\mathbf{E} + \nabla^2\delta\mathbf{E} + \frac{1}{c^2}\epsilon_r\omega_0^2\mathbf{E} + \frac{1}{c^2}\epsilon_{\mathrm{r}}\omega_0^2\delta\mathbf{E} + \frac{1}{c^2}(\omega_0^2\delta\epsilon_{\mathrm{r}} + 2\epsilon_{\mathrm{r}}\omega_0\delta\omega)\mathbf{E} = 0. \tag{3.3}$$

Combining the above equation with the the Helmhöltz equation (Eq. 3.1), we obtain

$$\nabla^2\delta\mathbf{E} + \frac{1}{c^2}\epsilon_{\mathrm{r}}\omega_0^2\delta\mathbf{E} + \frac{1}{c^2}(\omega_0^2\delta\epsilon_{\mathrm{r}} + 2\epsilon_{\mathrm{r}}\omega_0\delta\omega)\mathbf{E} = 0. \tag{3.4}$$

Dot multiply the Eq. 3.4 by $\mathbf{E}^*$ and the complex conjugate of Eq. 3.1 by $\delta\mathbf{E}$, and subtract, we find

$$\mathbf{E}^*\nabla^2\delta\mathbf{E} - \nabla^2\mathbf{E}^*\delta\mathbf{E} + \frac{1}{c^2}(\omega_0^2\delta\epsilon_{\mathrm{r}} + 2\epsilon_{\mathrm{r}}\omega_0\delta\omega)\mathbf{E}^*\mathbf{E} = 0. \tag{3.5}$$

Then, integrate over the whole volume, obtain

$$\int \omega_0\delta\epsilon_{\mathrm{r}} |\mathbf{E}|^2 \, dV + \int 2\epsilon_{\mathrm{r}}\delta\omega \, |\mathbf{E}|^2 \, dV = 0. \tag{3.6}$$

Solving this equation for the shift in cavity resonance,

$$\frac{\delta\lambda}{\lambda_0} = -\frac{\delta\omega}{\omega_0} = \frac{\int \delta\epsilon_{\mathrm{r}}|\mathbf{E}|^2 dV}{2\int \epsilon_{\mathrm{r}}|\mathbf{E}|^2 dV}. \tag{3.7}$$

To estimate the resonance shift, we can ignore the field variation because of the particle adsorption and assume that it is fixed in a plane wave field $\mathbf{E}(\mathbf{r}_{\mathrm{p}})$ localized at the particle position instead of an evanescent field, as long as the particle size is sufficiently smaller than the optical resonance wavelength. Since the $\delta\epsilon_{\mathrm{r}}$ is zero everywhere except the volume inside the particle, the change of the cavity resonance frequency ($\delta\omega$) or the equivalent wavelength shift ($\delta\lambda$) can be approximated as,

$$\delta\lambda = \lambda_0 \frac{\delta\epsilon_{\mathrm{r}}|\mathbf{E}(\mathbf{r}_{\mathrm{p}})|^2 V_{\mathrm{p}}}{2\int \epsilon_{\mathrm{r}}|\mathbf{E}|^2 dV}, \tag{3.8}$$

as shown in Fig. 3.1. For a higher accuracy of the resonance shift calculation, we need to take the particle perturbed evanescent tail into consideration, by replacing the unperturbed field $\mathbf{E}(\mathbf{r})$ with the perturbed field $\mathbf{E}'(\mathbf{r})$ inside the particle, such that [78]

$$\frac{\delta\omega}{\omega_0} = -\frac{\int_{V_{\mathrm{p}}} \delta\epsilon_{\mathrm{r}}\mathbf{E}^*(\mathbf{r})\mathbf{E}'(\mathbf{r})dV}{2\int_V \epsilon_{\mathrm{r}}|\mathbf{E}(\mathbf{r})|^2 dV}. \tag{3.9}$$

For a nanoparticle as small as $\lambda_0/10$, the particle induced resonance shift can be calculated with an improved accuracy for particle sizing, by considering the perturbed field decay across the particle [79].

Eq. 3.8 clearly shows that the resonance wavelength shift ($\delta\lambda$) is proportional to the permittivity difference ($\delta\epsilon_{\mathrm{r}}$) and the particle size (V_{p}). The direction of the resonance shift depends on the sign of $\delta\epsilon_{\mathrm{r}}$. The largest resonance shift of a particle occurs at the location with highest field intensity. For a particle with a larger permittivity than the surrounding media such that $\delta\epsilon_r > 0$, a binding particle can lead to a red shift of the cavity resonance, and a blue resonance shift indicates the unbinding event. It is worth mentioning that the attachment of air bubbles onto the surface of a cavity causes a blue resonance shift, while the red shift represents the unbinding of an air bubble. This is because the smaller permittivity of air compared to that of water makes $\delta\epsilon_{\mathrm{r}} < 0$ and changes the shift direction. At current stage, it is impossible to differentiate the sensing signal difference between the particle binding and the bubble detachment. Therefore, it is important to degas the sample suspension prior to the sensing experiment.

3.2 System configuration

We use the silica microsphere, shown in Fig. 2.1c, as the working device for the sensing experiments, whose diameter is around 100 μm. Without the photo-lithography procedure, the microsphere can be easily fabricated by reflowing the tip of a tapered optical fiber with a CO_2 laser beam. The CO_2 laser has an operating wavelength at 10.6 μm, which is highly absorbable by the silica fiber. The microsphere made with fused silica has a ultrahigh Q above 2.0×10^8.

To couple the light into a WGM cavity, the free space coupling is the easiest approach. However, it is the least efficient method due to the low coupling efficiency compared with the fiber taper coupler, which shows close to 100% coupling efficiency [55, 80]. In our research, we fabricate the tapered fiber coupler on the customized fiber pulling station shown in Fig. 3.2. Two fiber holders are fixed onto the motorized translational stages on each side. Before placing the fiber on to the holders, the polymer coating of the single mode fiber should be removed. The fiber is heated by the hydrogen mini-torch underneath with an optimized position and gas flow rate. The taper transmission loss is monitored with the oscilloscope while it is pulling. Generally, the loss of a good taper will not exceed 10 percent of its transmitted power after pulling while undetectable loss can be achieved. During the pulling process, the core of the single mode fiber gradually vanishes while the multiple cladding modes will be dominant in guiding the light through the tapered fiber section. When this occurs, the optical intensity transmitted through the fiber starts to oscillate due to multimode interference. Continue pulling the fiber to reduce the fiber taper width, one may obtain a tapered fiber that only supports a single cladding mode. Once the transmitted intensity ceases to vary, the taper reaches the single mode condition and the pulling process should be stopped.

When both the cavity and taper coupler are ready, they are assembled on the sensing stage in the configuration shown in Fig. 3.3. The microsphere is placed underneath the taper. The position of the taper is controlled by a nano-positioner with a great accuracy of about 100 nm. For a better sensitivity, the cavity usually stays in the under coupling regime where the resonance linewidth is mainly determined by the intrinsic loss (Q_0).

Finally, by connecting the input of the taper with an external tunable laser and its output to a photodetector to convert the transmitted optical intensity to the electrical signal that can be monitored on the oscilloscope, the workable sensing system based

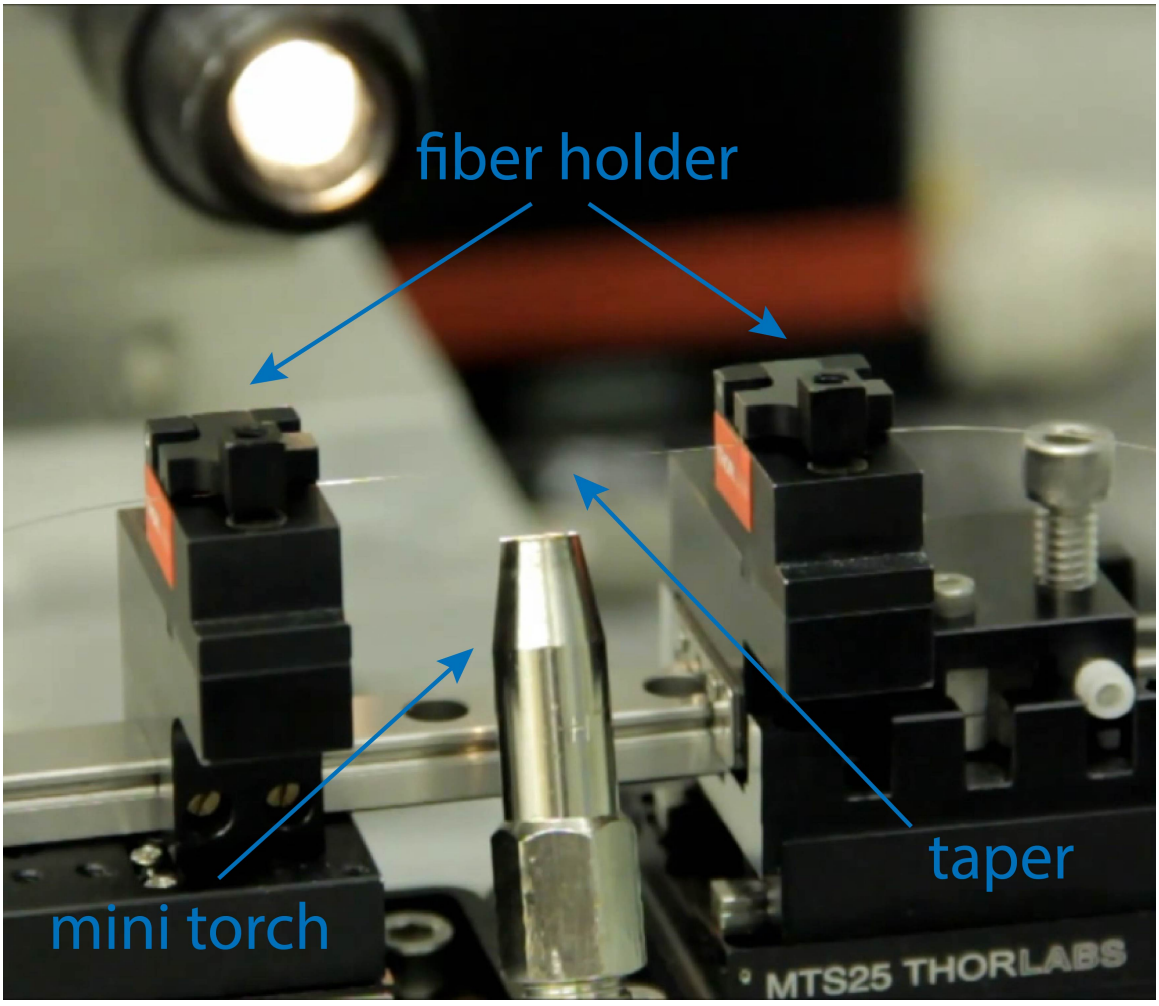

Figure 3.2: The tapered fiber coupler is made by heating and pulling a single mode optical fiber on the customized fiber pulling stage.

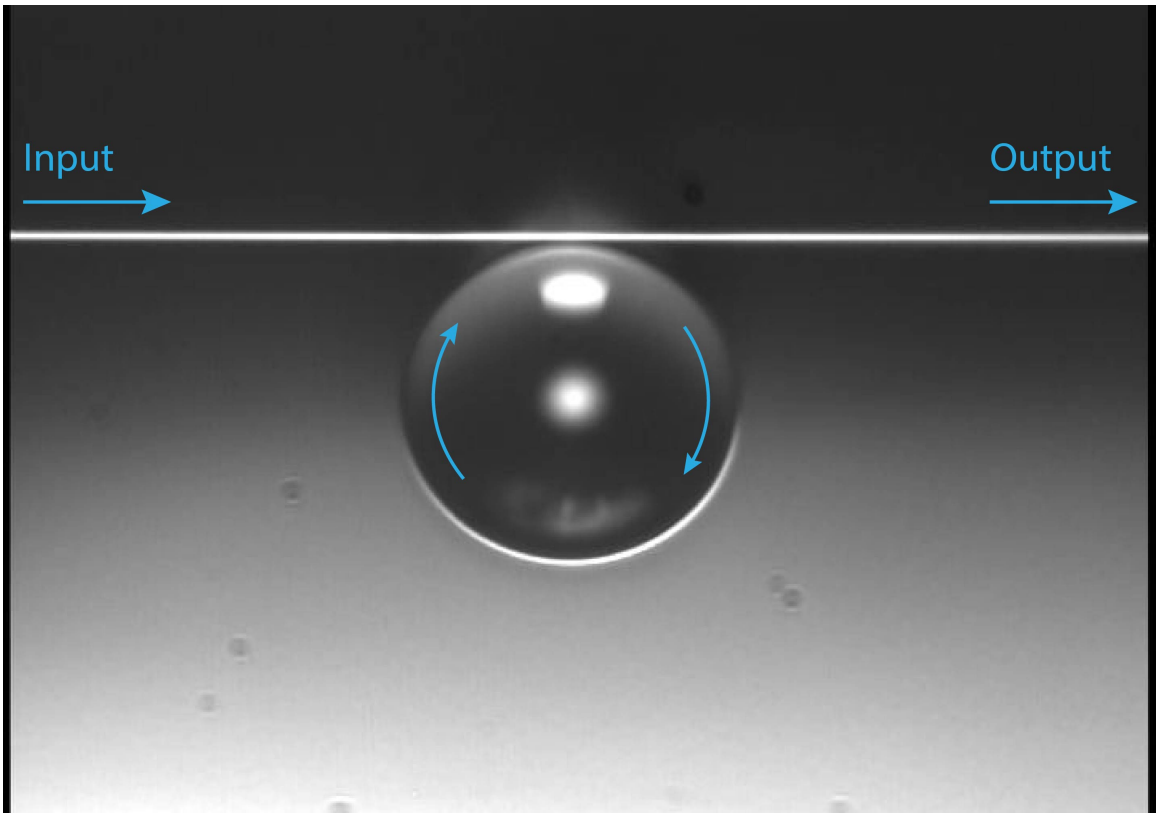

Figure 3.3: The front view of the sensing configuration for a silica microshere coupled with a tapered fiber coupler above it.

on a WGM cavity is complete. In order to detect the biological samples such as virions or protein molecules, which are usually prepared as suspension, the cavity and taper can be immersed into an aqueous environment without the significant degradation to the cavity Q or the taper transmission.

By scanning the probe laser wavelength with a function generator, a couple of resonance dips can be probed. Although every resonance mode can be used for sensing, a cavity mode with a narrower linewidth is always preferred for sensing. It is achieved by the fine tuning of the taper position with regard to the microsphere and the laser polarization.

3.3 Peak resolution

To explore the sensitivity limitation, two factors have to be considered. One is how accurately a cavity resonance wavelength (λ_0) or frequency (ω_0) can be determined. The other is the amount of background noise of the system. The sensitivity is limited collectively between the peak resolution and the system noise level.

The peak resolution is the minimum detectable WGM resonance shift of the cavity. As the cavity resonance is identified by the location of the resonance dark peak, the peak resolution is the minimum value of the difference between two peaks closely placed. According to Rayleigh criterion [54], the peak resolution is proportional to the resonance linewidth that in turn is inversely proportional to the cavity quality factor $\Delta\lambda = \lambda_0/Q$. Therefore, a narrower linewidth from a higher Q cavity is always preferred for a better sensitivity. However, it is impossible to increase the Q factor infinitely. When the cavity Q is pushed close to its theoretical limit, alternative approaches have to be explored for further improvements.

Another important factor that determines the sensing limit is the back ground noise of the system. The manifestation of noise on the spectrogram is the fluctuations of the cavity resonance. When the signal is lower than the noise level (SNR$<$ 1), the resonance shift due to the particle binding is not distinguishable from the fluctuations. For a given signal, the way to improve the signal-noise-ratio (SNR) is to lower the noise level of the system.

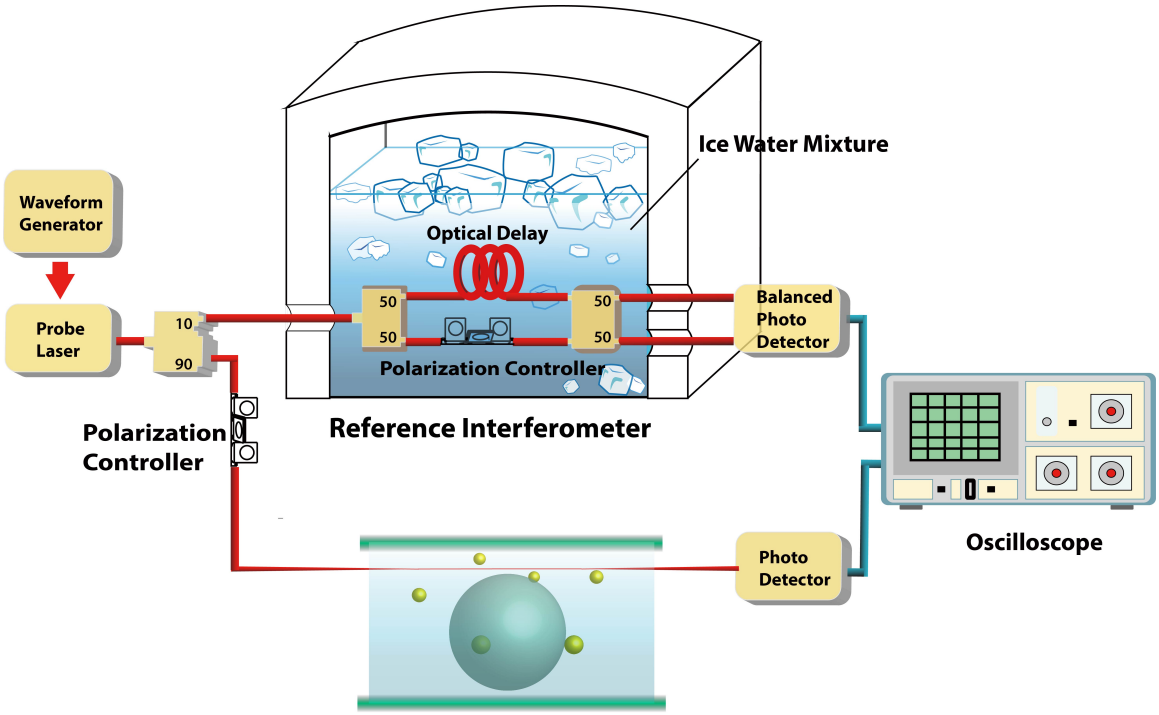

Figure 3.4: The setup for the microspere sensing system with a reference interferometer connected in parallel.

3.4 Reference interferometer

The dominant noise of the current system configuration is the fluctuations in the laser frequency/wavelength, known as laser jitter noise. Such fluctuations lead to the inherent uncertainty in the location of the transmission dip. Using the reference signal from a fiber Mach-Zehnder interferometer (MZI) has been a successful approach to suppress the spectral noise due to the laser jitter [11]. A thermally stabilized fiber MZI is connected in parallel with the WGM sensor in Fig. 3.4. The interferometer is stabilized to avoid any fluctuations as much as possible, by putting the interferometer with the mixture of ice and water in a foam box. There is a certain part of the input laser power coupled into the optical interferometer to produce a reference signal that follows the laser jitter.

Fig. 3.5 shows the transmission spectrum from the WGM cavity (top) and the interferometer connected in parallel (bottom). There are two splitting cavity modes showing on the spectrum arising from the interaction between the forward propagating whispering gallery mode and the backscattered mode [81]. The relative position of the splitting modes is not affected by the laser jitter noise. Therefore, it provides an additional means to the nanoparticle detection with a good sensitivity [15, 82]. The sinusoidal curve is the transmission of the optical interferometer captured in the same time as the cavity spectrum. Since the laser frequency is modulated linearly through the function generator, each period of the sinusoidal curve corresponds to the sweep of optical frequency by one free spectral range (FSR) of the fiber interferometer, which is 36.6 MHz in our case. After conducting a least square fit to the double Lorentzian function and the sinusoidal curve, the optical frequency and linewidth can be measured by comparing the transmission spectra of the cavity and the reference interferometer. Therefore, the quality factors measured from the spectrum are 2.1×10^8 for the resonance to the left and 3.8×10^8 for the resonance to the right, when the cavity is immersed in Dulbecco's Phosphate-Buffered Saline (DPBS).

3.5 In-line interferometer

The previous sensing scheme improves the sensitivity with the help of a reference signal indicating laser noise, however, it requires a split-off of the probe laser to the interferometer. This limits its application to power sensitive measurement where the maximum injection of probe laser power into the cavity is required. To circumvent

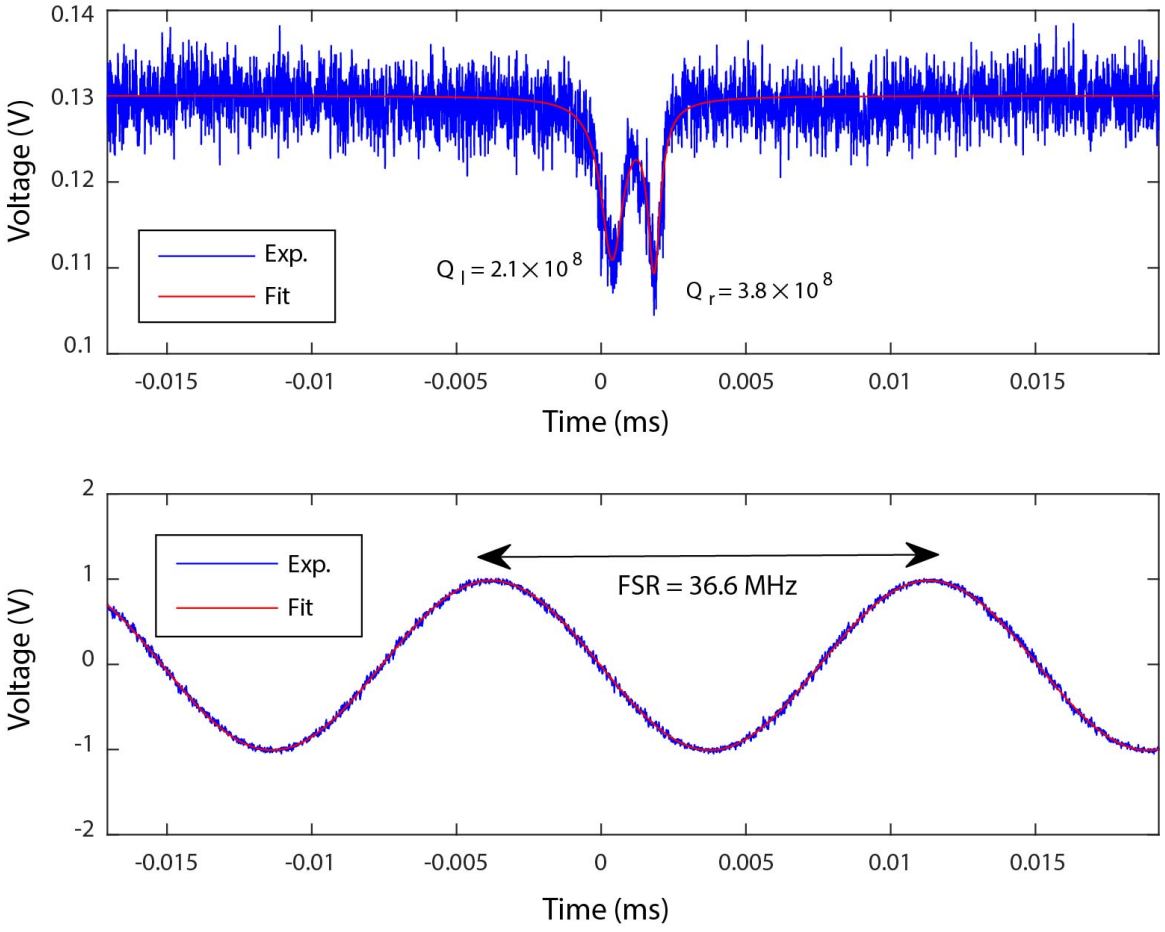

Figure 3.5: The cavity transmission spectrum. Top: The cavity resonance shows quality factors of 2.1×10^8 for the resonance to the left and 3.8×10^8 for the resonance to the right; Bottom: Interferometer signal used to determine the resonance location and linewidth.

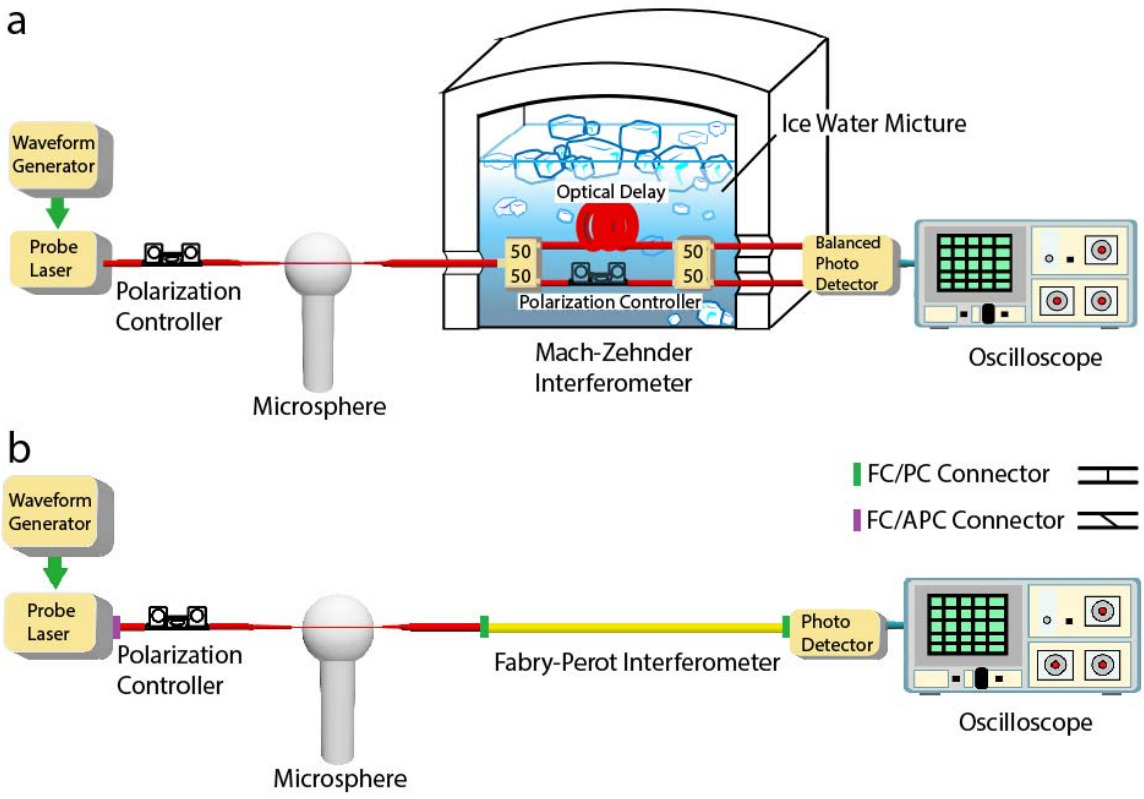

Figure 3.6: Schematic plot of WGM sensing systems with in-line interferometers. (a) WGM sensor with a Mach-Zehnder interferometer in serial (b) WGM sensor with a Fabry-Pérot interferometer in serial

the issue, we connect the interferometer in serial to the WGM sensor instead.

As shown in Fig. 3.6(a), a balanced amplified photodetector (PD) converts the optical output signal of the interferometer to electrical and sends to the oscilloscope. The employment of a balanced photodetector is favourable for Mach-Zehnder interferometry to cancel the excessive intensity noise. Next, to further simplify the experimental configuration and data processing, we replace the MZI with a Fabry-Pérot interferometer (FPI) in Fig. 3.6(b). Here, the FPI is simply a fiber patch cord with (FC/PC) connectors on both ends. The connectors are not completely tightened so that a small portion of the light may back reflect between the connectors to form a FP type interferometer. It is also worth noting that in a typical microcavity sensing system, an inherent FP cavity may already exist due to, eg. the minute back-reflection from poorly cleaned fiber connectors, which usually introduce sinusoidal ripples on the transmission spectrum. Therefore, one may use the following approach to improve the sensing resolution without introducing any new components in the setup.

In Fig. 3.7, the transmission spectrum is obtained from sensing experiments with the in-line FPI, which has a free spectral range of 49.8 MHz. Therefore, with the help of a least square fit (red trace), the probe laser frequency scanning rate is estimated to be 2×10^6 MHz/s. Consequently, the cavity Q is about 2.1×10^8 in DPBS. We further collected $8,192$ transmission traces seamlessly from the oscilloscope in each time section for the sensing experiments.

The experimental data after the post-processing is plotted in Fig. 3.8, which is the variation of the cavity resonance wavelength as a function of time. The blue trace is obtained from the reference signal for the cavity resonance drifting, while the grey one is tracked through the conventional method that is estimating the cavity resonance wavelength with the probe laser frequency modulation voltage at the dip location. As shown in the figure, both traces show a red drift of the cavity resonance wavelength, indicating a slow decrease of cavity resonance frequency or equivalently increase of resonance wavelength. This trend is anticipated due to the slow drifting of both the ambient temperature and the gap between the fiber taper and the cavity. Nevertheless, the resonance wavelength experiences a drift of less than 10 fm over 80 seconds as shown by the blue trace extracted from the spectrogram. As a comparison, the conventional method yields a measurement uncertainty of around 17 fm whilst our FPI reduced the uncertainty by more than an order of magnitude to around 1 fm. In addition, the conventional method indicates a larger cavity resonance wavelength drift

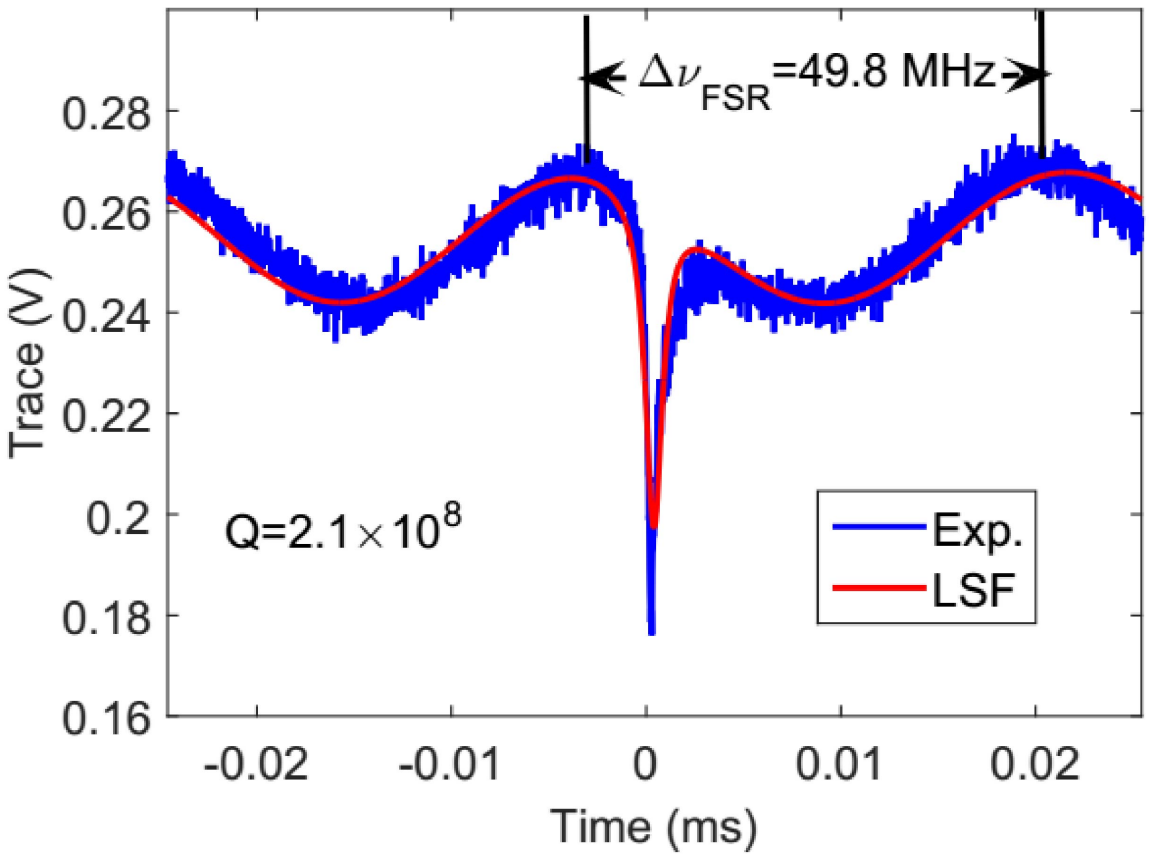

Figure 3.7: The transmission spectrum of WGM with a Fabry-Pérot interferometer in serial

compared to the FPI measurement result. That is due to the fact that wavelength wander occurs in probe lasers. Consequently, the conventional method produced a systematic error in estimating the cavity resonance wavelength shift while such error does not exist in interferometry systems.

Finally, Fig. 3.8 indicates that our sensing setup is highly stable for the detection of resonance wavelength steps produced by nanoparticle binding events. With this scheme, we have demonstated the detection of single polystyrene beads with a radius as small as 25 nm at a signal-to-noise ratio of around 3 [83]. The reference interferometry technique is shown to be a versatile sensitivity enhancing element in nanodetection experiments. The serial connected interferometer approach was shown to be of benefit. The mean sensitivity of this experiment was 1 fm, showing a great improvement over the conventional sensitivity.

3.6 Summary

In summary, we have described the principles of the optical reactive sensing based on the WGM cavity. A reference interferometer can be employed to increase the signal-to-noise ratio by suppressing the laser jitter noise, thereby contributes an improvement to the sensitivity. Using an in-line Fabry-Pérot interferometer, similar performance enhancement can be achieved with much simpler implementation.

The current sensitivity of the cavity reactive sensing is insufficient to detect single protein molecules. Besides, according to the perturbation theory, enhancing the local field near the particle while keeping the rest of the field unchanged can increase the resonance shift. This has been demonstrated with the implementation of metallic nanoantenna on the cavity surface [16]. The localized surface plasma effect of the metallic antenna is able to dramatically increase the optical intensity with a small volume near the antenna, but with an acceptable degrading of the Q factor. However, it requires some additional challenging effort to fabricate a dielectric cavity combined with a metallic antenna in nanometer scale. Meanwhile, the effective sensing area has been dramatically reduced from hundreds of square micrometers to hundreds of square nanometers. Next, we will provide an alternative approach to further push the limit of the WGM cavity sensing.

The in-line interferometer work has been published in Biosensors Journal [83], which is in collaboration with the author's colleagues. Steven Herchak studied and explored the theoretical derivation, experimental measurements, and the data anal-

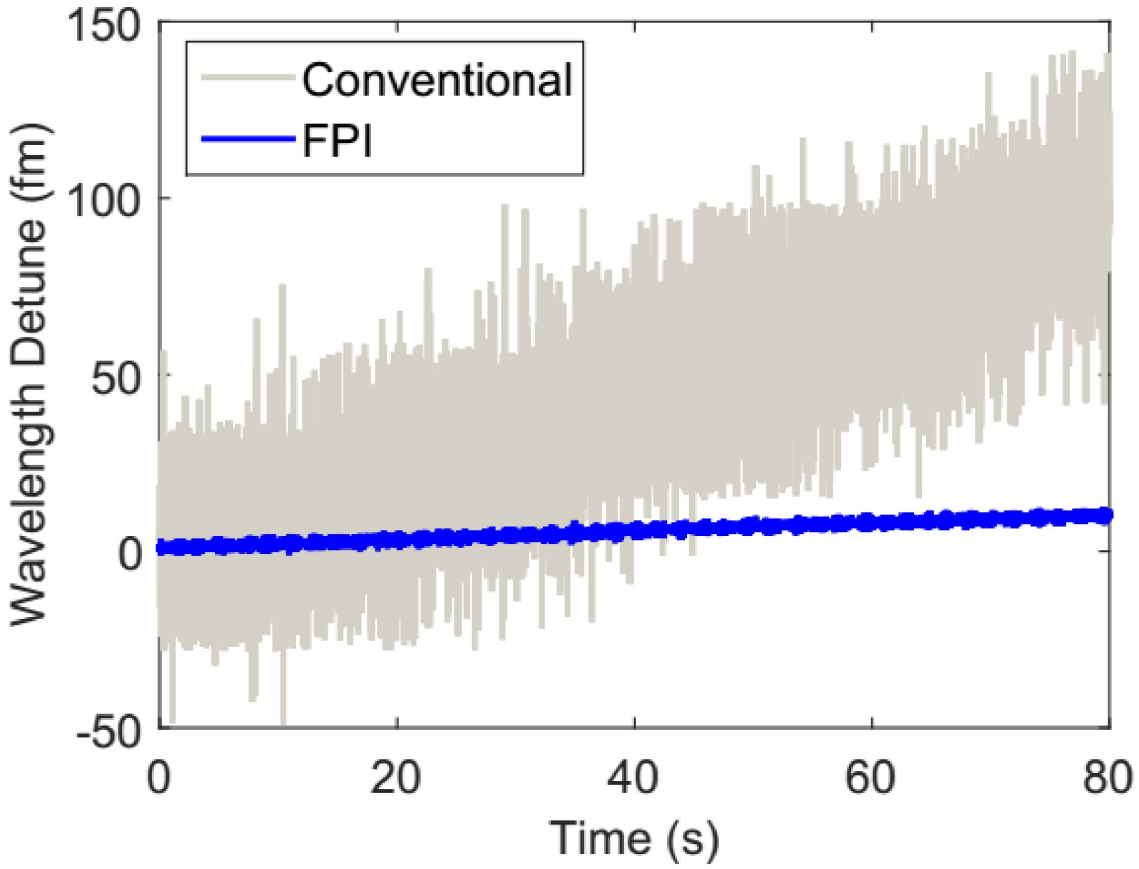

Figure 3.8: The comparison of transmission fluctuations between the FPI and the conventional configuration.

ysis [84]. The author fabricated the device, employed the stability characterization and nanoparticle sensing with the Fabry-Pérot interferometer. The supervisor (T.L.) conceived the idea, designed the experiment and participated the data analysis. Prof. W.S. Lu contributed the data processing with his expertises in signal processing.

Chapter 4

Optomechanical Oscillation

In the previous discussion, utilizing the narrow optical resonance linewidth of the high Q WGM for biosensing is one of the most interesting applications for optical mcirocavities with great promise, which has been in research for years [10, 11, 17, 77, 85, 86, 87]. Meanwhile, another important property of a high Q microcavity that hasn't been fully investigated for the sensing in liquid application is the cavity optomechanical oscillation (OMO), which is the regenerative mechanical motion of a cavity caused by the radiation pressure of the condensed optical field inside.

4.1 Radiation pressure

It is well known that the rest mass of a photon is zero but the photon does have energy and momentum that are nonzero. For a photon with a frequency $\omega = 2\pi\nu$, its corresponding energy is $E = h\nu$ and momentum is $\mathbf{p} = h\nu/c\widehat{\mathbf{k}}$, where h is the Planck constant and $\widehat{\mathbf{k}}$ is the unit wave vector indicating the propagating direction. Although negligible in most scenarios, the momentum change of a single photon does exert a force on the object. The optical force plays a crucial role where the light has a significantly high photon density, such as the resonance mode inside a low loss optical cavity [88, 89].

For the illustration, Fig. 4.1 shows the dynamical interaction of a Fabry-Pérot (FP) cavity mechanical eigenmodes and its optical resonance modes through the optical force. The cavity is pumped with a stable laser at a certain wavelength. When the photons are propagating inside a cavity of length L, they are reflected multiple times by the two end mirrors to form the resonance mode if their wavelength satisfies

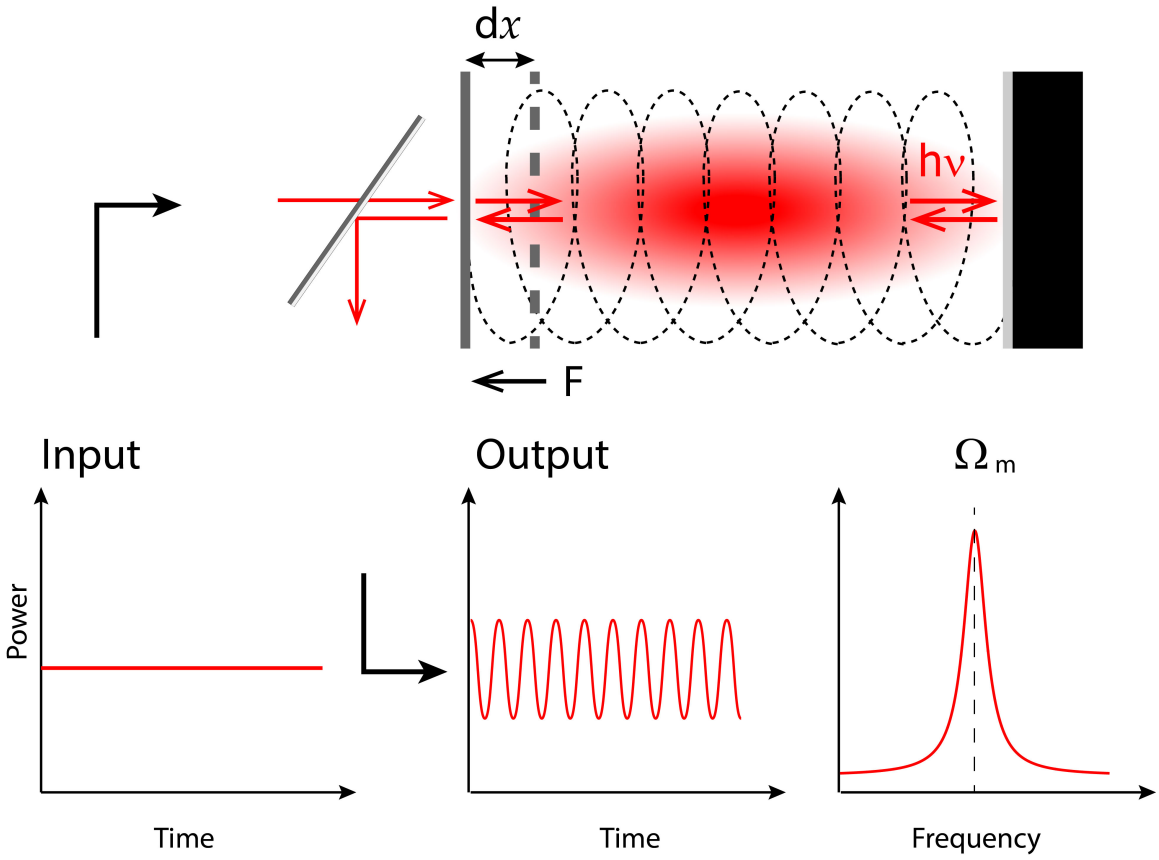

Figure 4.1: Schematic plot showing the radiation pressure in an optical resonator. The radiation pressure causes the movement of the cavity boundary, therefore the output is modulated by the cavity osculation frequency Ω_{m} with a constant input power.

$\lambda_0 = 2L/m$. Here, m is an integer longitudinal mode number for FP cavity. At every reflection, the momentum change for each photon is approximately $\Delta p = 2|\mathbf{p}| = 2h\nu/c$. Being hit continuously by the propagating photons, the cavity wall sustains an optical force from the resonance mode pointing to the outward. The amplitude of the optical force is determined by the number of reflected photons per unit time that is the circulating power P_c within the cavity. Therefore, the optical force depends on the intracavity power according to $F = 2P_{\mathrm{c}}/c$ for the FP cavity whereas $F = 2\pi n_{\mathrm{e}} P_{\mathrm{c}}/c$ for the WGM cavity. Moreover, recall the power buildup capability and small mode volume of the high Q WGM microcavity, the applied pressure from the optical force is sufficient to cause a deformation of the cavity structure. For instance, an ultrahigh Q ($Q > 10^8$) WGM microcavity generates a radiation pressure above thousands of Pascas when it is launched with an optical power as low as 1 mW. With a sufficient power, the radiation pressure is able to push the cavity wall outward from its original position with a small displacement of dx. Consequently, the cavity resonance moves toward a longer wavelength because of the increase of the cavity optical path length.

For a given pump laser operating with both power and wavelength fixed, the cavity buildup power changes with the relative detuning of the cavity and the pump laser. When the input laser is in the blue detuning regime, an increase of the cavity resonance wavelength λ_0, reduces the cavity circulating power because of the increased detuning, which in turn lowers the radiation pressure itself. Then, the cavity starts to shrink under the restoring force of the structure deformation like a mechanical spring. As the optical cavity has a finite decay rate Γ_{t}, the dynamical backaction between the optical mode and mechanical motion leads to an observable transmission variation modulating on the cavity output spectrum without any modulation on the external input laser.

4.2 Cavity optomechanics

When the circulating power is high enough, the whispering-gallery optical wave produces a radiation pressure that is sufficient to drive the mechanical vibration mode of a microsphere. The mechanical mode for a microsphere has a motion that modulates the device radius which in turn modulates the optical cavity resonance. Such an op-

tomechanical coupling is described by the following coupled equations of motion [90]:

$$\frac{da}{dt} = \left(j\Delta_\omega - jg_{\rm om}x - \frac{\Gamma_{\rm t}}{2}\right)a + j\sqrt{\Gamma_{\rm e}}A_{\rm in}, \tag{4.1}$$

$$\frac{d^2x}{dt^2} + \Gamma_{\rm m}\frac{dx}{dt} + \Omega_{\rm m}^2 x = \frac{F_{\rm rad}(t)}{m_{\rm eff}} + \frac{F_{\rm L}(t)}{m_{\rm eff}}, \tag{4.2}$$

where a is the field amplitude of optical whispering-gallery mode (WGM), normalized such that $U = |a|^2$ represents the cavity mode energy. $A_{\rm in}$ is the input optical wave, normalized such that $P_{\rm in} = |A_{\rm in}|^2$ represents the input optical power. $\Gamma_{\rm t}$ is the photon decay rate of the loaded cavity, and $\Gamma_{\rm e}$ is the photon decay rate associated with the external waveguide coupling. $\Delta_\omega = \omega_{\rm l} - \omega_0$ is the frequency detuning from the input wave $\omega_{\rm l}$ to the cavity resonance ω_0. x represents the effective mechanical displacement of the radial breathing mode of the microsphere. $\Gamma_{\rm m}$, $\Omega_{\rm m}$, and $m_{\rm eff}$ are the damping rate, intrinsic resonance frequency, and effective mass of the mechanical mode, respectively. $g_{\rm om} = d\omega_0/dx$ is the optomechanical coupling coefficient, which scales inversely with the radius for a microsphere, with a magnitude of $|g_{\rm om}|/(2\pi) \approx$ 6.2 GHz/nm at a wavelength of 974 nm for a device with a diameter of 100 μm. $F_{\rm rad} = -g_{\rm om}|a|^2/\omega_0$ describes the radiation pressure produced by the optical wave inside the cavity and $F_{\rm L}$ is the thermal Langevin force responsible for the thermal Brownian motion of the mechanical mode.

Eq. 4.1 reflects the cavity optical resonance modulation due to its mechanical motion through the optomechanical coupling coefficient. Consequently, the cavity mechanical displacement changes the optical mode by altering the laser cavity detuning according to

$$\Delta'_\omega(x) = \omega_{\rm l} - \omega_0(x) = \omega_l - \left(\omega_0 - \frac{\omega_0}{R}x\right) = \Delta_\omega - g_{\rm om}x, \tag{4.3}$$

where R is the WGM microcavity radius. When the mechanical displacement is small, under the linear approximation, we assume the cavity optical mode has a field amplitude $a(t) = a_0(t) + \delta a(t)$ where $\delta a(t) << a_0(t)$. Subsequently, Eq. 4.1 can be decomposed into two equations

$$\frac{da_0}{dt} = \left(j\Delta_\omega - \frac{\Gamma_{\rm t}}{2}\right)a_0 + j\sqrt{\Gamma_{\rm e}}A_{\rm in} \tag{4.4}$$

$$\frac{d\delta a}{dt} = \left(j\Delta_\omega - \frac{\Gamma_{\rm t}}{2}\right)\delta a - jg_{\rm om}xa_0. \tag{4.5}$$

In steady state, Eq. 4.4 leads to

$$a_0 = \frac{j\sqrt{\Gamma_\mathrm{e}}A_\mathrm{in}}{\Gamma_\mathrm{t}/2 - j\Delta_\omega}. \tag{4.6}$$

Using the the Fourier transform defined as $\delta\widetilde{a}(\Omega) = \int_{-\infty}^{+\infty} \delta a(t) e^{j\Omega t} dt$, Eq. 4.5 is solved in frequency domain

$$-j\Omega\delta\widetilde{a}(\Omega) = \left(j\Delta_\omega - \frac{\Gamma_\mathrm{t}}{2}\right)\delta\widetilde{a}(\Omega) - jg_\mathrm{om}\widetilde{x}(\Omega)a_0 \tag{4.7}$$

and its complex conjugate

$$-j\Omega\delta\widetilde{a}^*(\Omega) = \left(-j\Delta_\omega - \frac{\Gamma_\mathrm{t}}{2}\right)\delta\widetilde{a}^*(\Omega) + jg_\mathrm{om}\widetilde{x}(\Omega)a_0^*. \tag{4.8}$$

So, we derive the spectral response of the perturbed field as

$$\delta\widetilde{a}(\Omega) = \frac{jg_\mathrm{om}a_0\widetilde{x}(\Omega)}{i(\Delta_\omega + \Omega) - \Gamma_\mathrm{t}/2} \tag{4.9}$$

and

$$\delta\widetilde{a}^*(\Omega) = \frac{jg_\mathrm{om}a_0^*\widetilde{x}(\Omega)}{i(\Delta_\omega - \Omega) + \Gamma_\mathrm{t}/2}. \tag{4.10}$$

Note in Eq. 4.2, the Langevin force $F_\mathrm{L}(t)$ obeys the statistical properties in the frequency domain [91]

$$\left\langle \widetilde{F}_\mathrm{L}(\Omega_\mu)\widetilde{F}_\mathrm{L}(\Omega_\nu)\right\rangle = m_\mathrm{eff}\Gamma_\mathrm{m}k_\mathrm{B}T2\pi\delta(\Omega_\mu - \Omega_\nu) \tag{4.11}$$

where T is the temperature and k_B is the Boltzmann constant. Ignoring the high order perturbation, the optical force can be approximated as

$$F_\mathrm{rad}(t) = -\frac{g_\mathrm{om}|a|^2}{\omega_0} = -\frac{g_\mathrm{om}}{\omega_0}[|a_0|^2 + a_0^*\delta a(t) + a_0\delta a^*(t)]. \tag{4.12}$$

The first term defines the new equilibrium position of the cavity boundary and can be removed for simplicity by readjusting the mechanical displacement. With the consideration of Eq. 4.9 and 4.10, the Fourier transform of the optical force becomes

$$\widetilde{F}_\mathrm{opt}(\Omega) \equiv \widetilde{f}_0(\Omega)\widetilde{x}(\Omega) \tag{4.13}$$

with

$$\widetilde{f}_0(\Omega) = -\frac{2g_{om}^2|a_0|^2\Delta_\omega}{\omega_0}\frac{\Delta_\omega^2 - \Omega^2 + (\Gamma_t/2)^2 + j\Gamma_t\Omega}{[(\Delta_\omega+\Omega)^2+(\Gamma_t/2)^2][(\Delta_\omega-\Omega)^2+(\Gamma_t/2)^2]} \tag{4.14}$$

Here the optical force is linearly proportional to the mechanical displacement. In addition, we solve the Eq. 4.2 by Fourier transform and obtain

$$\widetilde{L}(\Omega)\widetilde{x}(\Omega) = \frac{\widetilde{F}_L(\Omega)}{m_{\text{eff}}} \tag{4.15}$$

where we define $\widetilde{L}(\Omega) \equiv \Omega_m'^2 - \Omega^2 - j\Gamma_m'\Omega$. The new mechanical frequency Ω_m' and decay rate Γ_m' is induced by the optical force as

$$\begin{cases} \Omega_m'^2 = \Omega_m^2 - \Re\left\{\frac{\widetilde{f}_0(\Omega)}{m_{\text{eff}}}\right\} \\ \Gamma_m' = \Gamma_m + \Im\left\{\frac{\widetilde{f}_0(\Omega)}{\Omega m_{\text{eff}}}\right\} \end{cases}, \tag{4.16}$$

where $\Re\{\cdot\}$ and $\Im\{\cdot\}$ are the real and imaginary part of the complex function $(\cdot)$. For a continuous-wave (CW) laser input with a constant power, from Eq. 4.6 we have

$$|a_0|^2 = \frac{\Gamma_e P_{\text{in}}}{(\Gamma_t/2)^2 + \Delta_\omega^2}. \tag{4.17}$$

Therefore, the interaction between the intracavity optical wave and the mechanical motion modifies the dynamics of the mechanical mode, resulting in an effective mechanical damping rate Γ_m' and an effective mechanical frequency Ω_m' given by [90],

$$\Gamma_m' \approx \Gamma_m - \frac{2g_{om}^2 P_{\text{in}}}{m_{\text{eff}}\omega_0}\frac{\Delta_\omega\Gamma_t\Gamma_e}{(\Gamma_t/2)^2+\Delta_\omega^2}\frac{1}{[(\Delta_\omega+\Omega_m)^2+(\Gamma_t/2)^2][(\Delta_\omega-\Omega_m)^2+(\Gamma_t/2)^2]}, \tag{4.18}$$

$$\Omega_m'^{\,2} \approx \Omega_m^2 + \frac{2g_{om}^2 P_{\text{in}}}{m_{\text{eff}}\omega_0}\frac{\Delta_\omega\Gamma_e}{(\Gamma_t/2)^2+\Delta_\omega^2}\frac{\Delta_\omega^2 - \Omega_m^2 + (\Gamma_t/2)^2}{[(\Delta_\omega+\Omega_m)^2+(\Gamma_t/2)^2][(\Delta_\omega-\Omega_m)^2+(\Gamma_t/2)^2]}, \tag{4.19}$$

which are obtained from Eq. 4.1 and 4.2 by treating the mechanical motion as a perturbation to the optomechanical system.

Equation 4.18 shows the dependence of optomechanical amplification/cooling on the laser-cavity detuning. The mechanical damping rate Γ_m' is modulated by the radiation pressure according to the sign of the detuning Δ_ω. When the pump laser

is operating at a frequency ω_l higher than the cavity resonance ω_0, the blue detuned pump laser ($\Delta_\omega > 0$) leads to a decrease of the mechanical damping rate. At a certain detuning, a negative damping rate occurs with sufficient optical power. Therefore, the cavity mechanical motion (Ω_m) is amplified by the radiation pressure and induces the mechanical instability. Due to the backaction of the caity motion, the circulating light (ω) is then Doppler shifted so that has two sidebands at ($\omega - \Omega_m$) and ($\omega + \Omega_m$) on its spectrum [21]. Affected by the power distribution within one cavity resonance mode, the sideband with a frequency closer to the resonance has a enhanced intensity compared to the other. The unbalanced sidebands cause a net energy transfer from optical mode to mechanical motion in the blue detuning regime, since the sideband with lowered frequency photons ($\omega - \Omega_m$) is enhanced by the cavity.

With a red detuned laser on the opposite side of the cavity resonance ($\Delta_\omega < 0$), the negative sign of the frequency detuning adds an extra effective damping rate to the intrinsic one so that further suppresses the mechanical motion of the cavity. There exits an net energy transfer from the mechanical motion to the optical mode through the optomechanics. Therefore, the cavity is considered to be cooling down by the optical force under this situation.

Physically, the CW optical wave launched into the cavity produces radiation pressure around the equator of the microsphere along the radial direction to actuate the radial-breathing mechanical mode in Eq. 4.2. The induced mechanical motion changes the cavity length and thus shifts the optical resonance frequency, which in turn modulates the optical wave inside the cavity according to Eq. 4.1. The resulting dynamic backaction between the optical field and mechanical motion can be either in phase or out of phase with the mechanical motion, depending on the laser-cavity detuning, thus amplifying or cooling the mechanical motion. The efficiency of optomechanical amplificaiton/cooling depends on the optomechanical coupling strength g_{om}, the optical Q, and the laser-cavity detuning Δ_ω. Therefore, the high optical quality and strong optomechanical coupling in our device would provide efficient optomechanical excitation.

In addition, on the blue detuning side ($\Delta_\omega > 0$), the optical wave amplifies the mechanical motion and leads to a decrease of the mechanical damping rate that depends linearly on the optical power. A large enough optical power is able to boost the mechanical motion above the oscillation threshold resulting in a coherent optomechanical oscillation (OMO) with a very narrow linewidth. Equation 4.19 shows the optical spring effect where the mechanical frequency depends sensitively on the

laser-cavity detuning Δ_ω. This effect underlies the principle of cavity optomechanical transduction sensing, which will be discussed in detail later.

4.3 Optomechanical oscillation in an aqueous environment

Since the first demonstration of OMO early this century [66, 67, 92, 90, 19, 20, 18, 93, 94, 95, 96, 97, 98, 99], the coherent regenerative optomechanical oscillation, being possible with the substantial optical force established at the cavity edge, has displayed pure spectral properties and unique back action against thermal noises and is desirable for sensing applications. Its adoption to sensing, however, is limited in a gaseous environment [28, 29, 69]. The rare demonstration of such system in an aqueous environment lies in the fact that when a cavity is immersed in a liquid bath where a biospecimen dwells, the suspension actuates strong viscous force against the cavity oscillation. This makes the optomechanical oscillation highly dissipative except in the cases where a superfluid was adopted [100]. Up to date, the sole demonstration of an optomechanical system compatible to liquid suspensions is the bottleneck cavity where the liquid was injected to the inner tube of the cavity to circumvent the mechanical energy dissipation to the aquarium [101]. Although demonstrations on sensing have been reported on this platform, the fact that the relative high mechanical oscillation frequency and large spatial separation between the optical mode and suspensions under test makes it less favourable in sensing applications compared to the microcavity reactive sensing established in previous experiments [10, 74].

To excite the coherent mechanical oscillation of a microcavity immersed in liquid, the optical quality factor of the microcavity must be maintained at a high value to establish a large intracavity power so that the dynamic backaction is strong enough for regenerative optomechanical oscillation. In our experiment, we demonstrated that by immersing a silica microsphere in heavy water for lower optical absorption at an operating wavelength around 970 nm, the optical quality factor of the microsphere can reach around ten million. Consequently, the condition was met and coherent regenerative optomechanical oscillation was observed.

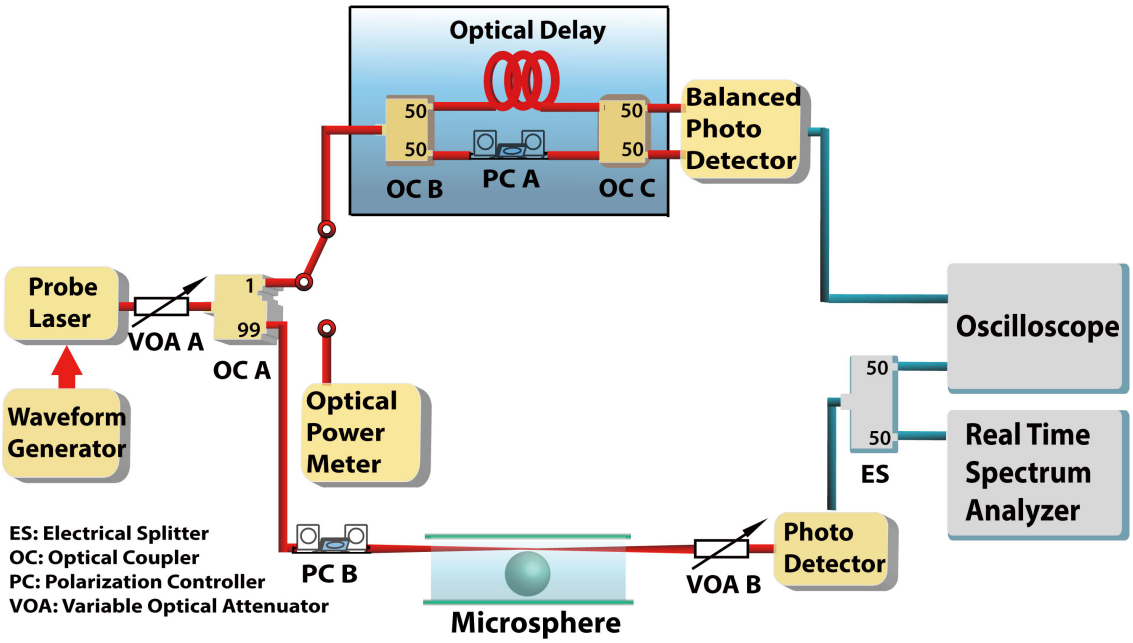

Figure 4.2: Experiment setup for the OMO measurements.

4.4 Experiment results and discussions

The experiment setup is shown in Fig. 4.2. In our experiment, a Newport 6300LN external cavity tunable laser operating at 970 nm range was used as the pump source to drive the cavity oscillation. Throughout the experiment, the laser output power remained unchanged for a constant Schawlow-Townes limited laser frequency noise. To control the amount of optical power delivered to the cavity, the laser output was regulated by a variable optical attenuator (VOA A) before entering a 20-dB optical directional coupler (OC A). The 99% port was connected to the input of a tapered optical fiber to deliver light to the silica microsphere under test. The microsphere was fabricated by melting a silica fiber tip into a 100 μm diameter sphere as shown previously. The microsphere was immersed in heavy water (D_2O) and mounted on a nanopositioner to precisely control the coupling position between the microsphere and fiber taper. The intracavity optical power of the microsphere was interrogated by the same tapered fiber whose output was connected to a photodetector (New focus 1811) to convert transmitted optical signal to electrical signal. The electrical signal was split by a 50/50 electrical splitter whose outputs were connected to an oscilloscope (Agilent DSO 90404A) and a real time spectrum analyzer (Tektronix RSA 3408B) for subsequent measurements.

During the experiment, we linearly scanned the optical frequency of the probe laser using a waveform generator and adjusted the coupling between the tapered fiber and the microsphere such that the oscillation was observable in aquarium as the transmission spectrum shown in Fig. 4.3. The input optical power of the cavity was around 2.5 mW. The typical thermal broadening effect moulted with the intensity oscillation close to the cavity resonance is displayed on the spectrum. As indicated in the insets, the oscillation was single mode when the optical power dropped in the cavity is slightly above the threshold power while high order harmonics occurs at higher drop power level.

To measure the quality factor of the cavity optical resonance mode, the 1% output branch of the directional coupler was connected to a reference interferometer thermally stabilized in a foam box filled with ice water mixture. The transmitted optical signal from the interferometer was received by a balanced photo detector for real time laser frequency tracking. When the laser was in continuous wave (CW) mode, the spectrum of the electrical signal from the balanced photo detector was captured by an Agilent N9010A EXA signal analyzer. As shown in the Fig. 4.4, the power

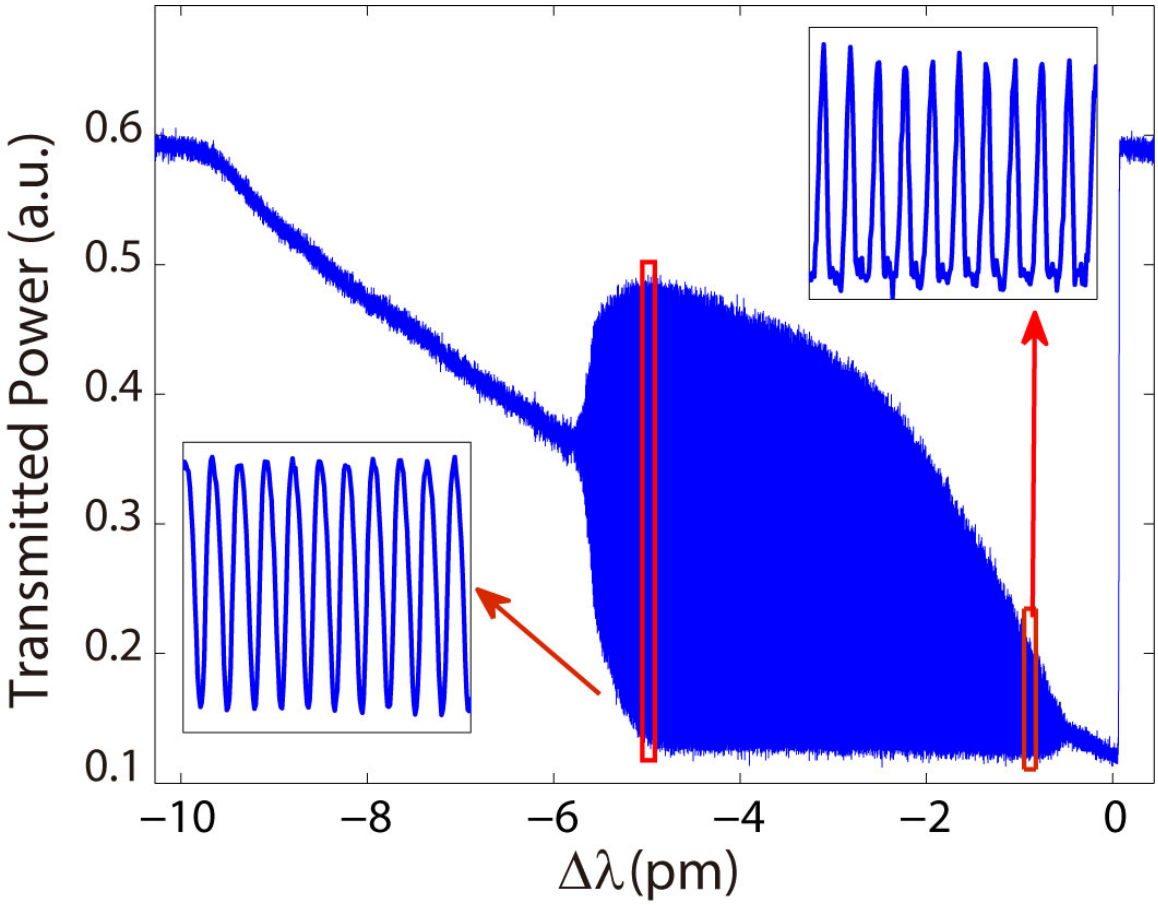

Figure 4.3: Transmitted optical power as a function of probe laser wavelength detune. At a dropped optical power close to the threshold power, the left inset displayed a sinusoidal spectrum while at a high dropped power the spectrum displayed in the right inset was distorted by the high order harmonics.

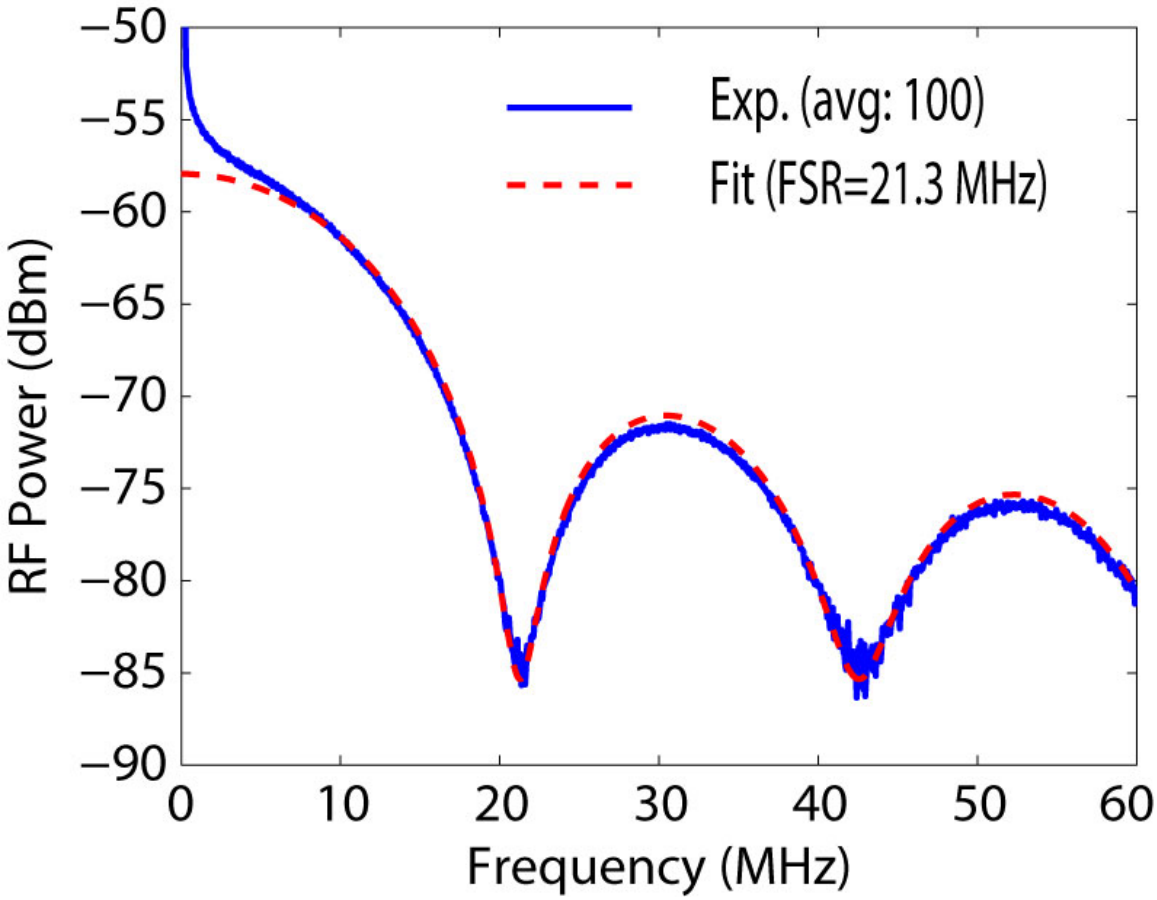

Figure 4.4: RF power spectrum of the reference interferometer output calibrated from the dark current spectrum.

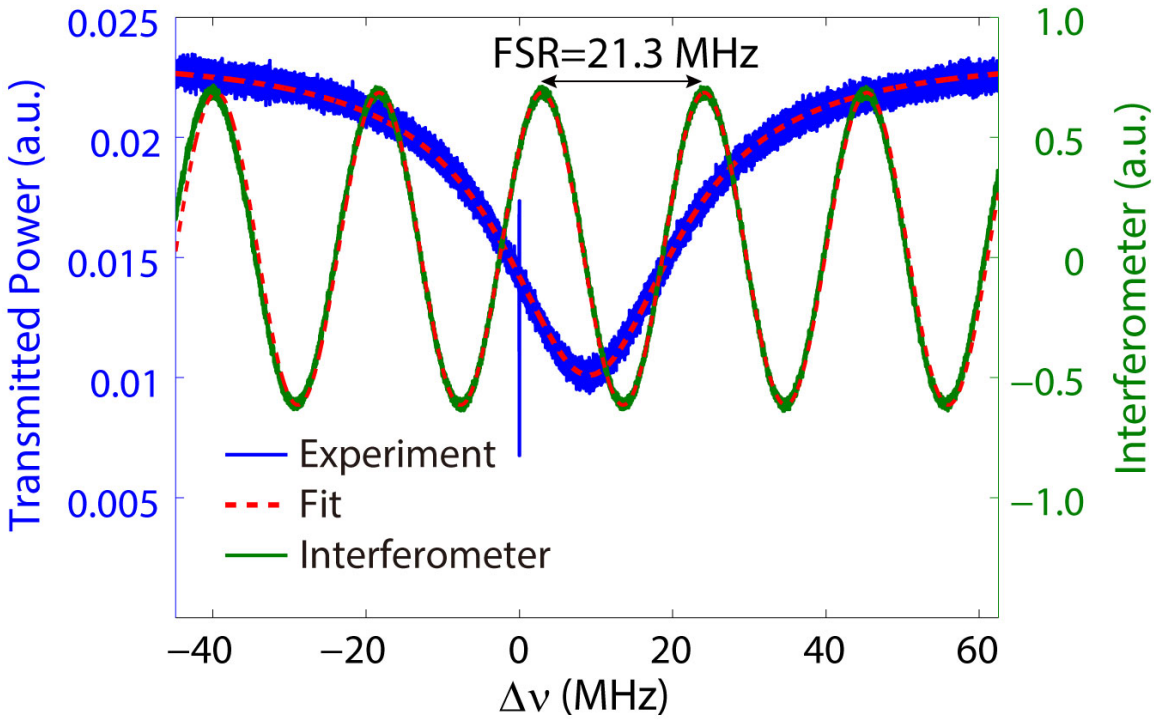

Figure 4.5: Cavity transmitted optical power (blue trace) displays a Lorentzian shape. The laser frequency is calibrated through the transmitted signal of the reference interferometer (green trace). The red dashed lines are least square fitting results.

spectrum of the signal displayed a sinc-square shape (blue trace). Note the spectrum was averaged over 100 measurements and calibrated by subtracting it from the dark current spectrum averaged over the same number of traces. A least square fit of the spectrum to a sinc-square function (red dashed trace) indicates the free spectral range $\Delta\nu_{\mathrm{FSR}}$ of the interferometer to be 21.3 MHz.

We then scanned the optical frequency of the laser linearly and reduced the probe laser power till thermal broadening effects were not observable from the cavity transmission spectrum. As shown in the Fig. 4.5, in the absence of thermal effects, transmitted signal from the cavity (blue trace, averaged over 100 traces) displayed a Lorentzian shape and the interferometer signal (green trace) has a sinusoidal shape with a periodicity equals to $\Delta\nu_{\mathrm{FSR}}$. Therefore, by comparing the fitted curves of both spectra, we obtained an intrinsic optical Q of 1.4×10^7 when the microsphere was immersed in heavy water (D_2O). We measured the intrinsic quality factor by both up-scanning and down-scanning the laser wavelengths. Both measurements yield the same optical Q values, indicating the transmission spectrum was not affected by the thermal effects. Under the operation coupling condition, an intrinsic optical Q of 1.4×10^7 was measured in heavy water, resulting an overall loaded optical Q of $9.8{\times}10^6$.

In the next stage, we switched the laser in the continuous wave (CW) mode and the coupler (OC A) 1% output branch to an optical power meter for monitoring purposes. The amount of pump laser power delivered to the cavity was adjusted by the first variable optical attenuator (VOA A). To facilitate our measurement, we adjusted the attenuator (VOA B) accordingly such that at off-resonance wavelength, the photodetector output voltage measured from the oscilloscope remains at a preset value of around 0.6 V regardless of the power delivered to cavity. We then tuned the optical frequency of the laser toward cavity resonance frequency till the voltage at the photodetector dropped around 50%. Each radio frequency (RF) spectrum of the cavity transmitted signal (Fig. 4.6) was captured by the real time spectrum analyzer. To improve the signal-to-noise ratio (SNR), each spectrum was averaged over 100 spectral traces collected seamlessly at the same drop power level while the traces of Fig. 4.7 was averaged over 500 times.

From Fig. 4.6, the coherent oscillation is evident observing that the linewidth of the oscillation peak narrows rapidly when the optical power dropped to the cavity exceeds 1 mW. A detailed study of spectra in Fig. 4.6 indicates that the linewidth of the spectrum decreases gradually from 269 kHz when the dropped power is well below

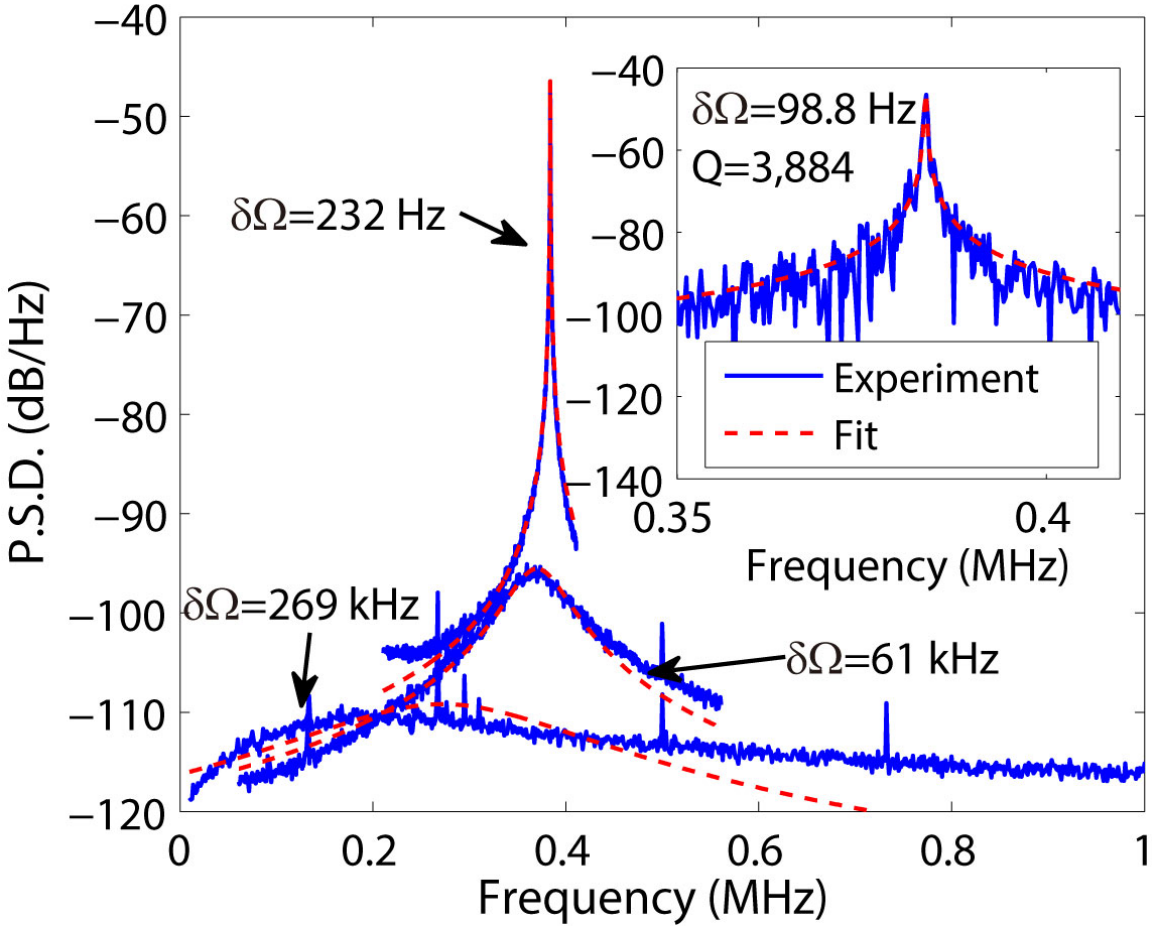

Figure 4.6: RF spectra at dropped power of 1.1 mW, 1 mW and 0.4 mW, least square fittings to the Lorentzian function indicate the linewidths of the optomechanical tones to be 232 Hz, 61 kHz and 269 kHz respectively. In the main plot, each spectrum was averaged over 100 spectral traces collected seamlessly at the same drop power level. The inset is the spectrum of single trace measurement.

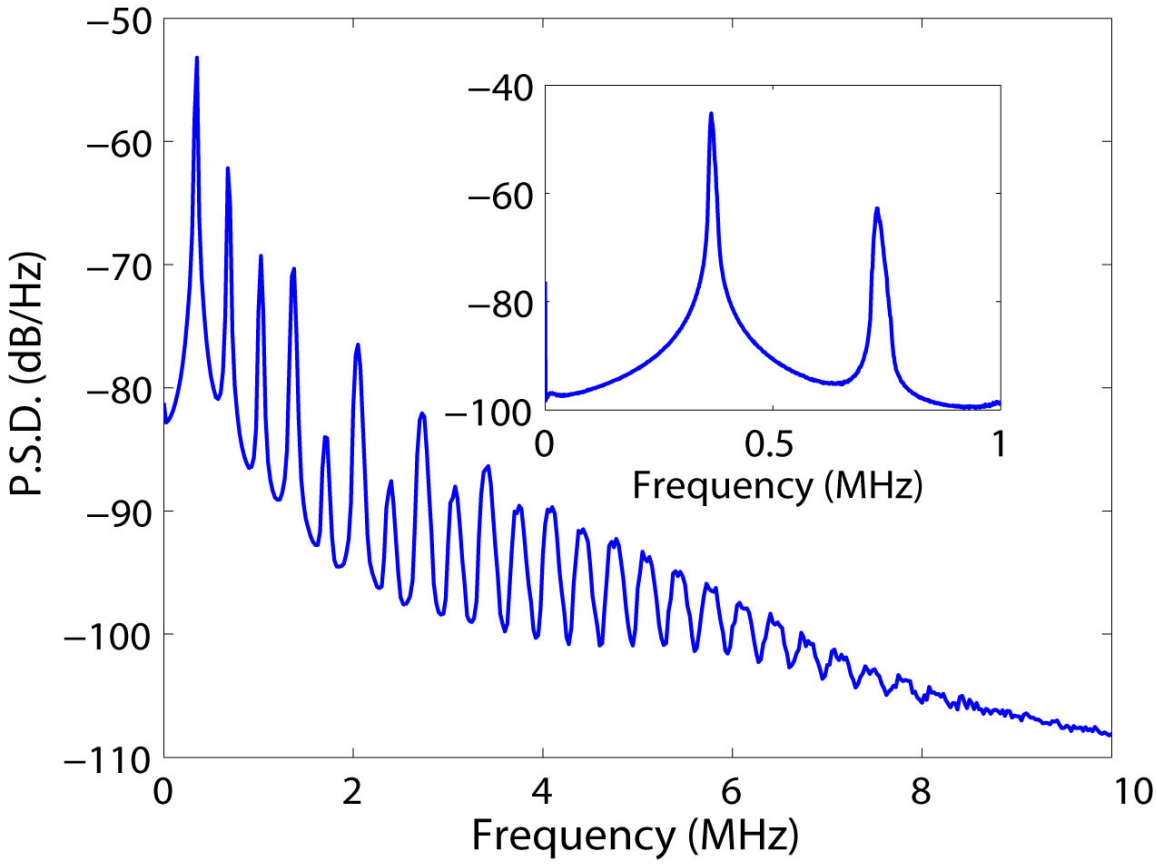

Figure 4.7: In a separate measurement, as high as 24-th order harmonics was observed in a frequency span of 10 MHz. The inset further displayed the spectrum with a frequency span set at 1 MHz.

threshold (0.4 mW) to 61 kHz at a power level close to the threshold (1.0 mW). When the dropped power reaches 1.1 mW, the linewidth narrows down to 232 Hz rapidly. Note that the calculated linewidth on an averaged spectrum is broadened due to frequency jitter. A least square fit (red trace) to a single spectrum trace displayed as the blue trace in the inset yields a linewidth of 99 Hz, corresponding to a super mechanical quality factor $Q_{\mathrm{m}} = 3,884$.

In Fig. 4.7 we further verified the generation of high order harmonics at high dropped optical power. As shown in the main plot, as many as 24 higher order harmonics peaks are visible over a frequency span of 10 MHz. The dropped optical power was 2.6 mW. Meanwhile the frequency doubling of the second harmonic is evident from the inset when the span is set to 1 MHz. The traces were averaged over 500 times.

Then, we plotted the cavity mechanical energy normalized to its peak value (blue circle markers) as a function of the dropped power in Fig. 4.8. As shown, the mechanical energy increases linearly with the dropped power at above a threshold power level. This further confirms the coherent nature of the mechanical oscillation. A linear fit to the mechanical energy (red dashed trace) reveals the threshold power to be 0.98 mW. In the inset of this figure, we plotted the peak frequency as a function of the dropped power. As shown, when below threshold the peak frequency drives gradually from 253 kHz at a dropped power of 0.3 mW to 370 kHz at 1.0 mW due to the optical spring effect [20]. A linear extrapolation to the peak frequency trace (red dashed line) predicts an intrinsic mechanic frequency of 199 kHz in the absence of optical force. To obtain the intrinsic mechanical quality factor Q_{m}, we plotted the linewidth (blue circles) as a function of the dropped power in Fig. 4.9. A linear fit (red dashed line) indicates an intrinsic linewidth of 431 kHz at zero dropped power level, yielding a Q_{m} of 0.5. Here the linewidth at each dropped power level was computed through a least square fitting of each RF spectrum to a Lorentzian function. At the lowest optical power around 0.3 mW, the spectrum significantly deviates from a Lorentzian shape, causing the estimated linewidth to be inaccurate. Therefore we exclude this data point from the linear fitting of linewidth displayed as red dashed line in Fig. 4.9. It is also worth mentioning that unlike those reported in the previous publication [101], the oscillation peak observed in the experiment was located at low frequencies around several hundred kHz.

Finally we characterised the oscillation frequency stability by taking the spectrogram as displayed in Fig. 4.10. The black line overlapped with the spectrogram is

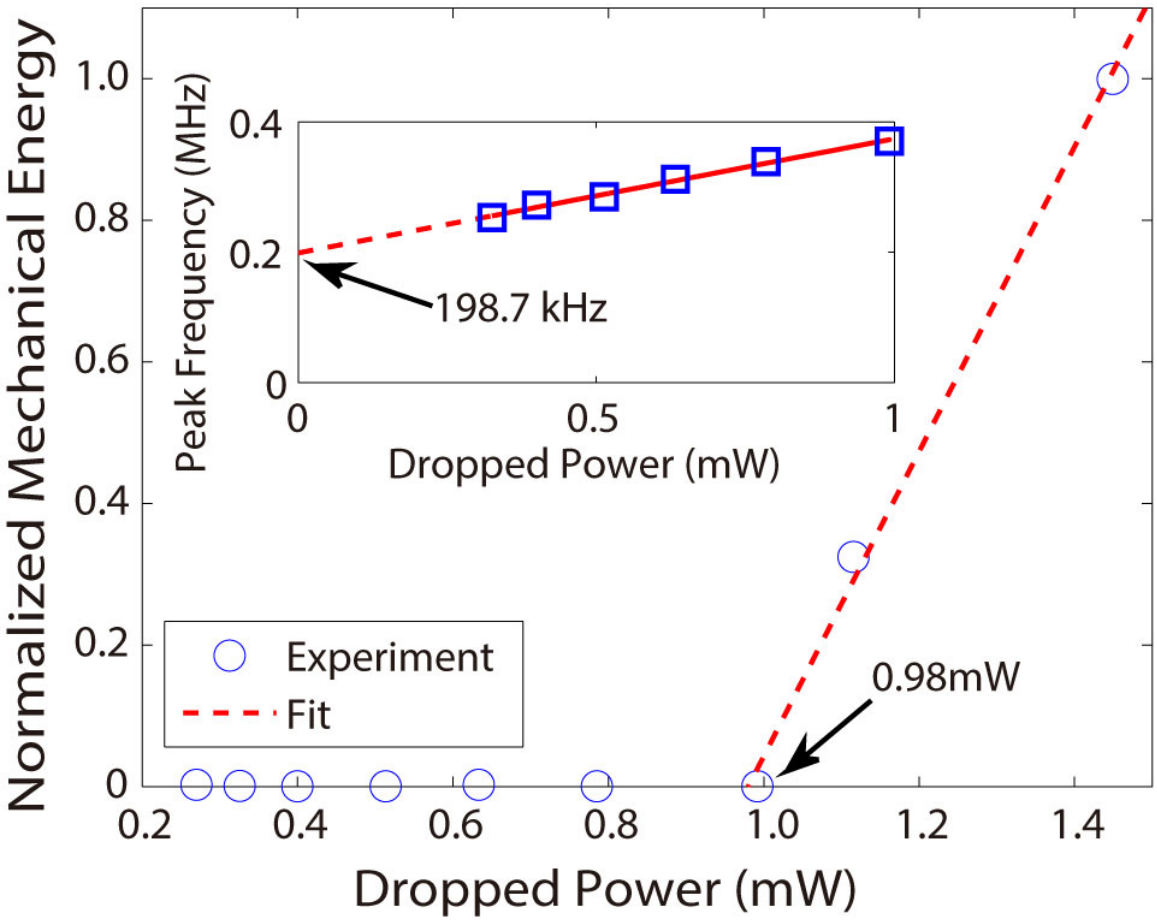

Figure 4.8: Mechanical energy (normalized to the maximum value) as a function of the dropped power. The peak frequency as a function of the dropped power is displayed in the inset and a linear extrapolation predicts an intrinsic mechanical frequency of 198.7 kHz.

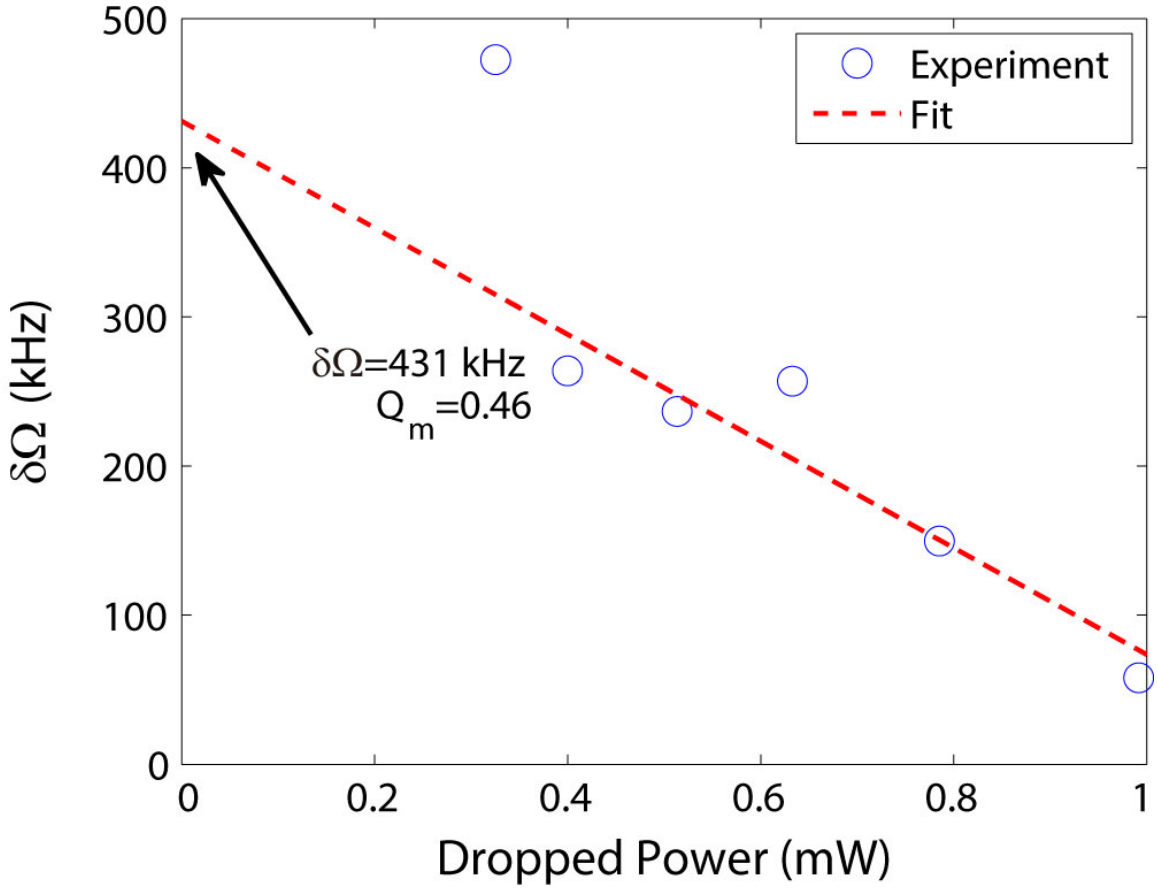

Figure 4.9: The plot of mechanical linewidth vs dropped power, which indicates an intrinsic mechanical linewidth of 431 kHz and an effective mechanical quality factor of $Q_{\mathrm{m}} = 0.5$ through the linear extrapolation.

the peak frequencies of the spectra calculated by the least square fitting. In this plot, the standard deviation of the peak oscillation frequencies was computed to be 130 Hz over a time span of 392 ms. Note that such low frequency fluctuation makes the opto-mechanical oscillation an attractive tool for highly sensitive nanodetection.

4.5 Summary

In summary, we demonstrated the optomechanical oscillation of a silica microsphere immersed in heavy water. The intrinsic optical Q of the microsphere was maintained above ten million in the aqueous environment, when the probe laser was operating around 970 nm wavelength. The high optical Q combined with sufficient overlap between cavity optical and mechanical modes makes it possible to establish a high intra-cavity optical force sufficient for optomechanical oscillation under the highly dissipative environment. It is worth noting that an optimum choice of pump laser wavelength may further reduce the optical absorption loss in water to increase the cavity optical Q for larger intracavity power. For example, the cavity Q can be boosted up to above 100 million without the system reconfiguration except switching the probe laser wavelength into the visible range. It may also increase the overlap between cavity optical and mechanical modes to change the energy transfer rate from optical to mechanical. Both effects will contribute to a lower oscillation threshold power. Therefore numerical verification of the opto-mechanical oscillation in aqueous environment is currently under investigation to determine the optimum pump laser wavelength for minimum threshold power and for better understanding of the system.

Furthermore, the investigation of its mechanical frequency spectrogram manifested the pure frequency tone of the cavity oscillation induced by the radiation pressure. Due to its narrow linewidth and high system stability, we realized that opto-mechanical oscillation for biosensing applications in the aqueous environment would be achievable with the use of higher power laser to overcome the excessive optical absorption from such suspensions. Based on the established platform, we will demonstrate the single nanoparticle detections in DPBS suspensions in the following chapter. More interestingly, the sensing results indicate an improved sensitivity compared to the conventional cavity reactive sensing.

The work in this chapter has been published in Optics Express [102], which is a collaboration with the researchers from University of Rochester, Wei Jiang and Qiang Lin. Our collaborators provided the theoretical analysis while the author carried the

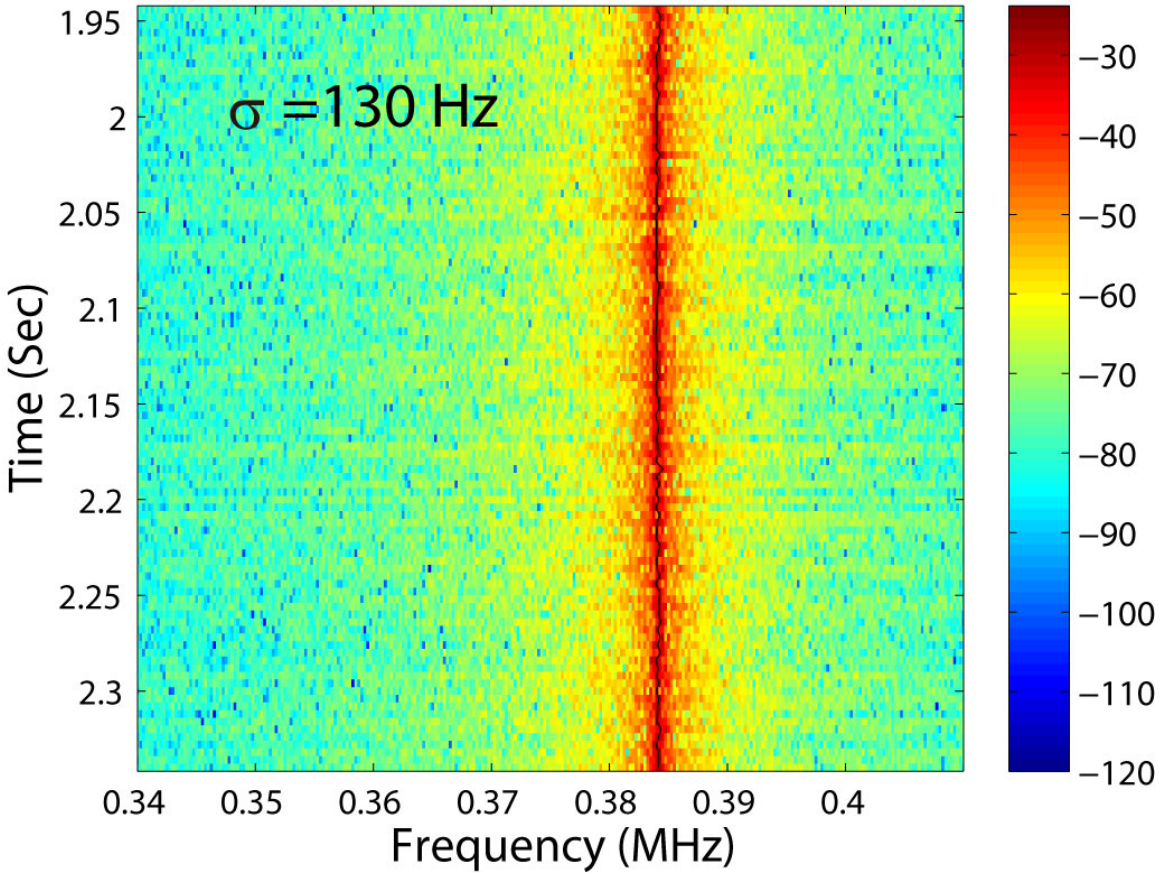

Figure 4.10: Spectrogram of the optomechanical oscillation indicates a 130 Hz standard deviation of the oscillation peak over a time span of 392 ms.

experiments. The author would like to thank Prof. Rustom B. Bhiladvala for fruitful discussions on the related works.

Chapter 5

Optical Spring Sensing

Sensitive detection of a single nanoparticle/molecule is essential for many applications ranging from medical diagnostics, drug discovery, security screening, to environmental science. In the past decades, a variety of approaches have been developed to observe single particles down to molecular scale [103, 104], among which optical detection based on high-Q microcavities has shown significant advantages for its high sensitivity and label-free operation [8, 12, 11, 82, 105, 106, 107]. To date, most microcavity sensors are dispersive in nature where particle detection is achieved by monitoring the cavity resonance wavelength shift induced by the binding events. Here we propose and demonstrate an optomechanical approach based upon a quivering high-Q whispering gallery microcavity driven by an optical force. By taking advantages of the intriguing optically induced spring in the device, we are able to enhance the sensing resolution by orders of magnitude compared with conventional approaches, which allows us to detect single Bovine Serum Albumin (BSA) proteins with a molecular weight of 66 kDa at a signal-to-noise ratio of 16.8. With a unique optomechanical nature, the demonstrated approach opens up a distinctive avenue that not only enables biomolecule sensing and recognition at individual level, but also exhibits great potential for studying/manipulating mechanical properties of individual biomolecules and their interactions that are crucial for cellular machineries and biological functionalities.

5.1 Sensing principle

Binding of a particle to a high-Q optical microcavity perturbs the cavity mode at a resonance wavelength of λ_0, resulting in a cavity resonance shift of $\delta\lambda$ which in turn changes the cavity transmission. This mechanism underlies the majority of current microcavity sensors [13, 10], with a sensing resolution dependent critically on the optical quality factor (Q) [108]. To date, the highest resolution reported is a resonance shift of $(\delta\lambda/\lambda_0) = 3\times10^{-10}$ achieved with an optical Q of one hundred million at a visible wavelength in an aqueous environment [11], which, however, is still larger than that induced by a single protein binding event [13]. Consequently, detection of a single protein molecule down to 1 kDa requires incorporating a plasmonic nanoantenna on the microcavity to enhance the resonance wavelength shift [16, 17, 86, 109], at a price of significant reduction of effective detection area.

On the other hand, the optical wave cycling inside the microcavity is able to produce a radiation pressure that interacts with the mechanical motion of the device (Fig. 5.1). Such optomechanical coupling flourishes in profound physics that has been intensively explored in recent years, particularly in the context of quantum control of mesoscopic mechanical motion [66, 67, 90, 92, 110]. When the laser wavelength λ_l is blue detuned to the cavity resonance, the optical wave can efficiently boost the mechanical motion above the threshold of regenerative oscillation [66, 90], resulting in highly coherent optomechanical oscillation (OMO) with a narrow mechanical linewidth. Of particular interest is that the optical wave inside the cavity is able to produce an effective mechanical rigidity [90], leading to an OMO frequency f_m depending sensitively on the laser-cavity detuning $\Delta_\lambda = \lambda_l - \lambda_0$. Consequently, any tiny perturbation to the cavity resonance wavelength, $\delta\lambda$, induced by particle/molecule binding would be readily transferred to the frequency shift, δf_m, of the mechanical motion: $\delta f_m = -\frac{df_m}{d\Delta_\lambda}\delta\lambda$, thus enabling an efficient transduction mechanism to amplify the resonance wavelength sensing.

As the minimal detectable frequency shift of OMO is determined by its linewidth Δf_m, the minimal detectable optical cavity resonance shift is thus given by $(\delta\lambda/\lambda_0)_{min} = \frac{\Delta f_m}{\lambda_0}/(-\frac{df_m}{d\Delta_\lambda})$. With a narrow linewidth of coherent OMO and a significant frequency tuning slope $|df_m/d\Delta_\lambda|$, the intriguing optical spring effect would thus offer an elegant approach for sensitive probing of cavity resonance variation, with a sensing resolution

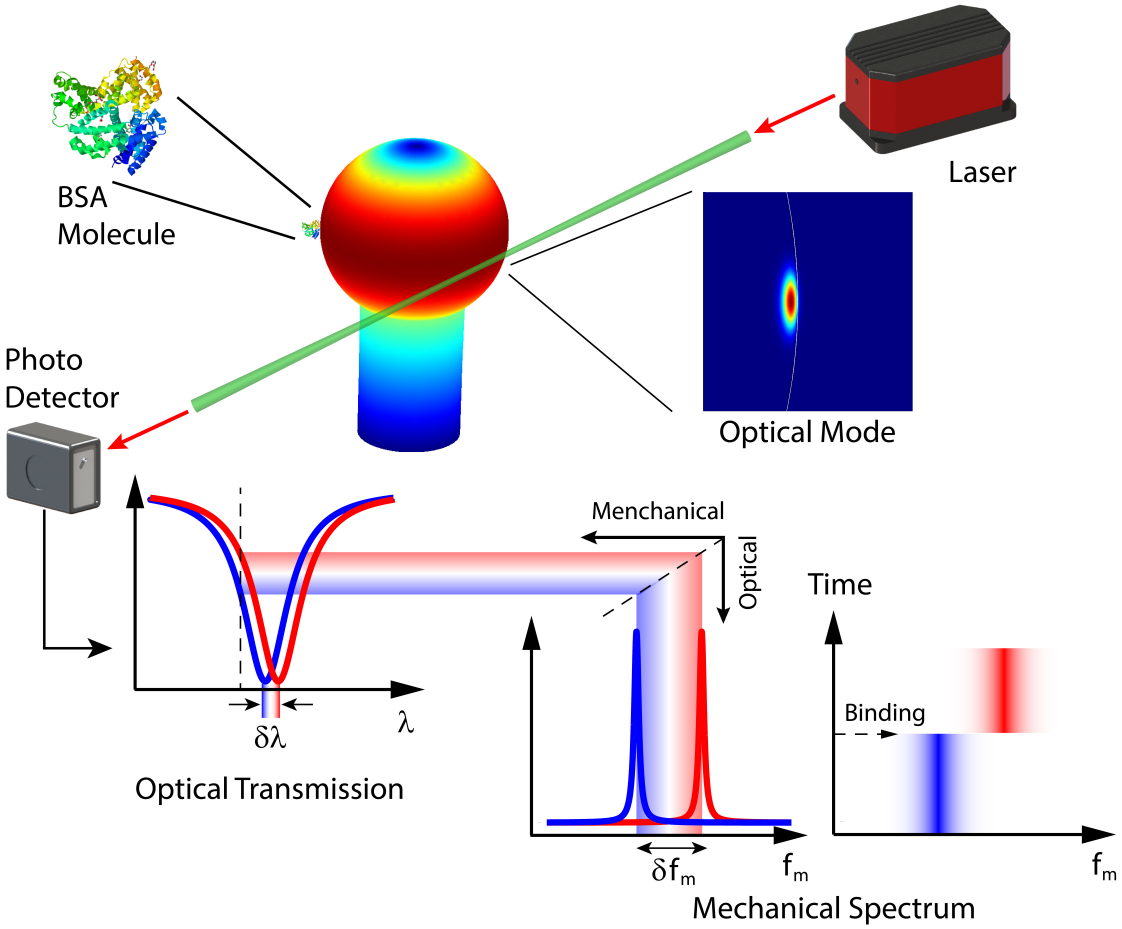

Figure 5.1: Schematic illustrating the sensing mechanism. A protein molecule bound to an optomechanically oscillating microsphere yields an optical resonance shift $\delta\lambda$, which is transduced to a mechanical frequency shift δf_{m}. The color map on the microsphere shows the radial breathing mechanical mode simulated by the finite element method.

given by

$$\left(\frac{\delta\lambda}{\lambda_0}\right)_{\min} = \frac{1}{\eta_{\mathrm{om}} Q_{\mathrm{m}}^{\mathrm{eff}} Q_{\mathrm{t}}}, \tag{5.1}$$

where $Q_{\mathrm{m}}^{\mathrm{eff}}$ is the effective mechanical Q factor of OMO, defined as the ratio between the frequency f_{m} and the linewidth Δf_{m} of the OMO: $Q_{\mathrm{m}}^{\mathrm{eff}} \equiv f_{\mathrm{m}}/\Delta f_{\mathrm{m}}$. Q_{t} is the loaded optical Q, and η_{om} represents the optomechanical transduction factor for sensing whose magnitude depends on laser-cavity detuning, with a value in the order of $\eta_{\mathrm{om}} \sim 1$. Equation 5.1 shows clearly that the sensing resolution scales not only with the optical Q of the cavity as in conventional microcavity sensors, but also with the effective mechanical Q of OMO. Consequently, in principle, the proposed cavity optomechanical spring sensing is able to enhance the sensing resolution by about a factor of $Q_{\mathrm{m}}^{\mathrm{eff}}$ compared with conventional approaches. As we will show below, the mechanical Q of coherent OMO in our device can reach a value above 10^6, resulting in a sensing resolution enhanced by orders of magnitude that is sufficient for single molecule detection.

To date, cavity optomechanics has been widely applied as a sensitive approach for probing mechanical displacement [66, 90]. However, the magnitude of mechanical motion is not relevant here. Instead, the optically induced frequency shift of the OMO is employed as the information carrier to transduce and to amplify the molecule binding signal. In this sense, we call our approach optical spring sensing. Although the optical spring effect has been known for a decade [111], to the best of our knowledge, this is the first time to realize the potential and the powerfulness of optical spring for particle/molecule sensing.

5.1.1 Optical spring effect

The optical spring effect provides an effective mechanical stiffness that relies on the radiation pressure produced by the WGM. A spring pulling away from its equilibrium position will oscillate as its elasticity exerts a restoring force to counter react the mechanical deformation. In a whispering gallery microcavity, the circulating optical wave exerts an optical force to deform the cavity from its equilibrium, causing it to oscillate mechanically in the same manner as a spring. Meanwhile, the cavity resonance wavelength changes as a result of the mechanical deformation, which in turn modulates the light intensity and the optical force. The mutual opto-mechanical

coupling in the process makes the cavity a forced harmonic oscillator and this phenomenon is also known as optomechanical oscillation (OMO) [67, 90, 110, 112].

It is well known that the harmonic oscillation angular frequency Ω_{m} of a spring follows the Hooke's law $\Omega_{\mathrm{m}} = \sqrt{k/m_{\mathrm{eff}}}$ where m_{eff} is the effective motional mass of a particular mechanical oscillation mode and k is the spring constant. In analogy, the oscillation angular frequency of the OMO can be described by the same equation, by including the radiation pressure contribution to the spring constant, $k = k_{\mathrm{mech}} + k_{\mathrm{opt}}$ [31]. Here, k_{mech} is the cavity elasticity induced intrinsic mechanical spring constant and k_{opt} is the optical spring constant produced by the optomechanical coupling. As the magnitude of the radiation pressure changes due to the cavity resonance detuning, the optical spring constant depends sensitively on the cavity resonance.

From the previous cavity reactive sensing mechanism, it has been fully explained that the WGM cavity resonance is highly sensitive to the change of its surrounding environment, such as the particle adsorption near its equator. As a result, the optical detuning $\Delta_\omega = \omega_{\mathrm{l}} - \omega_0$ expresses the shift of the cavity resonance ω_0 with regard to the fixed pump laser ω_{l}. Transduced by the optical spring effect, the small perturbation of the cavity resonance becomes an amplified frequency shift of the OMO that can be identified on the cavity mechanical frequency spectrogram for particle detections. Such a mechanical frequency shift transduced from the optical spring effect is described in detail in the following.

5.1.2 Mechanical frequency shift induced by particle binding

In general, particle adsorption at the microcavity modifies both the optical cavity resonance and the optical Q. According to the optical spring effect, the modifications on the optical mode are transduced to the mechanical motion and manifested by the behaviour of the mechanical frequency in Eq. 4.19 that

$$\begin{aligned} {\Omega'_{\mathrm{m}}}^2 &\approx \Omega_{\mathrm{m}}^2 + \frac{2g_{\mathrm{om}}^2 P_{\mathrm{in}}}{m_{\mathrm{eff}}\omega_0} \frac{\Delta_\omega \Gamma_{\mathrm{e}}}{(\Gamma_{\mathrm{t}}/2)^2 + \Delta_\omega^2} \frac{\Delta_\omega^2 - \Omega_{\mathrm{m}}^2 + (\Gamma_{\mathrm{t}}/2)^2}{[(\Delta_\omega + \Omega_{\mathrm{m}})^2 + (\Gamma_{\mathrm{t}}/2)^2][(\Delta_\omega - \Omega_{\mathrm{m}})^2 + (\Gamma_{\mathrm{t}}/2)^2]} \\ &= \frac{k_{\mathrm{mech}}}{m_{\mathrm{eff}}} + \frac{k_{\mathrm{opt}}(\Delta_\omega, \Gamma_{\mathrm{t}})}{m_{\mathrm{eff}}}. \end{aligned} \tag{5.2}$$

Equation 5.2 shows that the mechanical frequency depends on both the laser-cavity detuning and the optical Q, yielding a shift of the OMO frequency given by

$$\delta\Omega'_{\rm m} = \frac{\partial\Omega'_{\rm m}}{\partial\omega_0}\delta\omega_0 + \frac{\partial\Omega'_{\rm m}}{\partial Q_{\rm t}}\delta Q_{\rm t} = -\frac{\partial\Omega'_{\rm m}}{\partial\Delta_\omega}\delta\omega_0 - \frac{\Gamma_{\rm t}}{Q_{\rm t}}\frac{\partial\Omega'_{\rm m}}{\partial\Gamma_{\rm t}}\delta Q_{\rm t}, \tag{5.3}$$

where $\delta\omega_0$ and $\delta Q_{\rm t}$ are the variations of cavity resonance frequency and loaded cavity optical Q, respectively, induced by the particle binding. From Eq. 5.2, we obtain

$$\frac{\partial\Omega'_{\rm m}}{\partial\Delta_\omega} = \frac{g_{\rm om}^2 P_{\rm in}\Gamma_{\rm e}}{m_{\rm eff}\omega_0\Omega'_{\rm m}L_0L_+L_-}\left[L_0 + \Omega_{\rm m}^2\left(\frac{2\Delta_\omega^2}{L_0} - 1\right) - \frac{4\Delta_\omega^2(L_0-\Omega_{\rm m}^2)^2}{L_+L_-}\right], \tag{5.4}$$

$$\frac{\partial\Omega'_{\rm m}}{\partial\Gamma_{\rm t}} = \frac{g_{\rm om}^2 P_{\rm in}\Gamma_{\rm e}\Gamma_{\rm t}\Delta_\omega}{2m_{\rm eff}\omega_0\Omega'_{\rm m}L_0L_+L_-}\left[1 - (L_0-\Omega_{\rm m}^2)\left(\frac{1}{L_0}+\frac{1}{L_+}+\frac{1}{L_-}\right)\right], \tag{5.5}$$

where $L_0 \equiv \Delta_\omega^2+(\Gamma_{\rm t}/2)^2$, $L_+ \equiv (\Delta_\omega+\Omega_{\rm m})^2+(\Gamma_{\rm t}/2)^2$, and $L_- \equiv (\Delta_\omega-\Omega_{\rm m})^2+(\Gamma_{\rm t}/2)^2$.

In the sideband-unresolved regime with $\Omega_{\rm m} \ll \Gamma_{\rm t}$ where our sensing experiments operate, Eqs. 5.4 and 5.5 can be simplified considerably to

$$\frac{\partial\Omega'_{\rm m}}{\partial\Delta_\omega} = \frac{g_{\rm om}^2 P_{\rm in}\Gamma_{\rm e}}{m_{\rm eff}\omega_0\Omega'_{\rm m}}\frac{(\Gamma_{\rm t}/2)^2 - 3\Delta_\omega^2}{[\Delta_\omega^2+(\Gamma_{\rm t}/2)^2]^3}, \tag{5.6}$$

$$\frac{\partial\Omega'_{\rm m}}{\partial\Gamma_{\rm t}} = -\frac{g_{\rm om}^2 P_{\rm in}\Gamma_{\rm e}}{m_{\rm eff}\omega_0\Omega'_{\rm m}}\frac{\Gamma_{\rm t}\Delta_\omega}{[\Delta_\omega^2+(\Gamma_{\rm t}/2)^2]^3}. \tag{5.7}$$

When the particle size is small, the binding events introduce negligible impact on the optical Q, resulting in a linear relation between OMO frequency shift and the optical cavity resonance shift according to Eq. 5.3. In the cases when the particle size is large enough to yield a substantial degradation of the cavity Q, Eq. 5.3 indicates a deviation from such linear dependence due to the counteraction of the $\delta Q_{\rm t}$ term at the sensing operational regime. This agrees with the experimental observations shown in Fig. 5.11.

5.1.3 Cavity optomechanical transduction sensing resolution

The discussions above show that the OMO frequency depends linearly on the laser-cavity detuning within a certain range, providing that particle/molecule binding events introduce negligible cavity optical Q degradation. This mechanism offers an elegant approach to probe a single particle/molecule optomechanically. As the minimal detectable OMO frequency shift is determined by the linewidth of coherent OMO, from Eqs. 5.3 and 5.6, we obtain the sensing resolution given by Equation 5.1, with

the optomechanical transduction factor given by

$$\eta_{\rm om} = \left(1 - \frac{\Omega_{\rm m}^2}{\Omega_{\rm m}'^2}\right) \frac{1 - 3\bar{\Delta}_\omega^2}{(1 + \bar{\Delta}_\omega^2)\bar{\Delta}_\omega}, \tag{5.8}$$

where $\bar{\Delta}_\omega = \Delta_\omega/(\frac{\Gamma_{\rm t}}{2})$ is the normalized detuning with regard to the cavity resonance linewidth. For our sensing system, the OMO frequency is dominated by the optical spring, $\Omega_{\rm m}' \gg \Omega_{\rm m}$. As a result, the value of $\eta_{\rm om}$ primarily depends on the laser-cavity detuning and it usually ranges from 1 to 2 for proper sensing operation. At the present operation point with $\bar{\Delta}_\omega \approx 0.35$ used in the experiment, $\eta_{\rm om} \approx 1.6$.

5.1.4 Distinction from conventional mass sensing

In addition, this sensing approach is distinctive from the conventional micro-/nanomechanical sensing methods [25, 26] where the particle detection is realized by monitoring the mechanical frequency shift directly induced by the effective mass change from particle attaching, which, however, exhibits a minimal detectable mass change of $(\delta m)_{\rm min} = 2m_{\rm eff}/Q_{\rm m}^{\rm eff}$ that relies critically on the motional mass $m_{\rm eff}$ and the mechanical Q of the sensor. Although this mechanism was recently applied in combination with optical actuation and readout, it can only detect 1-μm-diameter silica beads with a sub-picogram resolution [28, 100]. For nanomechanical sensing, achieving single molecule resolution requires extremely tiny mass of employed nanomechanical oscillators [26, 103].

Here we provide a simple picture to show the distinctive nature of our proposed approach compared with conventional optomechanical and nanomechanical sensing. The oscillation angular frequency of the OMO is given simply by the Hooke's law, $\Omega_{\rm m}' = \sqrt{k/m_{\rm eff}}$, where $m_{\rm eff}$ is the effective motional mass and k is the effective spring constant. As discussed in the previous sections, the spring constant of an OMO contributes from two parts, $k = k_{\rm mech} + k_{\rm opt}$, where $k_{\rm mech}$ comes from the intrinsic mechanical rigidity of the device structure and $k_{\rm opt}$ is the optically induced spring which can be obtained from Eq. 5.2. Consequently, the OMO frequency shift can be induced by perturbation either to the mass $\delta m_{\rm eff}$, or to the spring constant, δk, given below:

$$\frac{\delta\Omega_{\rm m}'}{\Omega_{\rm m}'} = \frac{1}{2}\left(\frac{\delta k}{k} - \frac{\delta m_{\rm eff}}{m_{\rm eff}}\right) = \frac{1}{2}\left(\frac{\delta k_{\rm opt}}{k} + \frac{\delta k_{\rm mech}}{k} - \frac{\delta m_{\rm eff}}{m_{\rm eff}}\right). \tag{5.9}$$

Conventional nanomechanical sensing relies on the last two terms of the above equation, $\frac{\delta\Omega'_{\rm m}}{\Omega'_{\rm m}} = \frac{1}{2}\left(\frac{\delta k_{\rm mech}}{k} - \frac{\delta m_{\rm eff}}{m_{\rm eff}}\right)$, where the molecule binding either perturbs the effective mass or modifies the intrinsic mechanical spring constant of the mechanical resonator [25, 26]. Conventional OMO sensing relies on the last term, $\frac{\delta\Omega'_{\rm m}}{\Omega'_{\rm m}} = -\frac{1}{2}\frac{\delta m_{\rm eff}}{m_{\rm eff}}$, similar to nanomechanical sensing while with an optical readout [29, 28, 113].

In contrast, our approach takes advantage of the first term, $\frac{\delta\Omega'_{\rm m}}{\Omega'_{\rm m}} = \frac{1}{2}\frac{\delta k_{\rm opt}}{k}$. In particular, cavity optomechanics produces an optically induced spring that depends sensitively on the laser-cavity detuning, $\delta k_{\rm opt} = \frac{dk_{\rm opt}}{d\omega_0}\delta\omega_0$, where $\delta\omega_0$ is the resonance shift of the optical cavity induced by the molecule binding. Consequently, the OMO frequency shift is given by (see also Eq. 5.3)

$$\frac{\delta\Omega'_{\rm m}}{\Omega'_{\rm m}} = \frac{1}{2k}\frac{dk_{\rm opt}}{d\omega_0}\delta\omega_0. \tag{5.10}$$

As discussed in the previous sections, cavity optomechanics results in a significant magnitude of frequency tuning slope, $dk_{\rm opt}/d\omega_0$, that dramatically amplifies the cavity resonance shift induced by molecular binding and transduces it into the OMO frequency shift. It is this very distinctive nature of optical spring that provides a sensing resolution orders of magnitude higher than conventional OMO or nanomechanical sensing.

Although previous discussions focus on the frequency domain, it can be easily converted to the wavelength domain by use of $d\omega_0/d\lambda_0 = -c2\pi c/\lambda_0^2$. For example, the wavelength-dependent tuning slope can be obtained by $\partial\Omega'_{\rm m}/\partial\Delta_\lambda = -(2\pi c/\lambda_0^2)(\partial\Omega'_{\rm m}/\partial\Delta_\omega)$.

5.2 Experiment realization

5.2.1 System setup

The experiment setup is illustrated in Fig. 5.2. Here a Newport TLB 6700 external cavity tunable laser was used as a light source which has a maximum output power of 30 mW in free space. The wavelength of the laser was tuned around 970 nm by a waveform generator (Agilent 33210A). In our experiment, the laser output was connected to a 99/1 optical directional coupler so that 1% of the light was connected to an optical power meter (Newport 1830c) to monitor the power of the laser output. The 99% output branch was connected to a polarization controller before entering a tapered

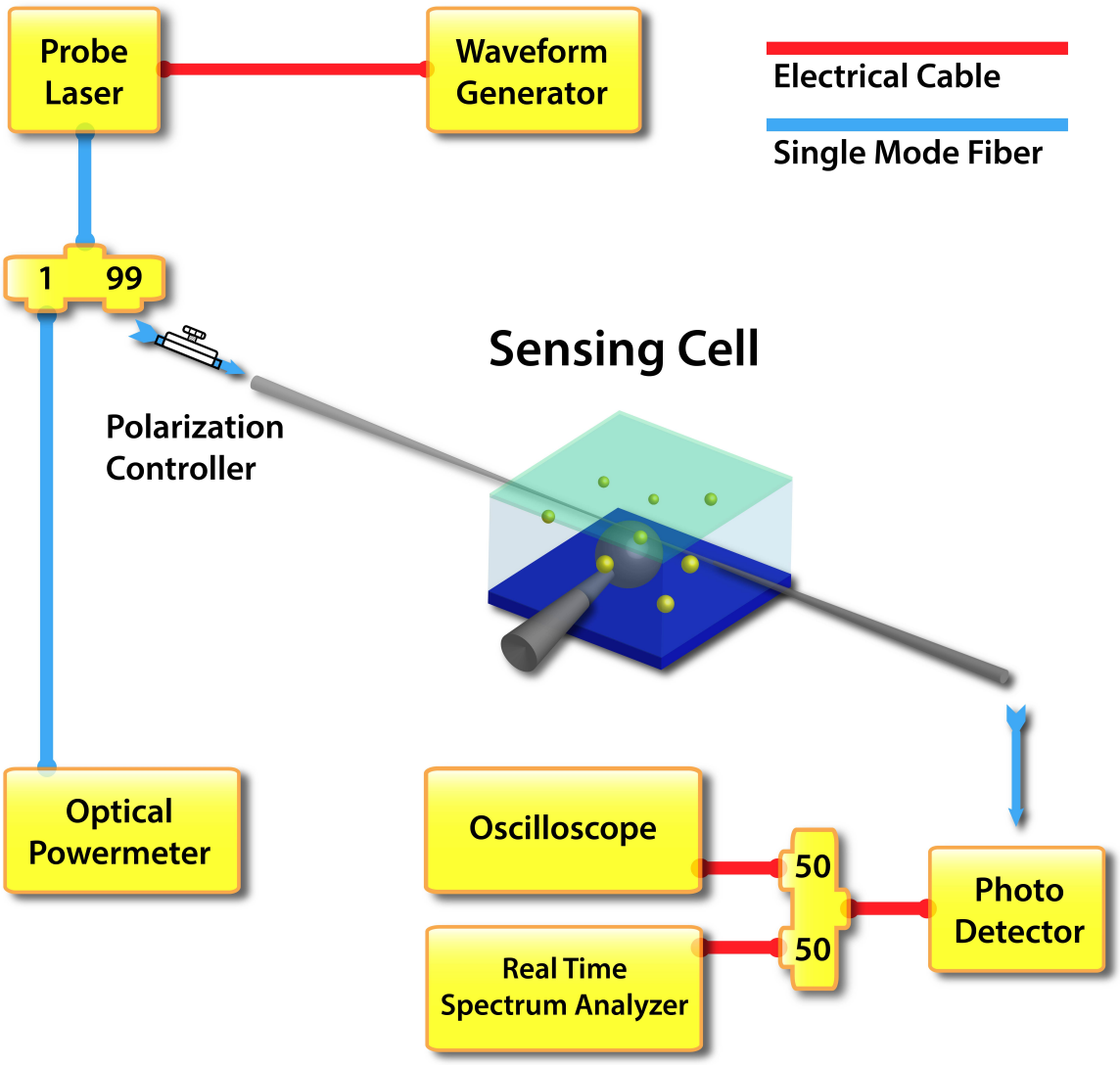

Figure 5.2: Experiment setup for optomechanical transduction sensing.

fiber. The light was then delivered to the silica microsphere through this tapered fiber while the light escaped from the microsphere was coupled to the same taper and delivered to a photodetector before converting into an electrical signal. The electrical signal was divided into two equal output ports using an electrical power splitter where one output signal from the splitter was recorded by an oscilloscope (Agilent DSO 90404A) for time domain measurements and the other output was delivered to a real time spectrum analyzer (Tektronix RSA 3408B) for spectral analysis.

5.2.2 Device characterisation

To verify the above sensing principle, we carried out experiments in a silica microsphere with a diameter of about 100 μm. The optical wave, at a wavelength around 974 nm, was coupled into and out of the device via a tapered optical fiber, as illustrated in Fig. 5.1. The intrinsic optical Q of the device was measured on the silica microsphere immersed in DPBS, with the laser wavelength calibrated by a reference interferometer. The input power was maintained low enough to prevent any optomechanical, thermo-optic, or nonlinear effect. By fitting the cavity transmission spectrum (blue) with a Lorentzian function (red), we obtained an intrinsic optical Q of 4.8×10^6 displayed in Fig. 5.3. Its close agreement with the numerically predicted value of 6×10^6 indicates a nearly-full-elimination of excessive contaminants that could have otherwise degraded the Q.

With such a high optical Q, the optical wave inside the microsphere produces a strong radiation pressure that efficiently actuates the radial breathing mechanical motion of the microsphere (Fig. 5.1). When the optical power is sufficient to suppress the mechanical damping rate, the regenerative oscillation signal occurs within a certain detuning range on the cavity transmission. To excite the coherent OMO, we adjusted the coupling distance between the microsphere and the fiber taper to a position close to critical coupling and increased the input power.

Consequently, by injecting an optical power of 3.0 mW into the cavity, we are able to boost the mechanical mode above the threshold even in the aqueous environment. The transmission spectrum displayed in Fig. 5.4 was obtain with a wavelength scanning laser source operating at a power of 8.5 mW. In addition to the thermally broadened cavity resonance, one can find the oscillation begin near the middle point of the resonance dip, which is corresponding to the high transduction rate regime because of the slop on the Lorentzian function.

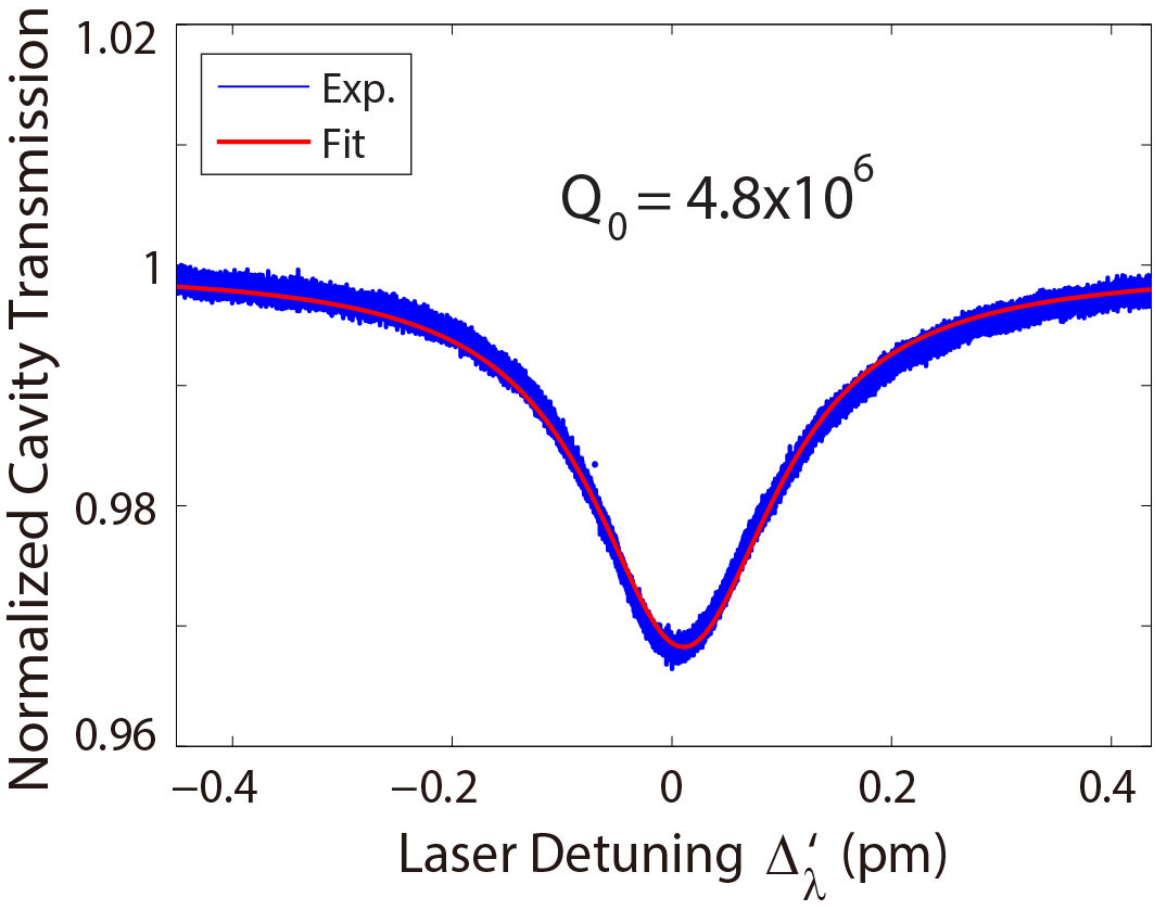

Figure 5.3: The optical transmission spectrum of the microsphere immersed in DPBS, at a probe laser wavelength of 974 nm, with experimental data in blue and theoretical fitting in red. The input power is maintained low enough to characterize the intrinsic optical property of device, which exhibits an intrinsic optical Q of 4.8×10^6.

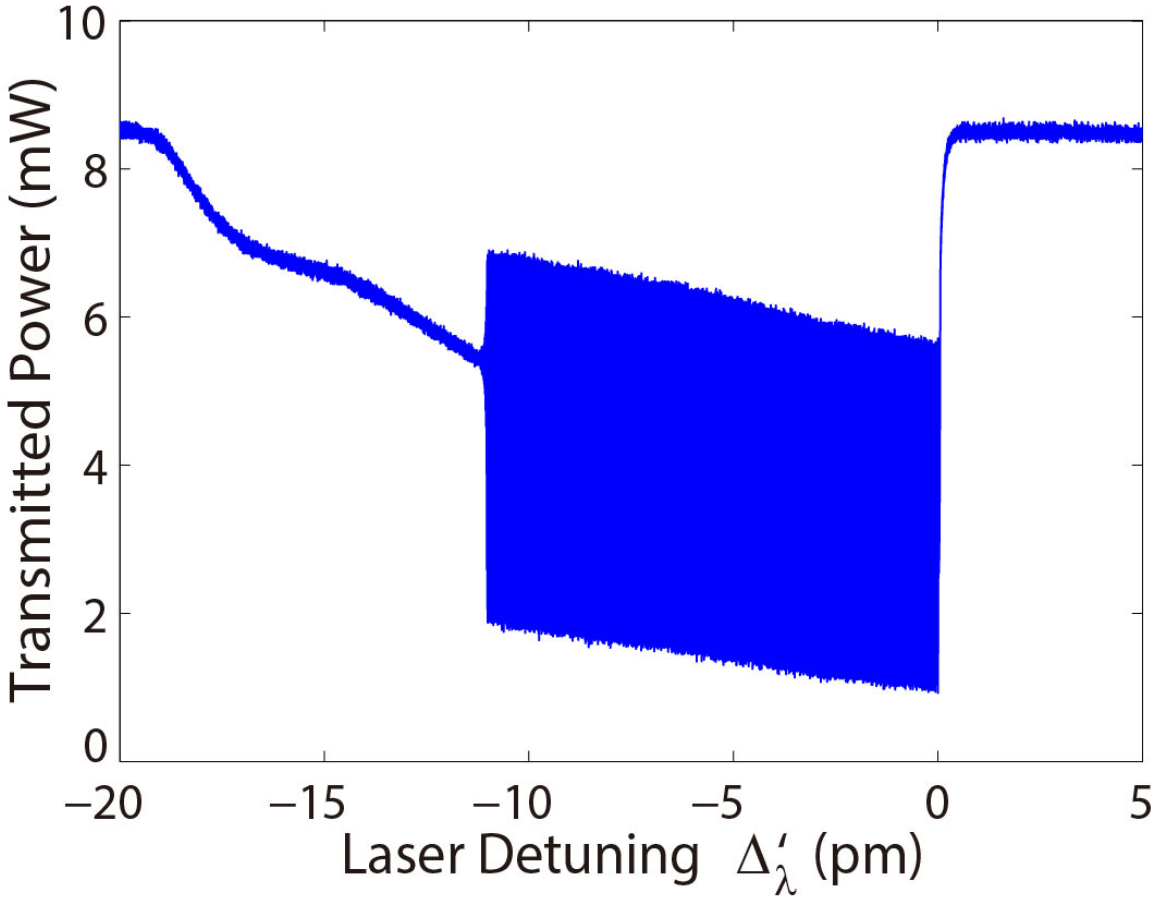

Figure 5.4: The optical transmission spectrum at an input laser power of 8.5 mW. The coherent OMO was excited with a threshold power of 3.0 mW dropped into the cavity.

To characterize the properties of the coherent OMO, we set the wavelength of the continuous-wave laser for stable optomechanical oscillation and recorded the power spectrum of the signal transmitted from the cavity. The linewidth of the OMO was obtained by fitting the fundamental oscillation tone with a Lorentzian function, as shown in Fig. 5.5. The optically pumped resonator is mechanically oscillating at a frequency of 262 kHz with a linewidth as narrow as 0.1 Hz, corresponding to an effective mechanical Q of 2.6×10^6. As shown in Fig. 5.6, the significant optomechanical oscillation leads to a harmonic comb on the power spectrum of the cavity transmission, a feature of coherent OMO resulting from the nonlinear transduction of the optical cavity [20, 114].

5.2.3 Calibration of laser-cavity wavelength detuning

We set the laser wavelength at a off-resonance blue-detuned position and increased it step by step toward the cavity resonance, with a fixed input power. Both the time waveform and power spectrum of the transmitted signal were recorded at each set wavelength. The inset of Figure 5.8 shows the averaged optical power dropped into the cavity $P_{\mathrm{d}}(\Delta'_\lambda)$ as a function of laser wavelength detuning Δ'_λ, which reflects the thermo-optic bistability. The actual laser-cavity detuning, $\Delta_\lambda = \lambda_{\mathrm{l}} - \lambda_0$ where λ_{l} is the laser wavelength, is obtained by the following equation

$$\Delta_\lambda = -\frac{\lambda_0}{2Q_{\mathrm{t}}}\sqrt{\frac{P_{\mathrm{d}}(0) - P_{\mathrm{d}}(\Delta'_\lambda)}{P_{\mathrm{d}}(\Delta'\lambda)}}, \tag{5.11}$$

where $P_{\mathrm{d}}(0)$ is the optical power dropped to the cavity when the probe laser is on-resonance.

5.2.4 OMO frequency versus laser-cavity detuning

In particular, the strong optical spring effect from the optomechanical coupling results in an OMO frequency sensitively dependent on the laser-cavity detuning (Fig. 5.7). As shown in Fig. 5.8, when the laser-cavity wavelength detuning decreases from -150 pm, the OMO frequency increases from 247 kHz to a peak value of 267 kHz, and then decreases quickly to about 115 kHz when the laser wavelength is tuned close to the center of cavity resonance, with a tuning slope of $df_{\mathrm{m}}/d\Delta_\lambda \approx -1.5$ kHz/fm at a laser-cavity detuning of $\Delta_\lambda \approx -70$ fm. The observed optical spring follows closely the

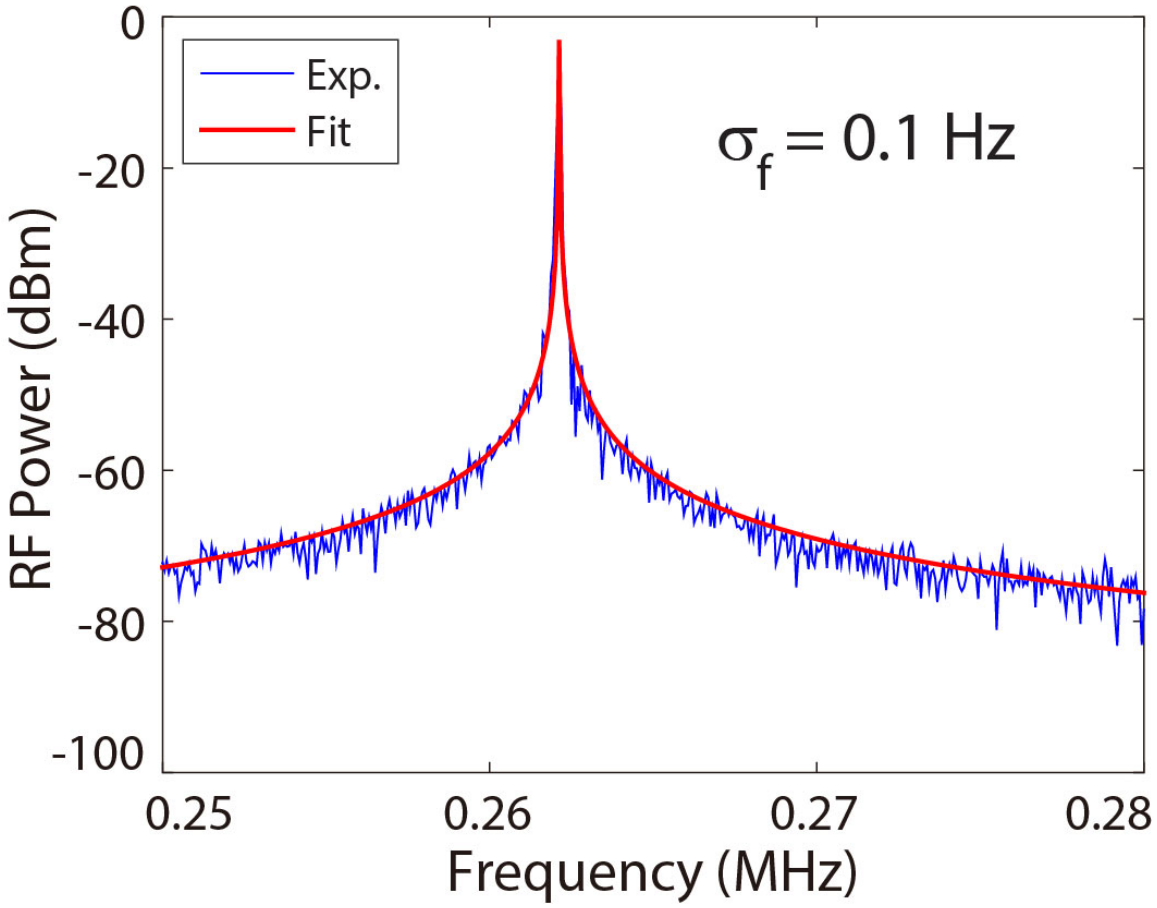

Figure 5.5: The detailed spectrum of the fundamental oscillation tone, with experimental data in blue and theoretical fitting in red. The OMO exhibits a full-width at half maximum of 0.1 Hz, corresponding to an effective mechanical Q of 2.6×10^6.

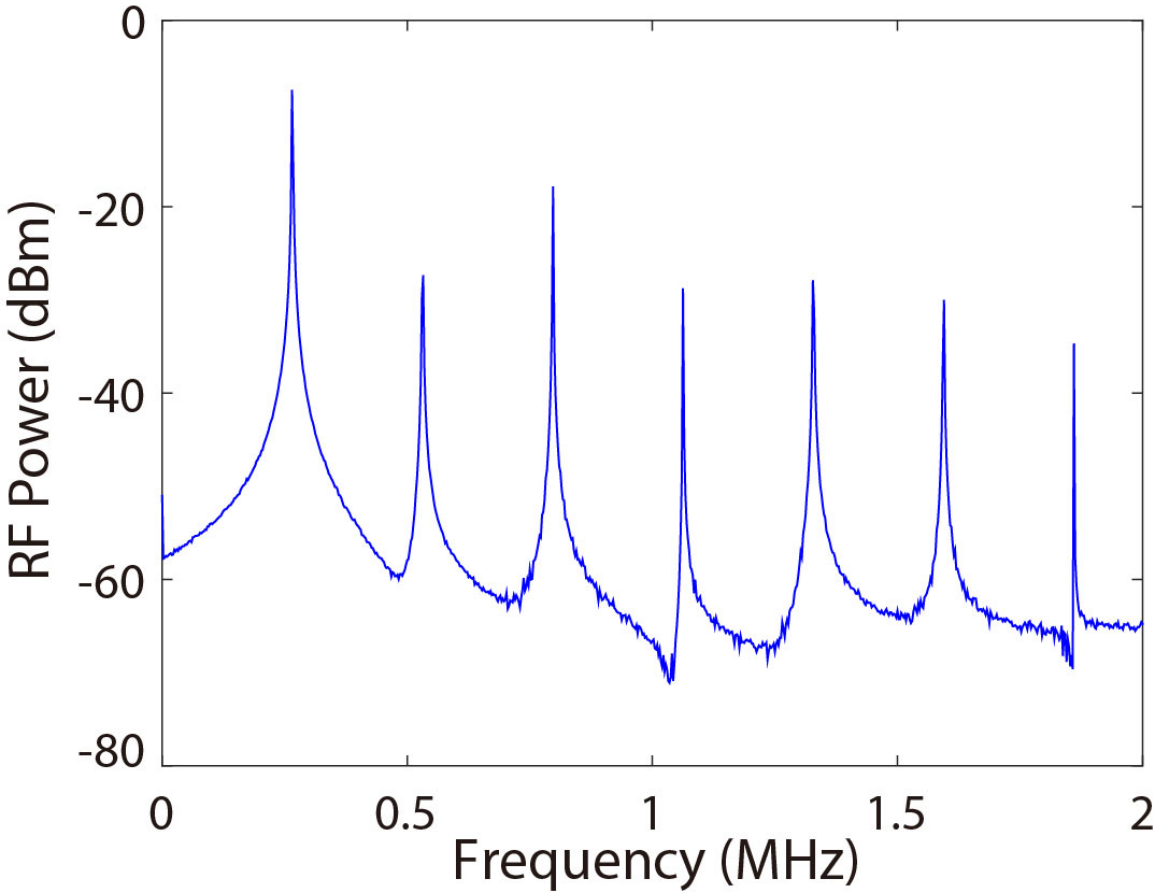

Figure 5.6: An example of the power spectral density of the cavity transmission. The fundamental oscillation frequency is located at 262 kHz, with 6 high-order harmonics clearly visible on the spectrum.

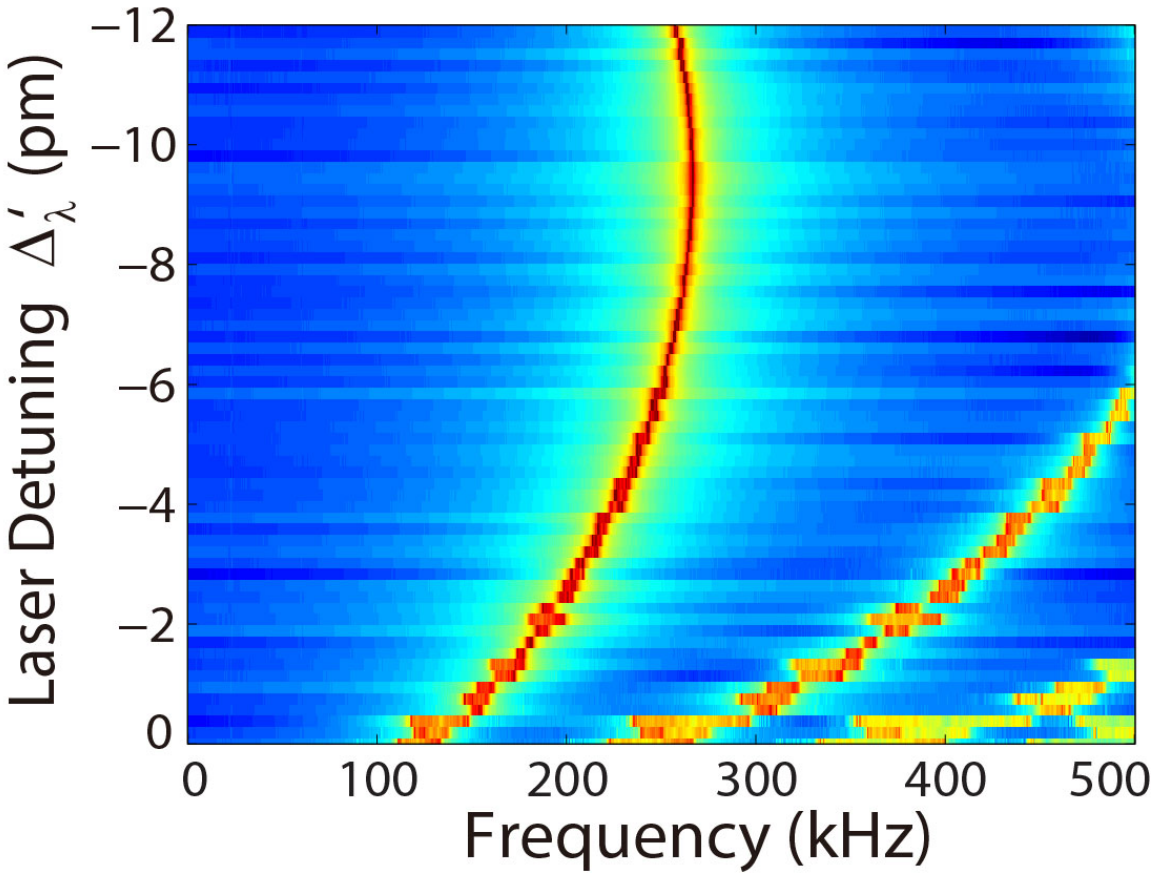

Figure 5.7: Spectrogram of cavity transmitted signal as a function of laser wavelength detuning Δ'_λ (see Fig. 5.8 for the meaning of Δ'_λ), showing the detuning dependent mechanical frequency. The proportional frequency variations at the second and third harmonics are clearly visible. Every spectrum was averaged over 5 traces acquired continuously.

theoretical expectation indicated by the grey curve in Fig. 5.8. The slight discrepancy is likely because the coherent OMO in experiment exhibits a significant amplitude (Fig. 5.4) beyond the linear perturbation regime used in the theoretical estimation.

Equation 5.2 indicates that a maximum mechanical frequency Ω'_{m} occurs at $\Delta_{\omega}^{\max} = \Gamma_{\mathrm{t}}/2\sqrt{3}$ which corresponds to a laser-cavity wavelength detuning of $\Delta_{\lambda}^{\max} = -\lambda_0/(2\sqrt{3}Q_{\mathrm{t}})$. In our experiment, $\Delta_{\lambda}^{\max}$ is measured to be -119 fm , corresponding to a loaded optical Q of $Q_{\mathrm{t}} \approx 2.4{\times}10^6$. In an aqueous environment, the viscosity of the surrounding fluid significantly impacts the mechanical motion of the device, resulting in a dramatically damped mechanical mode with very low mechanical frequency. The mechanical motion is so heavily damped that the intrinsic thermal Brownian motion cannot be clearly detected. As the numerical modeling of the fluidic system is beyond the capability of our current numerical modeling software, we treat the effective mass and the intrinsic mechanical frequency as free parameters in our theoretical analysis. We calculate the mechanical frequency as a function of laser-cavity detuning, which is plotted as a gray solid line in Fig. 5.8. It agrees closely with the experimental observations. The discrepancy is likely because the coherent OMO exhibits a significant amplitude Fig. 5.4 beyond the linear perturbation regime used in the theory. Figure 5.8 shows that the effective rigidity of the mechanical mode is dominated by the optically induced spring in the device and the intrinsic mechanical rigidity plays a fairly minor role.

Such an optical spring corresponds to a sensitive optical-to-mechanical frequency transduction, inferring that every 1-fm cavity resonance wavelength shift induced by a particle binding event can be transduced to an OMO frequency change of about 1.5 kHz that is about four orders of magnitude larger than the linewidth of optomechanical oscillation (Fig. 5.5). A detailed characterization of the Allan deviation of the OMO frequency (Fig. 5.9, see also 5.2.5) shows a minimum two sample deviation of 9.5 Hz at the fundamental OMO frequency, implying a detection resolution of $\delta\lambda/\lambda_0 \approx 6 \times 10^{-12}$ in the device.

This record resolution clearly shows the powerfulness of the demonstrated approach, which is more than 10^4 times higher than a conventional microcavity sensor with the same optical Q [108]. It is even about 50 times higher than that achieved with an optical Q of 10^8 at a visible wavelength [11]. Note that the harmonics of the optomechanical oscillation vary proportionally with the OMO fundamental frequency (Fig. 5.7) and thus can also be applied for particle sensing. Although this does not improve the sensing resolution due to the same signal-to-noise ratio (SNR) of detection,

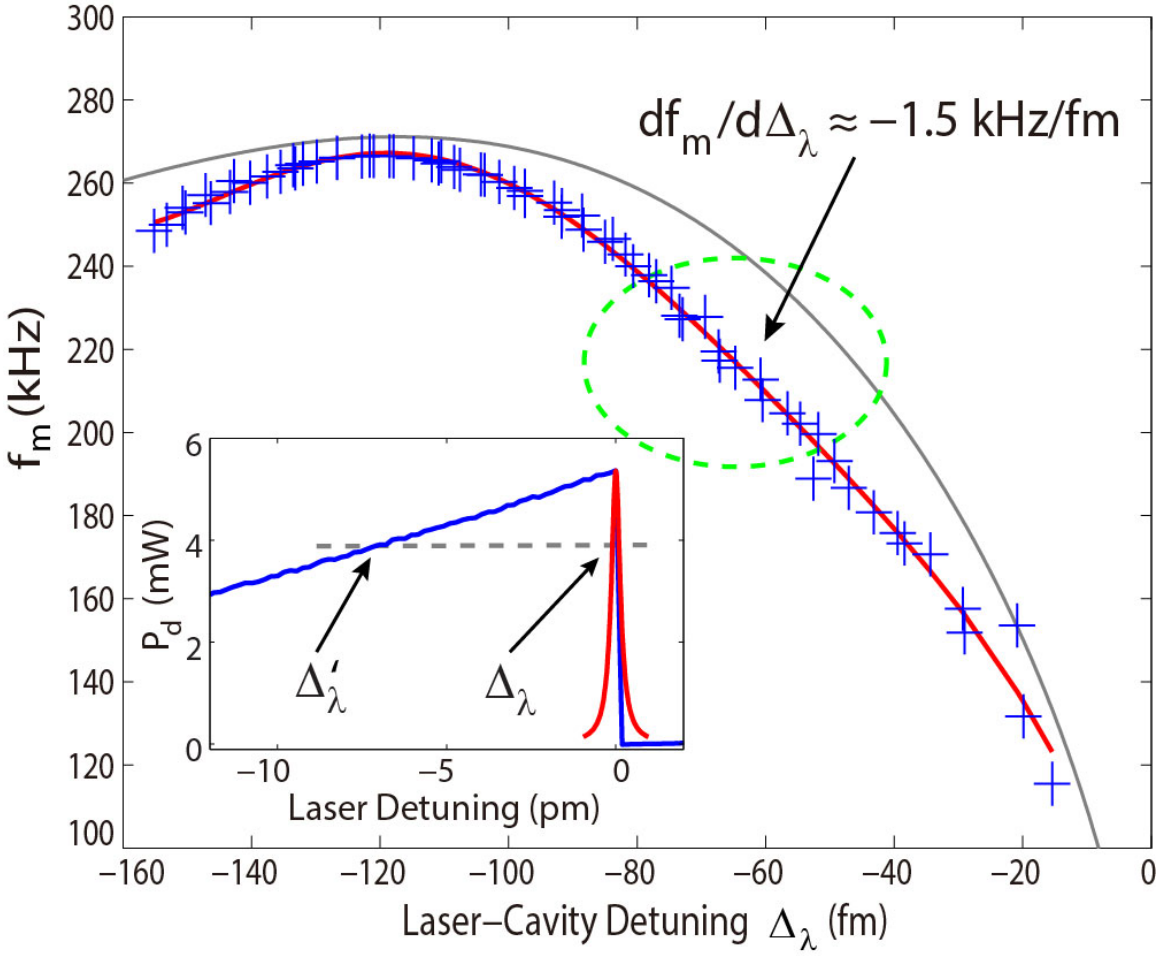

Figure 5.8: The OMO frequency as a function of laser-cavity wavelength detuning. The blue crosses show the experimental data and the grey curve shows the theory. The red curve is a polynomial fitting to the experimental data. The dashed circle indicates the operating regime for the particle and molecule sensing, with a frequency tuning slope of $df_{\mathrm{m}}/d\Delta_\lambda = -1.5$ kHz/fm at a laser-cavity detuning of $\Delta_\lambda = -70$ fm. Inset: Recorded dropped optical power as a function of laser wavelength detuning. This curve was used to obtain the real laser-cavity wavelength detuning $\Delta_\lambda = \lambda_l - \lambda_0$ where λ_l is the laser wavelength.

in practice, the larger frequency shifts on the higher-order harmonics significantly facilitate the mechanical spectrum analysis (by allowing to use a coarser resolution bandwidth), which reduces considerably the excessive detection noises from consecutive multiple particles skimming by the cavity surface (see discussions in 5.2.5).

5.2.5 Allan deviation measurement of OMO frequency

To obtain the background noise and to determine the minimum sensing resolution of our experiment, we measured the Allan deviation of the fundamental, second, and third order harmonics of OMO on the device immersed in pure DPBS in the absence of particle and recorded the power spectra of cavity transmission seamlessly.

Allan deviation [115], named after David W. Allan, is a powerful technique to characterize the frequency stability of an oscillator where many kinds of noises such as flicker noises, random walk noises may lead to a divergent value of the classical standard deviation. For oscillation frequency signals measured continuously in a time interval T, the Allan deviation $\sigma(\tau)$ can be expressed as

$$\sigma(\tau) = \sqrt{\frac{1}{2}\left\langle (f_{\mathrm{m}}(t+\tau) - f_{\mathrm{m}}(t))^2 \right\rangle_t} \tag{5.12}$$

Here $f_{\mathrm{m}}(t)$ is the oscillation frequency measured at time t and $\langle(\cdot)\rangle_t \equiv \frac{1}{T}\int_0^T (\cdot)dt$ denotes the time average of the quantity $(\cdot)$ over T. When a fully incoherent noise such as white noise is the only dominant noise, the Allan deviation is identical to the standard deviation. As f_m is usually measured at discrete time, the above equation needs to be discretized. In our experiment, the OMO frequencies were measured by an realtime electrical spectrum analyzer with a preset sampling rate of δt per spectrum. By representing the measured N OMO frequencies as a time series $f_{\mathrm{m}}(0), f_{\mathrm{m}}(\delta t), f_{\mathrm{m}}(2\delta t), \ldots, f_{\mathrm{m}}((N-1)\delta t)$, the Allan deviation at $\tau = m\delta t, (m = 1, 2, \ldots, N)$ can be derived as

$$\sigma(\tau = m\delta t) = \sqrt{\frac{1}{2(N-m)} \sum_{k=0}^{N-m-1} (f_{\mathrm{m}}((k+m)\delta t) - f_{\mathrm{m}}(k\delta t))^2} \tag{5.13}$$

It is worth mentioning that the Allan deviation typically displays a minimum at τ_{min}. Consequently we can set the acquisition time interval of our spectrum analyzer close to τ_{min} to minimize the measurement noise. Note that in our experiment, τ_{min} is found

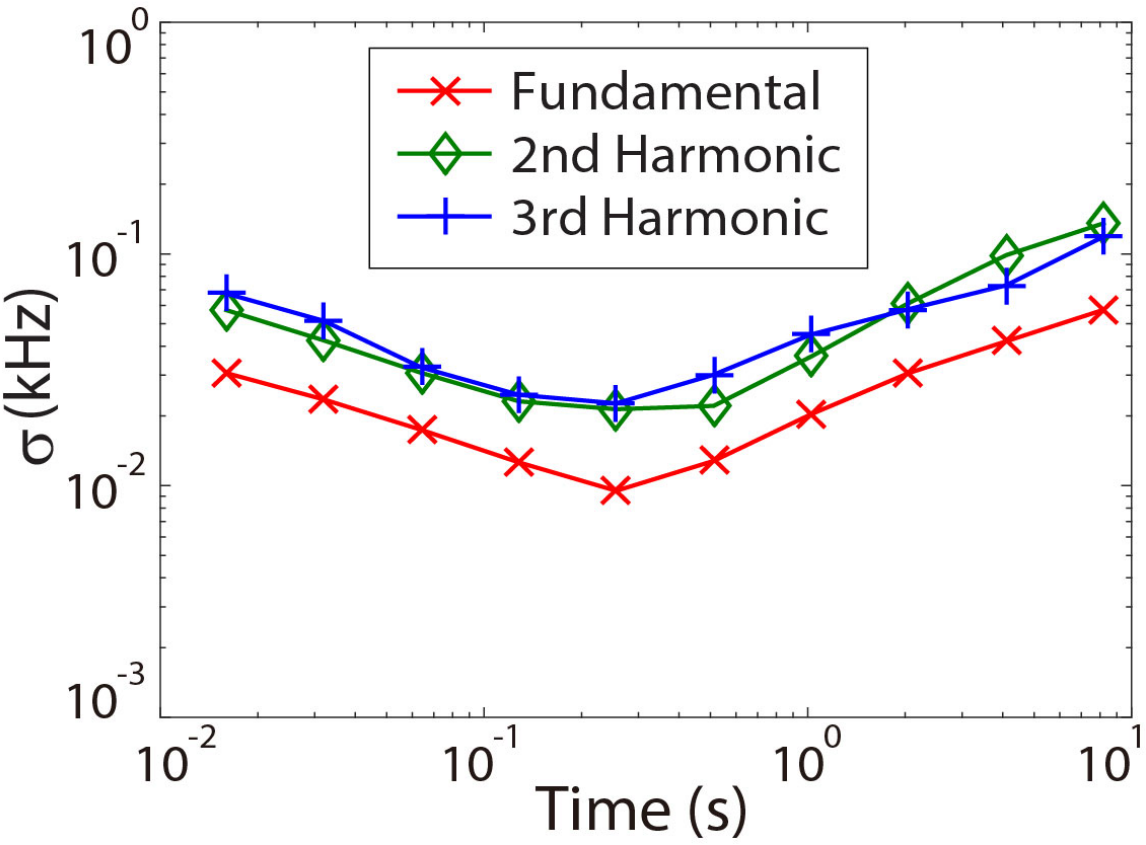

Figure 5.9: The two-sample Allan deviations of the fundamental, second and third harmonic tones measured in bare DPBS in the absence of sensing particle, showing a minimum deviation of 9.5 Hz at the fundamental oscillation tone.

to be around 0.1 second, in close agreement with previously reported results [30, 101].

As shown in Fig. 5.9, the Allan deviation reaches a minimum within a measurement interval of 256 ms with a minimum two sample deviation of 9.5 Hz at the fundamental oscillation. This value of Allan deviation includes all background noises in the experiments, thus corresponding to the minimum detectable shift of fundamental OMO frequency with an SNR of unity. It was also observed that the Allan deviations of higher order harmonics increase almost proportionally to that of the fundamental oscillation tone, indicating that the SNR would not be improved on the higher order harmonics. However, in practice, multiple particles that skim by the cavity surface within a single spectrum acquisition time contribute to an excessive detection noise. This noise can be reduced by sensing at higher order harmonics which facilitates considerably the mechanical spectral analysis (by allowing to use a wider frequency span and coarser resolution bandwidth) so as to ensure a faster data acquisition interval for each spectrum.

5.3 Sensing performance

5.3.1 Silica nanoparticles detection

To characterize the real sensing performance, we performed the sensing experiments on silica nanobeads with different diameters. We set the laser-cavity detuning at the operational point indicated within the dashed circle of Fig. 5.8 and delivered silica nanobeads diluted in Dulbecco's Phosphate-Buffered Saline (DPBS) around the microsphere. A particle binding would introduce a sudden change of the OMO frequency. The particle binding events were recorded by searching the sudden changes of the oscillation frequency in the recorded spectrograms. Typical examples are shown in Fig. 5.10(a)-(d) for the nanobeads with radii of 11.6 nm (NanoComposix, ECP1011), 25 nm (Polyscience, Cat. 24040), 50 nm (Polysciences, Cat. 24041), and 85 nm (Bangs Laboratories, Cat. SS02N), respectively. Here in the case of 11.6-nm beads, the frequency steps were recorded at the third harmonic of the oscillation frequency while all others were obtained at the fundamental. As shown in Fig. 5.10(a), a clear step of 1.3±0.1 kHz (corresponding to 0.43±0.03 kHz step at the fundamental oscillation tone) was observed at the time of 58 second with an SNR of 13. An increase of the oscillation frequency implies a red shift of the cavity resonance wavelength, which corresponds to a binding of a 11.6-nm silica bead on the surface of the microsphere.

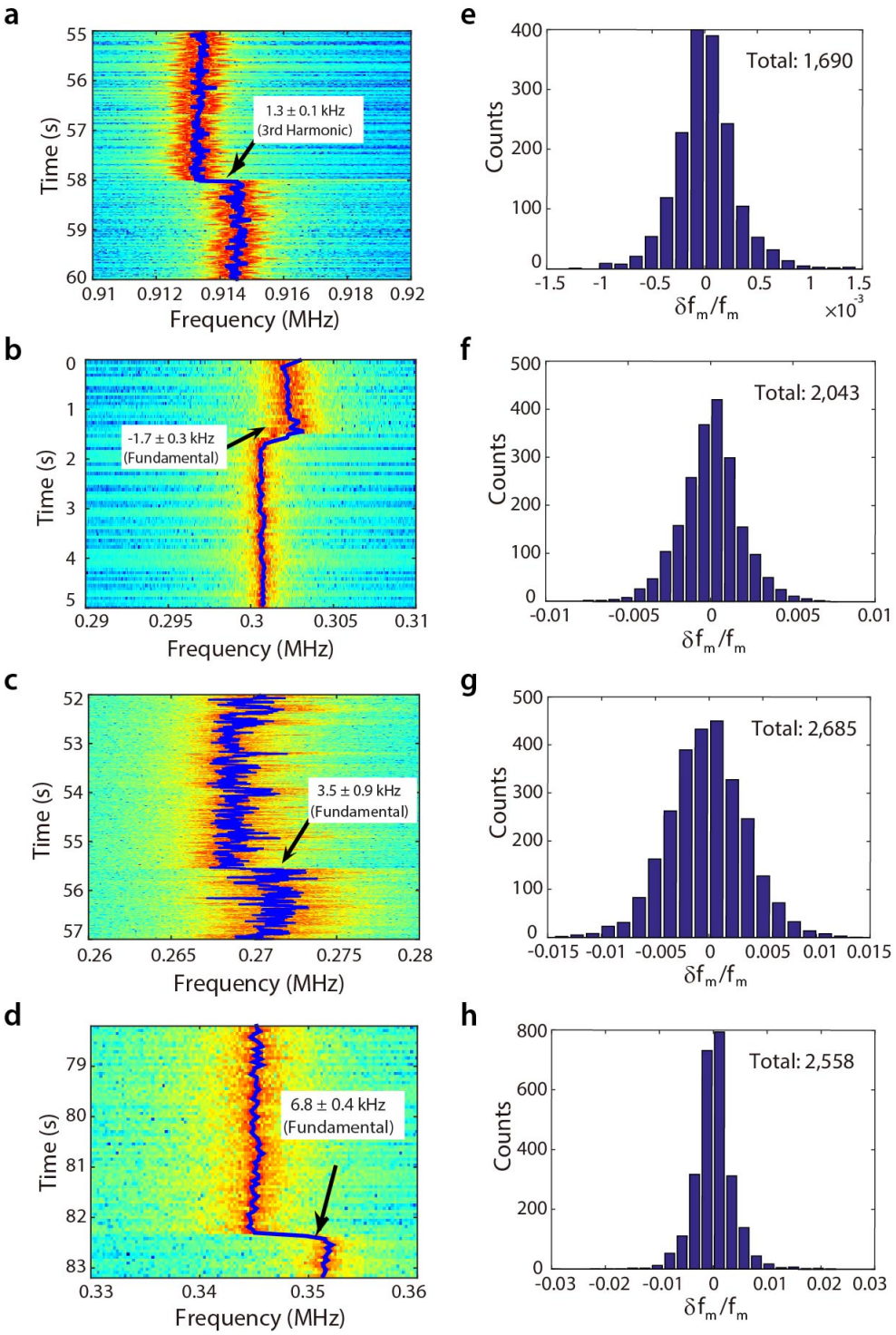

Figure 5.10: (a)-(d) Typical mechanical spectrograms for the binding events of silica beads with average radii of 11.6, 25, 50, and 85 nm, where (a) shows that of third harmonic and (b)-(d) show those of the fundamental oscillation frequency. (e)-(h) The histograms of the normalized frequency steps $\delta f_{\mathrm{m}}/f_{\mathrm{m}}$.

Figures 5.10(b)-(d) show frequency steps of -1.7 ± 0.3, 3.5 ± 0.9, and 6.8 ± 0.4 kHz, respectively, which correspond to the binding (positive frequency steps) or unbinding (negative steps) events of 25-nm, 50-nm, and 85-nm beads.

Note that the direct contribution of particle binding to the mechanical inertia of the OMO is negligible since the masses of the nanobeads ($\sim 0.01 - 5$ fg depending on particle radius) are more than 9 orders of magnitude smaller than the effective motional mass of the OMO (~ 1 μg). The observed OMO frequency shifts induced by particle bindings are purely transduced from the optical spring effect.

To obtain the statistical properties of the binding events, we recorded a total number of $500,121$, $521,389$, $1,335,415$, and $758,728$ spectra in sensing 11.6-nm, 25-nm, 50-nm, and 85-nm beads, respectively, among which frequency steps of $1,690$, $2,043$, $2,685$, and $2,558$ were captured with the SNR exceeding unity. Figures 5.10(e)-(h) show the histograms of the normalized frequency steps, $\delta f_{\rm m}/f_{\rm m}$, which indicate maximum OMO frequency shifts of $\delta f_{\rm m}/f_{\rm m} = (1.4\pm0.4)\times10^{-3}$, $(-7.8\pm1.5)\times10^{-3}$, $(1.3\pm0.3)\times10^{-2}$, and $(-2.3\pm0.6)\times10^{-2}$, respectively, for beads with radii of 11.6, 25, 50, and 85 nm. We converted the recorded OMO frequency steps into the corresponding cavity resonance wavelength shifts $\delta\lambda$, with the transduction rate of $df_{\rm m}/d\Delta_\lambda = -1.5$ kHz/fm. The probability density function of their absolute values are plotted as color bars in Fig. 5.11, with maximum wavelength shifts of $|\delta\lambda|/\lambda_0 = 2.6\times10^{-10}$, 1.2×10^{-9}, 2.4×10^{-9}, and 4.6×10^{-9}, respectively, for the four bead sizes (red circles).

For comparison, we also numerically estimated the expected maximum wavelength change as a function of bead radius (green dashed line). The experiment results agree with the theoretical predictions when the bead size is small (11.6-nm and 25-nm) [74]. At larger bead radii (50-nm and 85-nm), the experiment values are smaller than the theoretical predictions, which is because the optical Q starts to degrade at a large bead size. As an estimation, binding of a 85-nm bead to the equator of a 100-μm microphere would degrade the optical Q by 2.7×10^4. As the optical spring depends on both the laser-cavity detuning and the optical Q, the impact from cavity Q change counteracts that from the cavity resonance wavelength shift, leading to a smaller shift of OMO frequency.

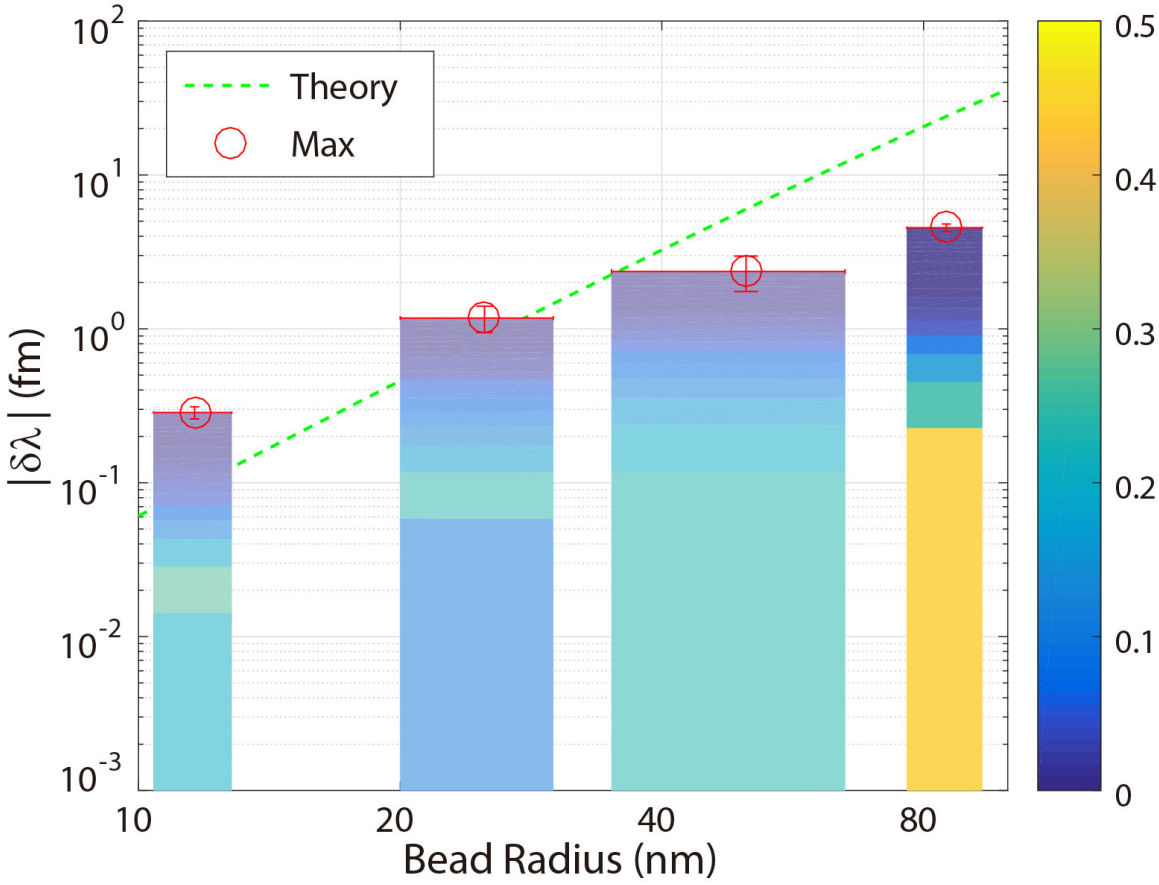

Figure 5.11: The corresponding cavity resonance shifts induced by the particle binding as a function of bead radius. The color bars show the probability density functions of the recorded cavity resonance wavelength shifts induced by particle binding, where the bar width indicates the standard deviation of the bead size (provided by the manufacturer) and the color map indicates the magnitude of probability density. The red circles indicate the recorded maximum wavelength shifts of the cavity resonance. The dashed curve shows the theortical prediction.

5.3.2 Single protein molecules sensing

The ultrahigh detection sensitivity demonstrated on silica nanobeads readily implies the superior capability of sensing single protein molecules. To do so, we injected BSA (Biovision, Cat. 2119-10) diluted in DPBS around the microsphere sensor, with the concentration gradually increased form 0 nM to 10 nM. In the protein sensing experiments, the excessive noises from the unwanted molecules were significantly reduced, resulting in a detection noise level close to the DPBS background noise obtained from the Allan deviation measurement. The third order harmonic of the oscillation frequency was employed to monitor the frequency steps. As shown in Fig. 5.12a, a maximum frequency step of -0.67 ± 0.04 kHz was observed with an SNR of 16.8, which corresponds to a step of -0.22 ± 0.01 kHz at the fundamental oscillation tone. In total, we recorded $145,407$ spectra with nominal concentration up to 10 nM among which $1,785$ frequency steps were captured. The histogram of the normalized frequency steps is plotted in Fig. 5.12b, with the maximum step of $\delta f_{\mathrm{m}}/f_{\mathrm{m}} = (-7.6\pm0.4)\times10^{-4}$ which corresponds to a cavity resonance shift of $|\delta\lambda|/\lambda_0 = 1.5\times10^{-10}$.

As a comparison, we also collected spectra by immersing the microsphere in bare DPBS without any protein molecules. As shown in Fig. 5.12c, the spectrogram indicates the OMO is stable in the absence of BSA molecules. Further, the histogram of all 118 steps found by our program displayed in Fig. 5.12d shows the baseline noise is well below the step signal detected in BSA experiments. This observation clearly proves the capability of sensing single BSA molecules with a molecule weight of 66 kDa. By assuming the resonance shift is proportional to the mass (or equivalently, to the volume) of the protein [116], we derive that our current set-up is capable of detecting proteins as small as 3.9 kDa with an SNR above unity.

The demonstrated single molecule detection now paves the foundation of ultrasensitive cavity optomechanical spring sensing. The sensing resolution can be further improved significantly in the future. For example, the minimal detectable OMO frequency shift in current devices is primarily limited by the laser frequency jitter in our experiment. With an OMO linewidth of only ~ 0.1 Hz, we expect that the future adoption of a fine laser frequency locking circuitry can further improve the sensing resolution by ~ 100 times to around $\delta\lambda/\lambda_0 \sim 10^{-14}$. On the other hand, the optical Q can be increased to above 10^8 if a visible laser is employed [11], which would further improve the sensing resolution by more than one order of magnitude.

Moreover, a plasmonic structure can also be incorporated to enhance the cavity

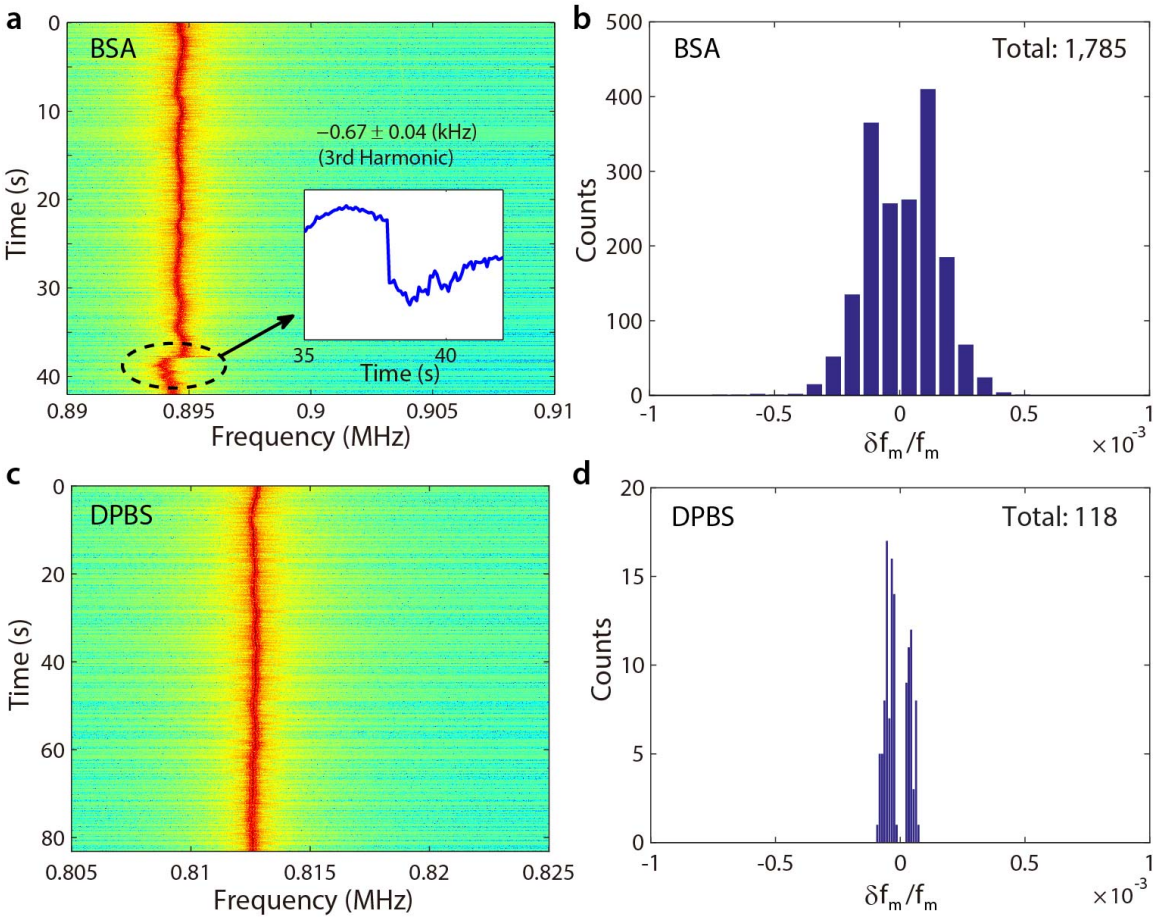

Figure 5.12: (a) A typical mechanical spectrogram recorded at the third harmonic of the oscillation tone, capturing the event of a BSA protein molecule detaching from the silica microsphere surface at 38 second, with a clear frequency step (inset) of -0.67 ± 0.04 kHz. (b) The histogram of the normalized frequency steps. (c) A mechanical spectrogram in the absence of protein molecules. (d) The histogram of the normalized frequency steps.

resonance shift. As the optomechanical effect is intrinsic to a high-Q microcavity, the proposed approach does not rely on any specific external sensing element attached to the device (*e.g.*, a plasmonic nanoantenna [86, 17, 16]), thus capable of fully utilizing the entire effective sensing area offered by a whispering-gallery microcavity which is more than five orders of magnitude larger than that of plasmonic devices. For the same reason, it does not rely on any gain medium, thus universal to different material platforms as long as the device has reasonably high optical Q.

These future improvements would enable detecting small molecules and atoms with a mass down to sub-Dalton level in cryogenic environment, with a great potential for dramatically advancing the capability of sensing to an unprecedented level. In particular, as the molecule binding occurs during the coherent mechanical motion of the sensor, controlling the motion pattern of the coherent OMO (amplitude, phase, time waveform and so on) may function as a unique paradigm to study/control the mechanical properties of molecule binding and unbinding. This, in combination with certain functionalization of the sensor surface [10] and with implementation of potentially versatile optomechanical motions [90], may offer a unique multifunctional biomolecule toolbox that is not only able to observe cellular machineries at work, but also to selectively manipulate single-molecule interactions [117].

Additionally, although we focus here on the particle and molecule sensing, the demonstrated optical spring sensing principle can be applied for other physical sensing applications [118], such as inertial sensing [119, 120], electromagnetic field sensing [121], gas sensing [122] and so on, which are based upon sensitive detection of optical cavity resonance shifts induced by external physical perturbations. Therefore, we expect the demonstrated optical spring to be of great promise for broad applications beyond the particle and molecule sensing itself.

5.4 Summary

In summary, we demonstrated a novel sensing technique by probing the particle induced WGM resonance shift through cavity optomechanical oscillation. The sensing performance evaluated with the detections of silica nanobeads with difference sizes indicated an improvement with orders of magnitude compared to the conventional approaches. It is the optical spring effect that transduces the binding signal to the mechanical frequency step from the optical detuning shift under the cavity reactive sensing principle. With this method, a single BSA protein molecule was detected

with a SNR 16.8. This is a record sensitivity well above all reported plain WGM microcavity sensors without the integration of a plasmonic nanoantenna.

Note that the input optical power dependency of our optomechanical transduction rate suggestted the potential of this technique to outbeat the plasmonic nanantenna sensor given a larger power laser employed. The adoption of frequency locking techniques and higher order harmonics are also directions that can improve the detection sensitivity by orders of magnitude. Finally, the effective sensing area of our technique was estimated to be around 300 μm^2, already 1.5×10^7 larger than a plasmonic nanoantenna reported in [16].

Work in this chapter has appeared in Nature Communications [123]. As indicated in the publication, the author fabricated the devices, prepared the samples and performed the experiments. Wei Jiang and Qiang Lin discovered the sensing principle and mechanism, developed the theory, and conducted the numerical simulation. My supervisor (T.L.) conceived and designed the experiments, developed software to control the experiments and processed the data. Q.L. and T.L. conceived the concept and supervised the project. W.Y., W.C.J., Q.L. and T.L. worked together on the result analysis and interpretation.

Chapter 6

Conclusion and Future Works

In this thesis, we demonstrated a single particle/molecule detector with a high Q whispering gallery mode microcavity. By implementing a Fabry-Pérot interferometer connected in series with the microcavity, we demonstrated a sensitivity to detecting 25-nm-radius ps beads in DPBS without a split-off of the input laser power.

Next, we reported the first observation of the regenerative cavity optomechanical oscillation in an aqueous environment. When the cavity was even immersed in the heavy water, its optical Q was maintained above ten million at a wavelength near 970 nm. As a result, the cavity optomechanical oscillation with a narrow linewidth and a high stability was demonstrated above a pump threshold power around 1.0 mW. By combing the optical spring effect with the reactive sensing principle, we conducted the single silica nanoparticle detections in DPBS by tracing the cavity optomechanical oscillation frequency. We demonstrated the sensitivity improvement of the cavity optical spring sensing by orders of magnitude, compared to the conventional sensings. As a result, we achieved the detection of the single BSA molecule, which had a molecular weight of 66 kDa.

It is worth mentioning that incorporation of existing technologies such as laser frequency locking, plasmonic sensing, and cavity active sensing. The projected sensitivity of the optical spring sensor can reach small molecules and atoms with a mass down to sub-Dalton level in a cryogenic environment, potentially reach the highest sensitivity among all comparable nanosensors. The integration of these technologies will be demonstrated in future researches.

Appendix A

List of Publications

A.1 Journal paper

- **Cavity Optomechanical Spring Sensing of Single Molecules**
  Wenyan Yu, Wei C. Jiang, Qiang Lin, and Tao Lu
  Nature Communications 7, 12311 (2016)

- **Whispering Gallery Microcavity Nanosensor with In-Line Interferometer**
  Steven Herchak, Wenyan Yu, Wu-Sheng Lu, and Tao Lu
  Biosensors Journal 4, 122 (2015)

- **Vectorial Whispering Gallery Mode Solvers Based on Straight Waveguide Modes**
  Wenyan Yu, Steven Herchak, and Tao Lu
  The European Physical Journal Special Topics 223, 1-9 (2014)

- **Coherent Optomechanical Oscillation of a Silica Microsphere in an Aqueous Environment**
  Wenyan Yu, Wei C. Jiang, Qiang Lin, and Tao Lu
  Optics Express Vol. 22, Iss. 18, pp. 21421-21426 (2014)

- **Implementation of a Reference Interferometer for Nanodetection**
  Serge Vincent, Wenyan Yu, and Tao Lu
  Journal of Visualized Experiments (86), e51133 (2014)

- **Cylindrical Beam Propagation Modelling of Perturbed Whispering-gallery Mode Microcavities**
  Mohammad Amin Cheraghi Shirazi, Wenyan Yu, Serge Vincent, and Tao Lu
  Optics Express, Vol. 21, Issue 25, pp. 30243-30254 (2013)

A.2 Conference paper

- **Optical Spring Sensors for Single Molecule Detections**
  Wenyan Yu, Wei Jiang, Qiang Lin, and Tao Lu
  Innovation 360 TEXPO 2016
  Montreal, Qubec, October 17, 2016.

- **An Optomechanical Induced Short Pulse Raman Laser**
  Wenyan Yu, Wei Jiang, Qiang Lin, and Tao Lu
  CLEO2015: Science and Innovations, Optomechanics II
  San Jose, California, United States, May 10-15, 2015.

- **Single Molecule Detection with an Optomechanical Nanosensor**
  Wenyan Yu, Wei Jiang, Qiang Lin, and Tao Lu
  CLEO2015: A&T Topical Review - Optofluidics Microsystems I
  San Jose, California, United States, May 10-15, 2015.

- **Coherent Regenerative Optomechanical Oscillation of a Silica Microsphere in an Aqueous Environment**
  Wenyan Yu, Wei Jiang, Qiang Lin, and Tao Lu
  CLEO2014: Science and Innovations, Optomechanics II (SF2M)
  San Jose, California, United States, June 8-13, 2014.

- **Numerical Analysis of Whispering Gallery Microcavities**
  Tao Lu, Xuan Du, Mohammad Amin Cheraghi Shirazi, Serge Vincent, and Wenyan Yu
  Invited, Pacific Center for Advanced Materials and Microstructures (PCAMM 2013), Dec. 7, 2013.

Bibliography

[1] V. Braginsky, M. Gorodetsky, and V. Ilchenko, "Quality-factor and nonlinear properties of optical whispering-gallery modes," *Physics Letters A*, vol. 137, no. 78, pp. 393 – 397, 1989.

[2] K. Vahala, "Optical microcavities," *Nature*, vol. 424, no. 6950, pp. 839–846, AUG 14 2003.

[3] L. Collot, V. Lefvre-Seguin, M. Brune, J. M. Raimond, and S. Haroche, "Very high-Q whispering-gallery mode resonances observed on fused silica microspheres," *Europhysics Letters (EPL)*, vol. 23, no. 5, p. 327, 1993.

[4] D. Armani, T. Kippenberg, S. Spillane, and K. Vahala, "Ultra-high-Q toroid microcavity on a chip," *Nature*, vol. 421, no. 6926, pp. 925–928, FEB 27 2003.

[5] D. W. Vernooy, A. Furusawa, N. P. Georgiades, V. S. Ilchenko, and H. J. Kimble, "Cavity QED with high-Q whispering gallery modes," *Physical Review A*, vol. 57, pp. R2293–R2296, Apr 1998.

[6] A. Matsko and V. Ilchenko, "Optical resonators with whispering-gallery modes-part I: basics," *IEEE Journal of Selected Topics in Quantum Electronics*, vol. 12, no. 1, pp. 3 – 14, jan.-feb. 2006.

[7] V. Ilchenko and A. Matsko, "Optical resonators with whispering-gallery modes-part II: applications," *IEEE Journal of Selected Topics in Quantum Electronics*, vol. 12, no. 1, pp. 15 – 32, jan.-feb. 2006.

[8] A. Serpengüzel, S. Arnold, and G. Griffel, "Excitation of resonances of microspheres on an optical fiber," *Optics Letters*, vol. 20, no. 7, pp. 654–656, Apr 1995.

[9] F. Vollmer, D. Braun, A. Libchaber, M. Khoshsima, I. Teraoka, and S. Arnold, "Protein detection by optical shift of a resonant microcavity," *Applied Physics Letters*, vol. 80, no. 21, pp. 4057–4059, 2002.

[10] F. Vollmer and S. Arnold, "Whispering-gallery-mode biosensing: label-free detection down to single molecules." *Nature Methods*, vol. 5, no. 5, pp. 591–6, 2008.

[11] T. Lu, H. Lee, T. Chen, S. Herchak, J.-H. Kim, S. E. Fraser, R. C. Flagan, and K. Vahala, "High sensitivity nanoparticle detection using optical microcavities," *Proceedings of the National Academy of Sciences*, vol. 108, pp. 5976–5979, 2011.

[12] F. Vollmer, S. Arnold, and D. Keng, "Single virus detection from the reactive shift of a whispering-gallery mode," *Proceedings of the National Academy of Sciences*, vol. 105, no. 52, pp. 20 701–20 704, 2008.

[13] X. Fan, I. M. White, S. I. Shopova, H. Zhu, J. D. Suter, and Y. Sun, "Sensitive optical biosensors for unlabeled targets: A review," *Analytica Chimica Acta*, vol. 620, no. 1-2, pp. 8 – 26, 2008.

[14] T. Lu, H. Lee, T. Chen, and S. Herchak, "Single molecule detection with an yb-doped microlaser," in *CLEO: Science and Innovations*. Optical Society of America, 2013, pp. CM2H–4.

[15] T. Lu, T. Su, K. Vahala, and S. Fraser, "Split frequency sensing methods and systems," USA Patent US Patent 8,593,638, Nov. 26, 2013, uS Patent 8,593,638.

[16] M. D. Baaske, M. R. Foreman, and F. Vollmer, "Single-molecule nucleic acid interactions monitored on a label-free microcavity biosensor platform," *Nature Nanotechnology*, vol. 9, pp. 933–939, 2014.

[17] V. R. Dantham, S. Holler, C. Barbre, D. Keng, V. Kolchenko, and S. Arnold, "Label-free detection of single protein using a nanoplasmonic-photonic hybrid microcavity," *Nano Letters*, vol. 13, no. 7, pp. 3347–3351, 2013, pMID: 23777440.

[18] T. Carmon, H. Rokhsari, L. Yang, T. J. Kippenberg, and K. J. Vahala, "Temporal behavior of radiation-pressure-induced vibrations of an optical microcavity phonon mode," *Physical Review Letters*, vol. 94, p. 223902, Jun 2005.

[19] T. J. Kippenberg, H. Rokhsari, T. Carmon, A. Scherer, and K. J. Vahala, "Analysis of radiation-pressure induced mechanical oscillation of an optical microcavity," *Physical Review Letters*, vol. 95, p. 033901, Jul 2005.

[20] M. Hossein-Zadeh, H. Rokhsari, A. Hajimiri, and K. J. Vahala, "Characterization of a radiation-pressure-driven micromechanical oscillator," *Physical Review A*, vol. 74, p. 023813, Aug 2006.

[21] T. J. Kippenberg and K. J. Vahala, "Cavity opto-mechanics," *Optics Express*, vol. 15, no. 25, pp. 17 172–17 205, Dec 2007.

[22] H. Rokhsari, T. Kippenberg, T. Carmon, and K. Vahala, "Theoretical and experimental study of radiation pressure-induced mechanical oscillations (parametric instability) in optical microcavities," *IEEE Journal of Selected Topics in Quantum Electronics*, vol. 12, no. 1, pp. 96–107, 2006.

[23] T. P. Burg, M. Godin, S. M. Knudsen, W. Shen, G. Carlson, J. S. Foster, K. Babcock, and S. R. Manalis, "Weighing of biomolecules, single cells and single nanoparticles in fluid," *Nature*, vol. 446, pp. 1066–1069, 2007.

[24] K. L. Ekinci and M. L. Roukes, "Nanoelectromechanical systems," *Review of Scientific Instruments*, vol. 76, no. 6, pp. –, 2005.

[25] P. S. Waggoner and H. G. Craighead, "Micro-and nanomechanical sensors for environmental, chemical, and biological detection," *Lab on a Chip*, vol. 7, no. 10, pp. 1238–1255, 2007.

[26] J. Arlett, E. Myers, and M. Roukes, "Comparative advantages of mechanical biosensors," *Nature Nanotechnology*, vol. 6, p. 203, 2011.

[27] Y.-W. Hu, Y.-F. Xiao, Y.-C. Liu, and Q. Gong, "Optomechanical sensing with on-chip microcavities," *Frontiers of Physics*, vol. 8, no. 5, pp. 475–490, 2013.

[28] F. Liu and M. Hossein-Zadeh, "Mass sensing with optomechanical oscillation," *Sensors Journal, IEEE*, vol. 13, no. 1, pp. 146–147, Jan 2013.

[29] F. Liu, S. Alaie, Z. C. Leseman, and M. Hossein-Zadeh, "Sub-pg mass sensing and measurement with an optomechanical oscillator," *Optics Express*, vol. 21, no. 17, pp. 19 555–19 567, Aug 2013.

[30] S. Olcum, N. Cermak, S. C. Wasserman, K. S. Christine, H. Atsumi, K. R. Payer, W. Shen, J. Lee, A. M. Belcher, S. N. Bhatia *et al.*, "Weighing nanoparticles in solution at the attogram scale," *Proceedings of the National Academy of Sciences*, vol. 111, no. 4, pp. 1310–1315, 2014.

[31] M. Hossein-Zadeh and K. J. Vahala, "Observation of optical spring effect in a microtoroidal optomechanical resonator," *Optics Letters*, vol. 32, no. 12, pp. 1611–1613, Jun 2007.

[32] L. Rayleigh, "The problem of the whispering gallery," *Scientific Papers (Cambridge Univ.)*, vol. 5, pp. 617–620, 1912.

[33] A. Yariv and P. Yeh, *Photonics. Optical Electronics in Modern Communications*, 6th ed. Ox, 2007.

[34] A. Ashkin and J. M. Dziedzic, "Observation of resonances in the radiation pressure on dielectric spheres," *Physical Review Letters*, vol. 38, pp. 1351–1354, Jun 1977.

[35] M. L. Gorodetsky, A. A. Savchenkov, and V. S. Ilchenko, "Ultimate Q of optical microsphere resonators," *Optics Letters*, vol. 21, no. 7, pp. 453–455, Apr 1996.

[36] M. Borselli, T. Johnson, and O. Painter, "Beyond the rayleigh scattering limit in high-q silicon microdisks: theory and experiment," *Optics Express*, vol. 13, no. 5, pp. 1515–1530, Mar 2005.

[37] A. A. Savchenkov, V. S. Ilchenko, A. B. Matsko, and L. Maleki, "Kilohertz optical resonances in dielectric crystal cavities," *Physical Review A*, vol. 70, no. 5, p. 051804, 2004.

[38] I. S. Grudinin and L. Maleki, "Ultralow-threshold raman lasing with caf2 resonators," *Opt. Lett.*, vol. 32, no. 2, pp. 166–168, Jan 2007.

[39] V. S. Ilchenko, A. A. Savchenkov, A. B. Matsko, and L. Maleki, "Nonlinear optics and crystalline whispering gallery mode cavities," *Physical review letters*, vol. 92, no. 4, p. 043903, 2004.

[40] B. Min, T. J. Kippenberg, L. Yang, K. J. Vahala, J. Kalkman, and A. Polman, "Erbium-implanted high-q silica toroidal microcavity laser on a silicon chip," *Physical Review A*, vol. 70, no. 3, p. 033803, 2004.

[41] T. Lu, L. Yang, R. V. A. van Loon, A. Polman, and K. J. Vahala, "On-chip green silica upconversion microlaser," *Optics Letters*, vol. 34, no. 4, pp. 482–484, Feb 2009.

[42] T. Kippenberg, S. Spillane, D. Armani, and K. Vahala, "Fabrication and coupling to planar high-q silica disk microcavities," *Applied Physics Letters*, vol. 83, no. 4, pp. 797–799, 2003.

[43] H. Lee, T. Chen, J. Li, K. Y. Yang, S. Jeon, O. Painter, and K. Vahala, "Chemically etched ultrahigh-Q wedge-resonator on a silicon chip," *Nature Photonics*, vol. 6, pp. 369–373, 2012.

[44] D. J. Griffiths, *Introduction to Electrodynamics*, 3rd ed. Prentice-Hall, 1999.

[45] H. A. Haus, *Electromagnetic Noise and Quantum Optical Measurements*. Springer, 2000.

[46] M. Oxborrow, "Traceable 2-D finite-element simulation of the whispering-gallery modes of axisymmetric electromagnetic resonators," *IEEE Transactions on Microwave Theory and Techniques*, vol. 55, no. 6, pp. 1209 –1218, june 2007.

[47] R. C. Booton, *computational methods for electromagnetics and microwaves*, K. Chang, Ed. JOHN WILEY & SONS, INC., 1992.

[48] D. B. Davidson, *Computational Electromagnetics for RF and Microwave Engineering*. Cambridge University Press, 2005.

[49] S. M. Spillane, T. J. Kippenberg, K. J. Vahala, K. W. Goh, E. Wilcut, and H. J. Kimble, "Ultrahigh-Q toroidal microresonators for cavity quantum electrodynamics," *Physical Review A*, vol. 71, p. 013817, Jan 2005.

[50] S. M. Spillane, T. J. Kippenberg, O. J. Painter, and K. J. Vahala, "Ideality in a fiber-taper-coupled microresonator system for application to cavity quantum electrodynamics," *Physical Review Letters*, vol. 91, p. 043902, Jul. 2003.

[51] G. M. Hale and M. R. Querry, "Optical constants of water in the 200-nm to 200-um wavelength region," *Applied Optics*, vol. 12, no. 3, pp. 555–563, Mar 1973.

[52] D. W. Vernooy, V. S. Ilchenko, H. Mabuchi, E. W. Streed, and H. J. Kimble, "High-Q measurements of fused-silica microspheres in the near infrared," *Optics Letters*, vol. 23, no. 4, pp. 247–249, Feb 1998.

[53] R. Kitamura, L. Pilon, and M. Jonasz, "Optical constants of silica glass from extreme ultraviolet to far infrared at near room temperature," *Applied Optics*, vol. 46, no. 33, pp. 8118–8133, Nov 2007.

[54] M. Born and E. Wolf, *Principles of optics: electromagnetic theory of propagation, interference and diffraction of light.* Cambridge Univ. Press, Cambridge, U.K., 1999.

[55] J. C. Knight, G. Cheung, F. Jacques, and T. A. Birks, "Phase-matched excitation of whispering-gallery-mode resonances by a fiber taper," *Optics Letters*, vol. 22, no. 15, pp. 1129–1131, Aug 1997.

[56] S. P. Vyatchanin, M. L. Gorodetskii, and V. S. Il'chenko, "Tunable narrow-band optical filters with modes of the whispering gallery type," *Journal of Applied Spectroscopy*, vol. 56, pp. 182–187, 1992, 10.1007/BF00662275.

[57] M. Gorodetsky and V. Ilchenko, "High-Q optical whispering-gallery microresonators: precession approach for spherical mode analysis and emission patterns with prism couplers," *Optics Communications*, vol. 113, no. 13, pp. 133 – 143, 1994.

[58] N. Dubreuil, J. C. Knight, D. K. Leventhal, V. Sandoghdar, J. Hare, and V. Lefèvre, "Eroded monomode optical fiber for whispering-gallery mode excitation in fused-silica microspheres," *Optics Letters*, vol. 20, no. 8, pp. 813–815, Apr 1995.

[59] G. Griffel, S. Arnold, D. Taskent, A. Serpengüzel, J. Connolly, and N. Morris, "Morphology-dependent resonances of a microsphere-optical fiber system," *Optics Letters*, vol. 21, no. 10, pp. 695–697, May 1996.

[60] M. Cai, O. Painter, and K. J. Vahala, "Observation of critical coupling in a fiber taper to a silica-microsphere whispering-gallery mode system," *Physical Review Letters*, vol. 85, pp. 74–77, Jul 2000.

[61] M. Cai, O. Painter, K. J. Vahala, and P. C. Sercel, "Fiber-coupled microsphere laser," *Optics Letters*, vol. 25, no. 19, pp. 1430–1432, Oct 2000.

[62] M. L. Gorodetsky and V. S. Ilchenko, "Optical microsphere resonators: optimal coupling to high-q whispering-gallery modes," *Journal of the Optical Society of America B: Optical Physics*, vol. 16, no. 1, pp. 147–154, Jan 1999.

[63] S. M. Spillane, T. J. Kippenberg, and K. J. Vahala, "Ultralow-threshold raman laser using a spherical dielectric microcavity," *Nature*, vol. 415, pp. 621–623, 2002.

[64] T. J. Kippenberg, S. M. Spillane, D. K. Armani, and K. J. Vahala, "Ultralow-threshold microcavity raman laser on a microelectronic chip," *Optics Letters*, vol. 29, no. 11, pp. 1224–1226, Jun 2004.

[65] T. Lu, L. Yang, T. Carmon, and B. Min, "A narrow-linewidth on-chip toroid raman laser," *IEEE Journal of Quantum Electronics*, vol. 47, no. 3, pp. 320–326, March 2011.

[66] T. J. Kippenberg and K. J. Vahala, "Cavity optomechanics: Back-action at the mesoscale," *Science*, vol. 321, no. 5893, pp. 1172–1176, 2008.

[67] I. Favero and K. Karrai, "Optomechanics of deformable optical cavities," *Nature Photonics*, vol. 3, p. 201, 2009.

[68] A. E. Fomin, M. L. Gorodetsky, I. S. Grudinin, and V. S. Ilchenko, "Nonstationary nonlinear effects in optical microspheres," *Journal of the Optical Society of America B: Optical Physics*, vol. 22, no. 2, pp. 459–465, Feb 2005.

[69] Y. Deng, F. Liu, Z. C. Leseman, and M. Hossein-Zadeh, "Thermo-optomechanical oscillator for sensing applications," *Optics Express*, vol. 21, no. 4, pp. 4653–4664, Feb 2013.

[70] J. Li, S. Diddams, and K. J. Vahala, "Pump frequency noise coupling into a microcavity by thermo-optic locking," *Opt. Express*, vol. 22, no. 12, pp. 14 559–14 567, Jun 2014.

[71] V. Ilchenko and M. Gorodetskii, "Thermal nonlinear effects in optical whispering gallery microresonators," *Laser Phys*, vol. 2, no. 6, pp. 1004–1009, 1992.

[72] G. White, "Thermal expansion of reference materials: copper, silica and silicon," *Journal of Physics D: Applied Physics*, vol. 6, no. 17, p. 2070, 1973.

[73] T. Carmon, L. Yang, and K. J. Vahala, "Dynamical thermal behavior and thermal self-stability of microcavities," *Opt. Express*, vol. 12, no. 20, pp. 4742–4750, Oct 2004.

[74] S. Arnold, M. Khoshsima, I. Teraoka, S. Holler, and F. Vollmer, "Shift of whispering-gallery modes in microspheres by protein adsorption," *Optics Letters*, vol. 28, no. 4, pp. 272–274, Feb 2003.

[75] S. Arnold, R. Ramjit, D. Keng, V. Kolchenko, and I. Teraoka, "Microparticle photophysics illuminates viral bio-sensing," *Faraday Discussions*, vol. 137, pp. 65–83, 2008.

[76] S. Arnold, S. I. Shopova, and S. Holler, "Whispering gallery mode bio-sensor ?for label-free detection of single molecules: thermo-optic vs. reactive mechanism," *Optics Express*, vol. 18, no. 1, pp. 281–287, Jan 2010.

[77] Y. Sun and X. Fan, "Optical ring resonators for biochemical and chemical sensing," *Analytical and Bioanalytical Chemistry*, vol. 399, no. 1, pp. 205–211, 2011.

[78] I. Teraoka and S. Arnold, "Theory of resonance shifts in te and tm whispering gallery modes by nonradial perturbations for sensing applications," *JOSA B*, vol. 23, no. 7, pp. 1381–1389, 2006.

[79] M. R. Foreman, D. Keng, E. Treasurer, J. Lopez, and S. Arnold, "Whispering gallery mode single nano-particle detection and sizing: the validity of the dipole approximation," *eprint arXiv:1611.09550*, 2016.

[80] M. Cai and K. Vahala, "Highly efficient optical power transfer to whispering-gallery modes by use of a symmetrical dual-coupling configuration," *Optics Letters*, vol. 25, no. 4, pp. 260–262, Feb 2000.

[81] M. L. Gorodetsky, A. D. Pryamikov, and V. S. Ilchenko, "Rayleigh scattering in high-q microspheres," *J. Opt. Soc. Am. B*, vol. 17, no. 6, pp. 1051–1057, Jun 2000.

[82] J. Zhu, S. K. Ozdemir, Y.-F. Xiao, L. Li, L. He, D.-R. Chen, and L. Yang, "On-chip single nanoparticle detection and sizing by mode splitting in an ultrahigh-q microresonator," *Nature Photonics*, vol. 4, p. 46, 2010.

[83] S. Herchak, W. Yu, W.-S. Lu, and T. Lu, "Whispering gallery microcavity nanosensor with in-line interferometer," *Biosensors Journal*, vol. 2015, 2015.

[84] S. Herchak, "Reference interferometry techniques for nanodetection and biosensing," Ph.D. dissertation, University of Victoria, 2012.

[85] M. A. Santiago-Cordoba, S. V. Boriskina, F. Vollmer, and M. C. Demirel, "Nanoparticle-based protein detection by optical shift of a resonant microcavity," *Applied Physics Letters*, vol. 99, no. 7, p. 073701, 2011.

[86] S. I. Shopova, R. Rajmangal, S. Holler, and S. Arnold, "Plasmonic enhancement of a whispering-gallery-mode biosensor for single nanoparticle detection," *Applied Physics Letters*, vol. 98, no. 24, p. 243104, 2011.

[87] J. Knittel, T. G. McRae, K. H. Lee, and W. P. Bowen, "Interferometric detection of mode splitting for whispering gallery mode biosensors," *Applied Physics Letters*, vol. 97, no. 12, pp. –, 2010.

[88] V. Braginsky, S. Strigin, and S. Vyatchanin, "Parametric oscillatory instability in fabry perot interferometer," *Physics Letters A*, vol. 287, pp. 331 – 338, 2001.

[89] V. B. Braginsky, S. E. Strigin, and S. P. Vyatchanin, "Analysis of parametric oscillatory instability in power recycled LIGO interferometer," *Physics Letters A*, vol. 305, pp. 111 – 124, 2002.

[90] M. Aspelmeyer, T. J. Kippenberg, and F. Marquardt, "Cavity optomechanics," *Rev. Mod. Phys.*, vol. 86, pp. 1391–1452, Dec 2014.

[91] W. Coffey, Y. Kalmykov, and J. Waldron, *The Langevin Equation: With Applications to Stochastic Problems in Physics, Chemistry, and Electrical Engineering*, ser. Series in contemporary chemical physics. World Scientific, 2004.

[92] D. V. Thourhout and J. Roels, "Optomechanical device actuation through the optical gradient force," *Nature Photonics*, vol. 4, p. 211, 2010.

[93] Q. Lin, J. Rosenberg, X. Jiang, K. J. Vahala, and O. Painter, "Mechanical oscillation and cooling actuated by the optical gradient force," *Physical Review Letters*, vol. 103, p. 103601, Aug 2009.

[94] M. Eichenfield, R. Camacho, J. Chan, K. J. Vahala, and O. Painter, "A picogram- and nanometre-scale photoniccrystal optomechanical cavity," *Nature*, vol. 459, p. 550, 2009.

[95] I. S. Grudinin, A. B. Matsko, and L. Maleki, "Brillouin lasing with a caf_2 whispering gallery mode resonator," *Physical Review Letters*, vol. 102, p. 043902, Jan 2009.

[96] S. Tallur, S. Sridaran, and S. A. Bhave, "A monolithic radiation-pressure driven, low phase noise silicon nitride opto-mechanical oscillator," *Optics Express*, vol. 19, no. 24, pp. 24 522–24 529, Nov 2011.

[97] M. A. Taylor, A. Szorkovszky, J. Knittel, K. H. Lee, T. G. McRae, and W. P. Bowen, "Cavity optoelectromechanical regenerative amplification," *Optics Express*, vol. 20, no. 12, pp. 12 742–12 751, Jun 2012.

[98] W. C. Jiang, X. Lu, J. Zhang, and Q. Lin, "High-frequency silicon optomechanical oscillator with an ultralow threshold," *Optics Express*, vol. 20, no. 14, pp. 15 991–15 996, Jul 2012.

[99] X. Sun, K. Y. Fong, C. Xiong, W. H. P. Pernice, and H. X. Tang, "Ghz optomechanical resonators with high mechanical q factor in air," *Optics Express*, vol. 19, no. 22, pp. 22 316–22 321, Oct 2011.

[100] S. Forstner, S. Prams, J. Knittel, E. D. van Ooijen, J. D. Swaim, G. I. Harris, A. Szorkovszky, W. P. Bowen, and H. Rubinsztein-Dunlop, "Cavity optomechanical magnetometer," *Physical Review Letters*, vol. 108, p. 120801, Mar 2012.

[101] K. Hyun Kim, G. Bahl, W. Lee, J. Liu, M. Tomes, X. Fan, and T. Carmon, "Cavity optomechanics on a microfluidic resonator with water and viscous liquids," *Light: Science & Applications*, vol. 2, 2013.

[102] W. Yu, W. C. Jiang, Q. Lin, and T. Lu, "Coherent optomechanical oscillation of a silica microsphere in an aqueous environment," *Opt. Express*, vol. 22, no. 18, pp. 21 421–21 426, Sep 2014.

[103] M. Hanay, S. Kelber, A. Naik, D. Chi, S. Hentz, E. Bullard, E. Colinet, L. Duraffourg, and M. Roukes, "Single-protein nanomechanical mass spectrometry in real time," *Nature nanotechnology*, vol. 7, no. 9, pp. 602–608, 2012.

[104] M. Piliarik and V. Sandoghdar, "Direct optical sensing of single unlabelled proteins and super-resolution imaging of their binding sites," *Nature Communications*, vol. 5, p. 4495, 2014.

[105] R. W. Boyd and J. E. Heebner, "Sensitive disk resonator photonic biosensor," *Applied Optics*, vol. 40, no. 31, pp. 5742–5747, Nov 2001.

[106] J. Knittel, J. D. Swaim, D. L. McAuslan, G. A. Brawley, and W. P. Bowen, "Back-scatter based whispering gallery mode sensing," *SCIENTIFIC REPORTS*, vol. 3, no. 2974, 2013.

[107] S. Avino, A. Krause, R. Zullo, A. Giorgini, P. Malara, P. D. Natale, H. P. Loock, and G. Gagliardi, "Direct sensing in liquids using whispering-gallery-mode droplet resonators," *Advanced Optical Materials*, vol. 2, p. 1155, 2014.

[108] I. M. White and X. Fan, "On the performance quantification of resonant refractive index sensors," *Optics Express*, vol. 16, no. 2, pp. 1020–1028, Jan 2008.

[109] B. Min, E. Ostby, V. Sorger, E. Ulin-Avila, L. Yang, X. Zhang, and K. Vahala, "High-q surface plasmon polariton whispering gallery microcavity," *Nature*, vol. 457, p. 455, 2009.

[110] F. Marquardt and S. M. Girvin, "Optomechanics," *Physics*, vol. 2, p. 40, 2009.

[111] M. Aspelmeyer, T. J. Kippenberg, and F. Marquardt, Eds., *Cavity Optomechanics Nano- and Micromechanical Resonators Interacting with Light*. Springer-Verlag Berlin Heidelberg, 2014.

[112] D. Van Thourhout and J. Roels, "Optomechanical device actuation through the optical gradient force," *Nature Photonics*, vol. 4, no. 4, pp. 211–217, 2010.

[113] K. H. Kim and X. Fan, "Surface sensitive microfluidic optomechanical ring resonator sensors," *Applied Physics Letters*, vol. 105, no. 19, pp. –, 2014.

[114] C. Xiong, X. Sun, K. Y. Fong, and H. X. Tang, "Integrated high frequency aluminum nitride optomechanical resonators," *Applied Physics Letters*, vol. 100, p. 17, 2012.

[115] D. W. Allan, N. Ashby, and C. C. Hodge, *The science of timekeeping*. Hewlett-Packard, 1997.

[116] I. Teraoka, S. Arnold, and F. Vollmer, "Perturbation approach to resonance shifts of whispering-gallery modes in a dielectric microsphere as a probe of a surrounding medium," *Journal of the Optical Society of America B: Optical Physics*, vol. 20, no. 9, pp. 1937–1946, Sep 2003.

[117] D. J. Mller and Y. F. Dufrne, "Atomic force microscopy as a multifunctional molecular toobox in nanobiotechnology," *Nature Nanotechnology*, vol. 3, p. 261, 2008.

[118] M. R. Foreman, J. D. Swaim, and F. Vollmer, "Whispering gallery mode sensors," *Advances in optics and photonics*, vol. 7, no. 2, pp. 168–240, 2015.

[119] C. Ciminelli, F. DellOlio, C. E. Campanella, and M. N. Armenise, "Photonic technologies for angular velocity sensing," *Advances in Optics and Photonics*, vol. 2, no. 3, pp. 370–404, 2010.

[120] A. G. Krause, M. Winger, T. D. Blasius, Q. Lin, and O. Painter, "A high-resolution microchip optomechanical accelerometer," *Nature Photonics*, vol. 6, no. 11, pp. 768–772, 2012.

[121] T. Ioppolo, U. Ayaz, and M. V. Ötügen, "Tuning of whispering gallery modes of spherical resonators using an external electric field," *Optics express*, vol. 17, no. 19, pp. 16 465–16 479, 2009.

[122] N. A. Yebo, S. P. Sree, E. Levrau, C. Detavernier, Z. Hens, J. A. Martens, and R. Baets, "Selective and reversible ammonia gas detection with nanoporous film functionalized silicon photonic micro-ring resonator," *Optics express*, vol. 20, no. 11, pp. 11 855–11 862, 2012.

[123] W. Yu, W. Jiang, Q. Lin, and T. Lu, "Cavity optomechanical spring sensing of single molecules," *Nature Communications*, vol. 7, p. 12311, 2016.